Universiteit Utrecht

In-Situ Characterization of $BiVO_4$ Photoanodes for Solar-Driven Fuel Production

Silvia Zanoni

Master Thesis

2015-2016

In-situ Characterization of $BiVO_4$ Photoanodes for Solar-driven Fuel Production

Silvia Zanoni (UU-4202678)

Under the supervision of

Dr. Monica Barroso,

Ivan Garcia Torregrosa,

Prof. dr. ir. Bert Weckhuysen

Inorganic Chemistry and Catalysis group

Utrecht University

Abstract

The conversion of solar energy into chemicals that could be used as fuels is envisioned as a solution to the energy demand continuous growth. In particular, with the process of photoelectrochemical (PEC) water splitting, sunlight can be used to produce hydrogen from water. Hydrogen can be converted to power or heat with no green gasses emissions and only water as a by-product, making it an ideal fuel. The photoelectrochemical process makes the conversion of solar energy into chemical bonds possible, thanks to the employment of semiconductor materials. Such materials are used as thin film anodes or cathodes in an electrochemical cell. By absorbing photons, they are able to generate excited charges, which are then used in the electrochemical circuit of the cell to allow the redox reaction of water splitting into hydrogen and oxygen.

During this research project $BiVO_4$ was investigated, a semiconductor that can be used as a photoanode in a PEC system. Such material has ideal properties, but its actual performances are far below its potential. The reasons behind its low efficiencies are slow electron mobility, fast electron-hole recombination and very poor surface kinetics for water oxidation. To give a better insight into its properties and how to improve its performances, $BIVO_4$ thin films were synthetized and different expedients were used to try to improve its performances. Furthermore, by means of a transient absorption spectrometer, the charge carrier dynamics on the ns-μs window were analysed.

The synthesis of $BiVO_4$ by means of a spin coater was successful in the production of homogeneous and photoactive semiconductor films. On the other hand, the synthesis by spray pyrolysis was found to be more troublesome. The film width influence on photoactivity was studied and it was found that approximately 100 nm corresponded to an optimal thickness. The very low surface kinetics for water oxidation was well addressed by the addition of a CoPi co-catalyst for water oxidation by photo-assisted electrodeposition on the sample surface. The bulk properties were modified by the addition of W in the crystal lattice of $BiVO_4$ as a dopant. The optimal concentration was found to be of 0.2% W to be added to the precursor's solution during the synthesis procedure.

Residual carbon was detected on all samples. This was believed to negatively affect the photoanodes performances. Carbon concentration was drastically reduced by annealing the samples at 600°C with a drastic positive effect on their photoperformance.

Charge carrier dynamics of the synthetized $BIVO_4$ photoanodes were then explored by means of a transient absorption spectrometer. The window investigated was in the ns-μs range and it was established that bulk recombination phenomena would occur in such time scale. Namely, direct bimolecular recombination of electron and holes, mathematically described by a single exponential decay occurred in the fast phase (ns), while trap-mediated recombination processes took place on a longer scale (μs), defined by a power-law decay. On the other hand, the process of holes injection into the surface was believed to befall outside the time window investigated. Besides, experiments conducted with the sample immersed in a phosphate buffer caused the degradation of the sample. Such degradation was more evident when a positive voltage was applied.

Contents

1.Introduction.....1

1.1. Hydrogen as solar fuel.....1

1.2. Photoelectrochemical water splitting.....3

1.2.1. Chemistry and thermodynamics of water splitting and PEC cell description.....3

1.2.2. Semiconductor-electrolyte interface.....5

1.2.3. PEC efficiencies.....6

1.2.4. Ideal photoanode characteristics for water splitting.....8

1.3. Material investigated: $BiVO_4$ as photoanode.....9

1.3.1Crystal structure and electronic properties.....11

2. Research Project Aims.....14

2.1. Strategies to enhance $BiVO_4$ photoperformance.....14

2.1.1. Thickness.....14

2.1.2. Deposition of a co-catalyst for oxygen evolution.....16

2.1.3. Doping.....17

2.2. Charge carrier dynamics investigation.....19

3. Methods.....21

3.2. Deposition methods.....21

3.2.1. Spray pyrolysis.....21

3.2.2. Spin coating 23

3.3. Characterization methods 25

3.3.1. TGA, UV-Visible spectroscopy, XRD, SEM.....25

3.3.2. Photoelectrochemical measurements.....26

3.3.3. Transient absorption spectroscopy (TAS) 28
4. Results....31
4.1. TGA on precursors....31
4.2. Synthesis procedures....32
4.2.1.Spray pyrolysis....32
4.2.2. Spin coating....34
4.3. Structural characterization and photocatalytic analysis....36
4.3.1. Thickness investigation....36
4.3.2. "CoPi" photo-assisted electrodeposition....43
4.3.3. doping with W....44
4.3.4. Extra annealing treatment at 600°C....47
4.3.5. Structural and photocatalytic results summary....54
4.4. Charge dynamics investigation....58
4.4.1. TAS results....58
4.4.2 Semi-quantitative analysis and result summary....64
5. Conclusions....70
6. Outlook 71
7. Bibliography....72
8. Appendix....77
8.1. Tauc plots....77
8.2. FTO surface....79
8.3. Annealing temperature investigation....80
8.4. TAS: alpha and constant rate values....82

1. Introduction

1.1. Hydrogen as solar fuel

The world demand for energy is rising unceasingly. In 2011 the global consumption was equivalent to a thermal output of 16.35 TW and it is estimated to double, at the least, by 2050.[1,2] Nowadays 87% of the total energy consumed is supplied by fossil fuels and only 10% by renewables. Based on the current consumption rate, the estimated availabilities of these fuels range from 150 to 400 years for coal, 40–80 years for oil, and 60–160 years for natural gas.[3,4] This is a clear evidence that basing our energy system on such resources will not be sustainable over time. It is therefore of substantial importance to shift our energy consumption toward renewables as wind, hydro, biomass, solar and geothermal power.

One of the biggest renewable resources that is available to us is solar energy. Sunlight strikes the earth with 120'000 TW/year which is more than 7'000 times than what we consume.[1,3] With an irradiance of 1'353 W/m^2, the solar spectrum at the top of the earth's atmosphere, denoted as air mass 0 (AM 0),[5] is closed to that of a 5'800 K blackbody. At sea level, the sunlight has travelled through the atmosphere and filtered by it, resulting in a spectrum no longer similar to the one of a black body. At equatorial regions, with a solar zenith angle of 0°, the spectrum is referred to as AM 1. However, the AM 1.5 spectrum, which corresponds to a solar zenith angle of 48,19°, approximates better the average sunlight experienced by most regions of the world, which are at mid-latitudes where the light is in fact received at a tilted angle.[5,6]

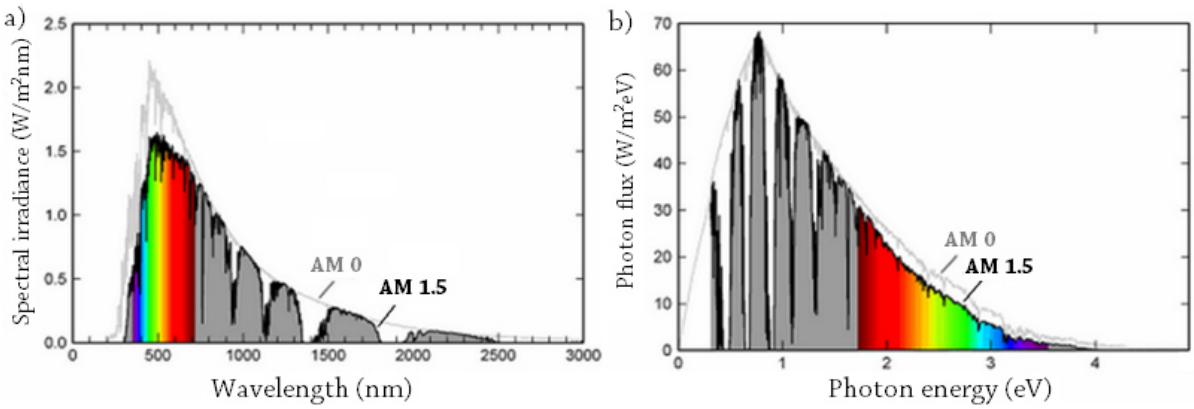

Figure 1: a) Spectral solar irradiance on Earth before passing through the atmosphere, AM 0 (grey line), and at sea level with a solar zenith angle of 48.19°, AM 1.5 (black line). b) Photon flux of the AM0 and AM1.5 spectra. The coloured sections indicate the visible region of the spectra.

The AM 0 and AM1.5 spectra and photon fluxes are depicted in Figure 1. The total output irradiance of the AM1.5 spectrum is reduced to 964 W/m^2, which is the reason why the AM 1.5 simulated sunlight at 1'000 W/m^2, also referred as 1 sun, is used for standardized solar cell testing.

Figure 2: Area of land that needs to be covered with 10% efficient solar cells in order to generate 20 TW of electrical power.[4]

To harness 20 TW of power from the sun, the area to be covered with 10% efficient solar cells would be about 816'000 km^2. When projected onto Africa, as shown in Figure 2, this region seems relatively small, but it should be realized that covering that area with solar cells presents a discouraging task. Indeed, in order to achieve such goal, one would need to produce on average 650 m^2 of solar cell panels per second, every single day of the next 40 years.[4]

Furthermore, the sun is not constantly illuminating the whole globe (day and night cycle) and, even when it does, due to weather conditions, it is not always with a sufficient intensity. Hence, converting solar light to electricity to be directly employed cannot be the only way to exploit the large amount of energy that the sun is irradiating us with. It is therefore essential to develop a way to store this energy. Collecting and storing solar energy in chemical bonds is one of the ways that could make this aim achievable. The energy of a visible-light photon ranges between 1 and 3 eV, which is more than sufficient for many chemical synthesis routes. Ideally, what's needed is an energy vector that can be efficiently generated from renewable sources and that can be easily stored, but also straightforwardly transported to the point of use. Furthermore, due to the environmental consequences of climate change, the ideal fuel should not only come from a renewable source, but also have low CO_2 and other greenhouse gasses emission, when converted into energy by combustion.

Hydrogen is one of the world most abundant elements and it is an extremely valuable chemical today. Its low density, high thermal conductivity and strong chemical reducing properties make it ideal for several industrial applications. The production of hydrogen from water using solar light, with the so-called photoelectrochemical water splitting reaction, is envisioned as a primary route for the storage and distribution of energy derived from the sun. Moreover, using fuel-cells or combustion engine technologies, hydrogen can be converted to power or heat with only water as a by-product, making it the ideal fuel.[7] However, to satisfy the large industrial demand, hydrogen is nowadays mainly produced by fossil fuel conversion, primarily by the steam methane reforming process:

$$CH_4 + 2H_2O \rightarrow 4H_2 + CO_2 \tag{1.1}$$

As shown in the equation above, this process produces also CO_2, which makes water splitting an obvious better choice in terms of environmental friendly process. However, the production cost of hydrogen by steam methane reforming is around 2-3 \$/Kg, which is much cheaper than any currently available system for solar hydrogen production (10 \$/Kg).[7–10]

Therefore, developing a system with high performances, low complexity and able to produce hydrogen at a competitive price is still a major challenge. Photoelectrochemical water splitting is a promising process which will help us achieve a better and more sustainable energy economy, but it still needs to be significantly improved in terms of efficiency and costs.

1.2. Photoelectrochemical water splitting

1.2.1. Chemistry and thermodynamics of water splitting and PEC cell description

In the photoelectrochemical (PEC) water splitting process, solar energy is converted into electrochemical energy, thanks to a photoactive semiconductor material. There are different types of PEC cells. For simplicity, only the kind of cell used during this research project will here be considered.

In the employed photoelectrochemical cell, as shown in Figure 3, the photosensitive semiconductor working electrode (WE) is the anode, wire-connected to a metallic counter electrode (CE). Both are immersed in the electrolyte. In this thesis the focus is indeed on $BiVO_4$, a n-type semiconductor, therefore used as a photoanode, while the counter electrode is a metallic Pt cathode. A third electrode, (Ag/AgCl), even though not depicted in figure, is also employed during all experiments conducted during this research, as a reference electrode (RE).

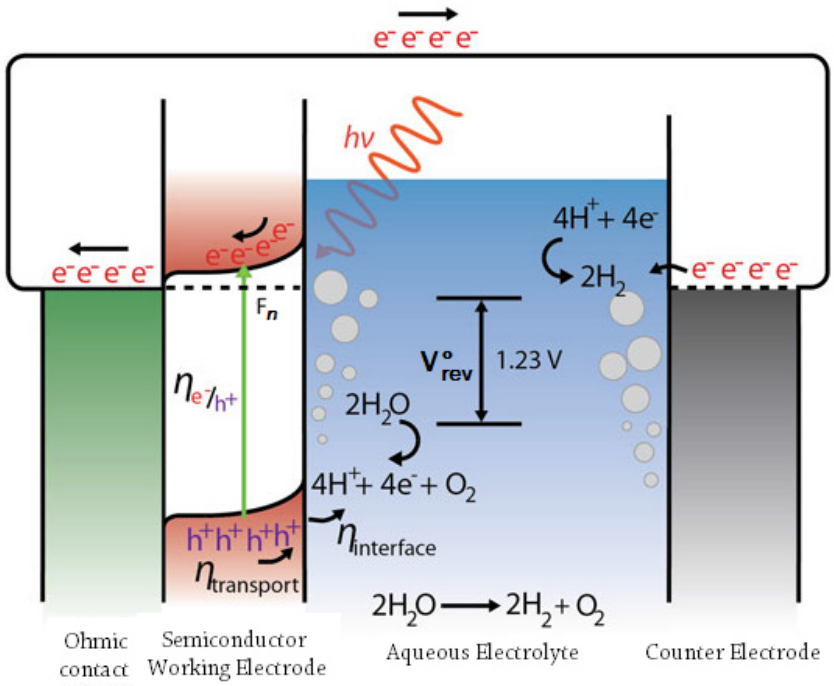

Figure 3: Scheme of the basic principles and functioning of water splitting for a specific kind of photoelectrochemical cell. Sunlight hits an n-type semiconductor photoanode, the working electrode, where the charge carriers are generated. Holes are injected in the electrolyte and oxygen is evolved, while electrons are transported by a conductive wire to the counter electrode, where hydrogen evolution occurs. F_n is the Fermi level of the semiconductor. V^0_{rev} is the standard reversible potential for water splitting. η_{e^-/h^+} indicated the separation efficiency of the generated charges, $\eta_{transport}$ is the efficiency with which electrons reach the back contact and holes the surface of the electrode and $\eta_{interface}$ is the efficiency of holes injection into the electrolyte. [11]

In section 1.2.2 a closer look will be taken to what happens at the semiconductor when put into contact with the electrolyte under illumination, while here the overall process of water splitting is generically described. When the WE semiconductor is exposed to sunlight, photons with an energy equal or higher than the semiconductor band gap are absorbed and their energy is used to generate electron-hole pairs. If electrons and holes are successfully separated (depending on the separation efficiency η_{e^-/h^+}), they will be then transported to the respective reaction

sites. The holes drive the Oxygen Evolution Reaction (OER) at the n-semiconductor's surface, while the electrons are carried through the electrical wire to the cathode, where the Hydrogen Evolution Reaction (HER) takes place. The efficiency by which electrons reach the back contact and holes the surface is defined as $\eta_{transport}$. In order to oxidize water, holes need to be extracted from the semiconductor and injected into electrolyte. The efficiency of this final step is defined as $\eta_{interface}$.[4,11–14]

The set of equations that describes the overall process of water splitting is:

Photon-induced electron-hole separation $$4 \times \left[(e^{-}h^{+})_{\mathrm{VB}} \xrightarrow{h\nu} e^{*-}{}_{\mathrm{CB}} + h^{+}{}_{\mathrm{VB}}\right] \quad (2.1)$$

Oxygen Evolution Reaction (OER), at the anode $$2\mathrm{H_2O} + 4h^{+} \rightarrow 4\mathrm{H^{+}} + \mathrm{O}_{2(gas)} \quad (2.2)$$

Hydrogen Evolution Reaction (HER), at the cathode $$4\mathrm{H^{+}} + 4e^{*-} \rightarrow 2\mathrm{H}_{2(gas)} \quad (2.3)$$

Net PEC water splitting reaction $$2\mathrm{H_2O} + 4e^{*-} + 4h^{+} \rightarrow 2\mathrm{H}_{2(gas)} + \mathrm{O}_{2(gas)} \quad (2.4)$$

Where $(e^{-}h^{+})_{\mathrm{VB}}$ represents the unseparated electron-hole pair in the valence band of the semiconductor, while $e^{*-}{}_{\mathrm{CB}}$ is the electron excited to the conduction band by adsorption of a photon ($h\nu$) and $h^{+}{}_{\mathrm{VB}}$ the hole left behind in the valence band.

It is important to note that the two OER and HER half-reactions occur only when the electrodes are connected in a closed circuit (through the wire and the electrolyte they are immersed in), ensuring the exchange of charge carriers between the two.

However, not only the charge carriers have to be efficiently produced and available at the required reaction sites, but their energy must be sufficient to sustain the two half reactions. The standard Gibbs free energy of the net conversion process, ΔG^0, represents a thermodynamic minimum for splitting water at standard condition of 25°C and 1bar.

Standard Gibbs free energy $$\Delta G^{\circ} = +237{,}18\ \mathrm{kJ\ mol^{-1}} \quad (2.5)$$

It is a positive value, which means indeed that energy must be supplied for the reaction to occur.

The standard reversible potential is:

Standard reversible potential $$V^{\circ}{}_{rev} = \frac{\Delta G^{\circ}}{nF} = 1{,}23\ \mathrm{V} \quad (2.6)$$

$V^{0}{}_{\mathrm{rev}}$ is the difference between the potential of hydrogen reduction ($E_{\mathrm{H+/H2}}$=0,0V) and that of water oxidation ($E_{\mathrm{H2O/O2}}$=-1,23V). Hence, it is the minimum potential needed to sustain electrolysis of water. However, water splitting would not occur at this potential, since process losses need to be considered, as overpotential losses at the anode (OP_a) and at the cathode (OP_c).[13,15,16]

Operating voltage with overpotential losses $$V_{op} = V^{\circ}{}_{rev} + OP_a + OP_c \quad (2.7)$$

Therefore, the operating voltage, V_{op}, is normally higher than 1.23 V.

1.2.2. Semiconductor – electrolyte interface

The HER and OER half reactions can occur only if the photoexcited electron-hole pairs are efficiently separated and extracted from the semiconductor before they recombine. This is possible thanks to the electric field that is formed at the junction between semiconductor and electrolyte when the two are put into contact. The formation of this electric field arises from the equilibration of Fermi levels of semiconductor and electrolyte, as shown in Figure 4. Figure 4a shows photoanode and electrolyte before interaction. Since the semiconductor in this case is a n-type, its Fermi level (F_n) is close to the CB, while the Fermi level of the electrolyte (F_s) lays between the redox levels for hydrogen reduction ($E_{H+/H2}$) and water oxidation ($E_{H2O/O2}$). F_n is higher than F_s, therefore to reach equilibrium (Figure 4b-c) free electrons have to migrate to the interface, inducing a thin Helmholtz layer of negative charges in the electrolyte, while leaving positive fixed charges in the semiconductor, the space charged region (SCR). This causes an upward bending of CB and VB of the semiconductor in the region close to the interface and a built-in electric field which will drive photoexcited electrons toward a back contact and holes in the electrolyte.[17,18]

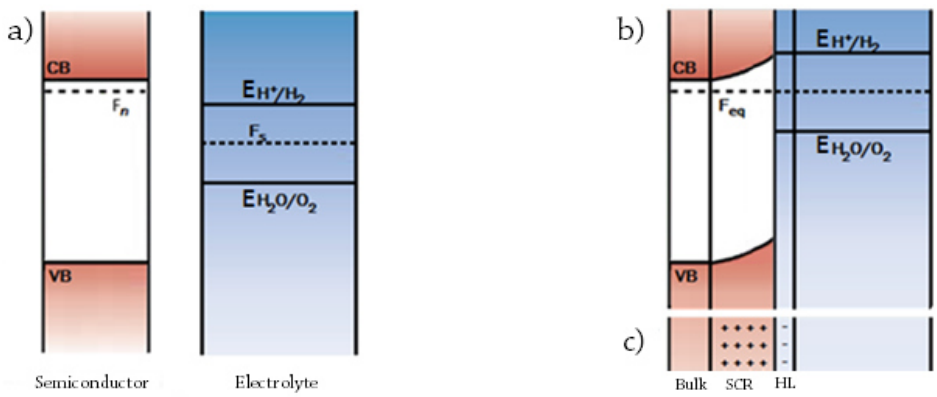

Figure 4: Formation of a semiconductor/electrolyte PEC junction based on an n-type photoanode. a) Semiconductor and electrolyte before contact; b) band diagram of junction formation and equilibration; c) charge distributions in the space charge region (SCR) and Helmholtz layer (HL). F_{eq} is the equilibration Fermi level.[18]

When light hits the photoanode, the thermal equilibrium at the junction is disturbed due to an excess concentration of photogenerated electron-hole pairs. As a result, the single Fermi level F_n splits into two quasi-Fermi levels, namely F_e for the electrons and F_h for the holes. The minority carries (holes, for a n-type semiconductor) distribution is significantly altered by the excess of electron-hole pairs, thus the quasi-Fermi level F_h shifts substantially to a lower energy, while the majority carrier distribution is almost unaffected, resulting in a slightly upward shift of the quasi-Fermi level F_e, as shown in Figure 5.

The Fermi level separation determines the actual energy that can be used to carry on the water splitting reaction. If this potential V_{ph} is sufficient to overcome the reversible potential plus anodic and cathodic overpotential (OP_a and OP_c), then water splitting will occur. On the other hand, if F_h is not low enough or the electropotential at the counter-electrode not high enough, the reaction will not take place. An applied voltage (a bias) is often used in the last cases, in order to provide the energy that the stand-alone system lacks.

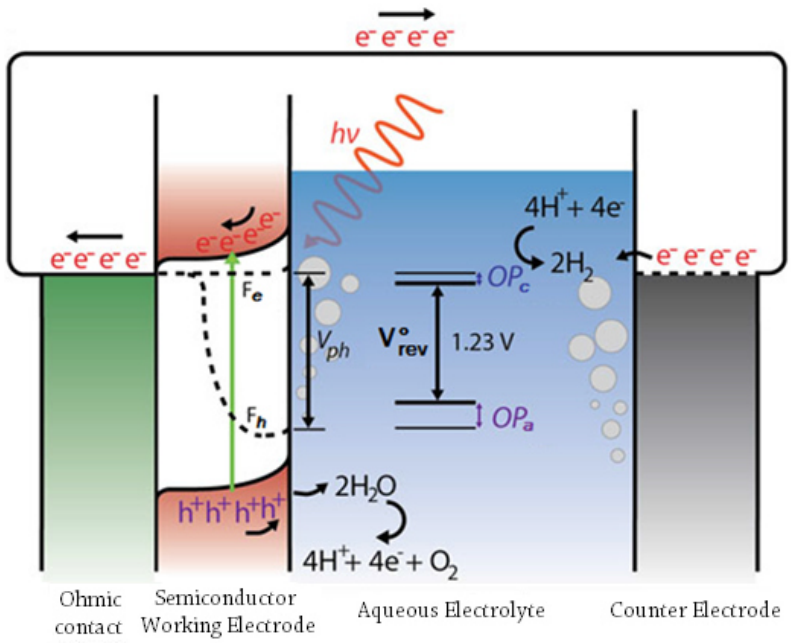

Figure 5: Band diagram of the photoanode PEC junction under solar illumination, illustrating the Fermi level split into two quasi-Fermi levels. V_{ph} is the separation between the two quasi-Fermi levels and is the usable energy for the PEC reaction, which will occur only if it overcomes the reversible potential (V°_{rev}) plus the anodic (OP_a) and cathodic (OP_c) overpotentials.[11]

1.2.3. PEC efficiencies

Several different kinds of efficiency (η) have been defined and each of them has a different place in PEC research.[11,13,18]

The overall conversion of solar energy into hydrogen (STH) is the most important parameter to define a PEC solar cell. It describes the overall efficiency of a PEC water splitting device exposed to broadband solar irradiance (AM 1.5 G) under zero-bias conditions. It is therefore the parameter used us to reliably compare different devices. STH efficiency is defined as the chemical energy of the hydrogen produced divided by the solar energy input from sunlight incident on the cell.

$$\text{STH }\% = \frac{P_{output}}{P_{input}} \times 100\% = \frac{chemical\ energy\ H_2\ produced}{solar\ energy\ input} \times 100\% = \frac{RH_2(mmol\ H_2\ s^{-1}) \times \Delta G^{\circ}(KJ\ mol^{-1})}{P_{tot}(mW\,cm^{-2}) \times A(cm^2)} \times 100\%$$

Where RH_2 is the rate of hydrogen production that can be measured directly by analytical methods like gas chromatography, ΔG° is the change in free Gibbs energy per mole of H_2 (237,18 KJ mol^{-1}), P_{tot} is the incident illumination power density and A the area of the illuminated electrode.

Quantifying the output power by directly measuring the amount of H_2 produced is not always ideal, therefore another equation can be used to express STH efficiency. In this case, the output energy is calculated by multiplying the voltage (V_{rev}) with the short-circuit photocurrent density (J_{sc}, normalized to the electrode area) and the Faradaic efficiency for hydrogen evolution (η_f):

$$\text{STH }\% = \frac{P_{output}}{P_{input}} \times 100\% = \frac{J_{SC}(mA\ cm^{-2}) \times V_{rev}(V) \times \eta_F}{P_{tot}(mW\,cm^{-2})} \times 100\%$$

As seen previously, when stand-alone PEC devices cannot provide enough current to sustain water splitting, a bias needs to be applied between the working and counter electrodes. In these cases a different efficiency value is used, defined as Applied Bias Photon-to-current Efficiency (ABPE):

$$\text{ABPE }\% = \frac{|J_{PH}(mA\ cm^{-2})| \times [V_{rev} - V_{bias}](V) \times \eta_F}{P_{tot}(mW cm^{-2})} \times 100\%$$

Besides these two expressions of overall performances, other efficiencies can be defined that will give us more specific information to understand the system and the interface performances of a specific semiconductor.

In specific, the Incident Photon-to-Current efficiency (IPCE) describes the photocurrent collected per incident photons as a function of incident wavelength. It is also defined as External Quantum Efficiency (EQE) and it takes into account the single efficiency of three fundamental steps that are involved in photoelectrochemistry: photon absorptance (defined as the fraction of electron-hole pairs generated per incident photon, η_{e^-/h^+}), charge transport to the solid-liquid interface ($\eta_{transport}$) and the efficiency of interfacial charge transfer ($\eta_{interface}$).

$$\text{IPCE}(\lambda)\ \% = \text{EQE}(\lambda)\ \% = \frac{electrons\ out}{photons\ in} \times 100\% = \eta_{e^-/h^+} \times \eta_{transport} \times \eta_{interface} \times 100\%$$

IPCE values are obtained from chrono-amperometry measurements: the PEC electrode is subjected to monochromatic light which changes wavelength with time and the current that arises is measured as a function of wavelength. The difference between the steady state current under illumination and the steady state background current is the photocurrent that arises due to reactions occurring at the surface of the semiconductor (J_{ph}). IPCE is therefore calculated as the ratio of this photocurrent converted to an electron rate (by multiplying J_{ph} for hc/e) versus the rate of incident photons (calculated from the monochromatic illumination power intensity multiplied to the λ at which P_{mono} is measured).

$$\text{IPCE}(\lambda)\ \% = \text{EQE}(\lambda)\ \% = \frac{electrons\ s^{-1}\ cm^{-2}}{photons\ s^{-1}\ cm^{-2}} \times 100\% = \frac{J_{ph}(mA\ cm^{-2}) \times \frac{hc}{e}(Vnm)}{P_{mono}(mW cm^{-2}) \times \lambda(nm)} \times 100\%$$

Therefore, every IPCE value is related to a specific value of λ and, if no applied bias is used in the measurement, the integration of IPCE values over the entire solar spectrum can provide an estimation of the maximum possible STH efficiency.

Finally, to understand the inherent performance of a material, it is helpful to subtract the losses due to photons that are reflected or transmitted, hence defining an efficiency that takes into account only the photons that are actually absorbed. This is the Absorbed-Photon-to-Current Efficiency (APCE) and it describes indeed the photocurrent collected per incident photon absorbed. It is also defined as External Quantum Efficiency and it is particularly useful for the characterization of thin films semiconductors, since it can be used to determine the optimum balance between maximal path-length for photon absorption and minimal effective transport distance for electrons and holes within the material.

$$\text{APCE}(\lambda)\ \% = \text{IQE}(\lambda)\ \% = \frac{IPCE\ \%}{\eta_{e^-/h^+}} = \frac{J_{ph}(mA\ cm^{-2}) \times \frac{hc}{e}(Vnm)}{P_{mono}(mW cm^{-2}) \times \lambda(nm) \times (1 - 10^{-A})} \times 100\%$$

Where the absorptance η_{e^-/h^+} is calculated as followed:

$$\eta_{e^-/h^+} = \frac{I_0 - I}{I_0} = 1 - \frac{I}{I_0} = 1 - 10^{-A} \quad \text{With A = - log(I/I}_0\text{).}$$

1.2.4. Ideal photoanode characteristics for water splitting

Semiconductors have the capability to conduct electricity when enough energy is provided to them. For the scope of water splitting, such characteristic is used to allow the water splitting reaction to occur, therefore to convert solar energy into chemical energy. How this is achieved has already been explained in the previous sections. The characteristics that a semiconductor should have in order to be considered a good candidate for PEC employment in the water oxidation half reaction are here explained.

First of all, as discussed in the previous paragraphs, the two half reactions need electrons and holes with enough energy to respectively evolve H_2 and O_2 from water. This is determined by the position of the band edges or, rather, of the quasi Fermi levels (see section 1.2.2) in respect to the water redox potentials.

An n-type photoanode should have a valence band maximum (VBM) potential more positive than the water oxidation potential $E_{O2/H2O}$ (VBM > +1.23V vs. RHE). If the conduction band minimum (CBM) potential is more negative than the hydrogen reduction potential $E_{H+/H2}$ (CBM < 0.0V vs. RHE), then the photogenerated electrons will also have enough energy to reduce water at the counter electrode[19], assuming faradaic efficiency. When this is not the case, a voltage will need to be applied in order to provide the needed amount of energy.

Such band edges requirements imply that the band gap has to be large enough to overcome the operative voltage, V_{op} (see equation 2.7). However, it should be considered that the ultimate goal is to store solar energy into chemical bonds. Since most of the solar spectrum lies in the visible region, small band gaps would absorb a bigger portion of the solar spectrum, while semiconductors with large bang gaps would absorb only in the UV region, making them a poor choice for solar to hydrogen conversion processes. The band gap of a semiconductor should therefore be large enough to overcome the water splitting operating voltage, but not too large, in order to absorb a big portion of the solar spectrum's visible region. A good band gap value is considered to be approximately 2.0-2.2 eV.

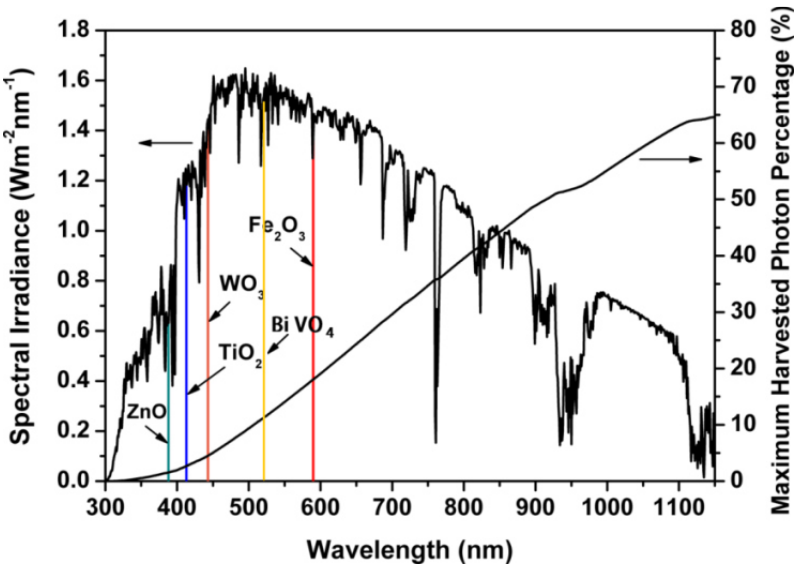

Figure 6: Solar spectrum with band gap position for few metal oxide semiconductors. The band gap represents the maximum value of wavelength (minimum energy) that can be absorbed by that specific semiconductor. For example, $BiVO_4$ will absorb wavelength shorter than 520nm. The black line shows how the maximum harvested photon percentage decreases with the increase of the semiconductor band gap position: the smaller the band gap, the higher the harvested photon percentage.[16,20]

Lastly, the fact that the semiconductor will be immersed in aqueous solutions and irradiated with light during its working lifetime should be taken into account. This means that the material has to be resistant to photoinduced corrosion. In fact, a compound semiconductor used as a n-type photoanode should have a VBM lower than $E_{O2/H2O}$. However, the photogenerated holes (h^+) may oxidize the semiconductor first, rather than water, making the compound decompose (Figure 7a).

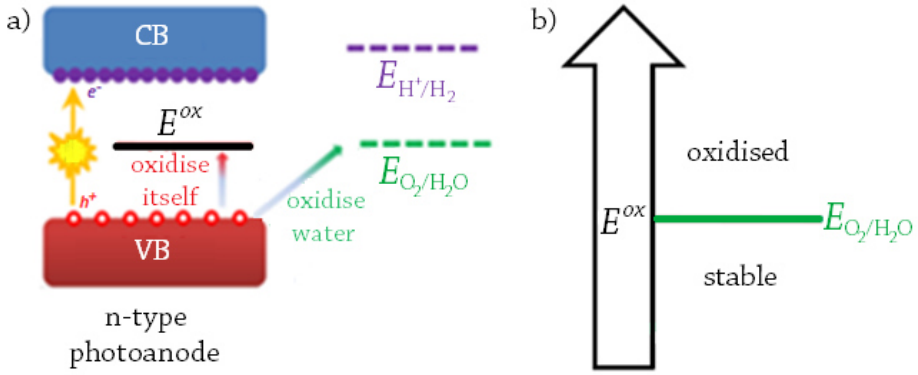

Figure 7: a) Schematic representation of the photogeneration of charge carriers in an n-type photoanode and the possible pathways that holes can undergo, oxidizing water or the semiconductor material itself. E^{ox} is the oxidation potential of the photoanode in aqueous solution. b) Schematic representation of the material stability dependence to the relative position of its oxidation potential to that of water oxidation.[21]

Whether the semiconductor is resistant to the photocorrosion depends on the position of its E^{ox} relative to the water oxidation potential, $E_{O2/H2O}$. In general, a semiconductor is stable with respect to the hole oxidation if its E^{ox} is situated at more positive values than $E_{O2/H2O}$ (Figure 7b).

To find a semiconductor that satisfies all these requirements it is therefore not easy. Metal oxides semiconductor materials are among the most studied photoanodes for solar water oxidation.[15] Several of them match all the criteria so far listed: they have suitable band gap sizes, a valence band maximum more positive than the thermodynamic potential for water oxidation and they're stable under photo-oxidation conditions. Additionally, they are inexpensive and abundant, a factor that would definitely make a difference when employed in large-scale systems. Furthermore, unlike non-oxide materials, many metal oxide semiconductors exhibit Nernstian behaviour. The conduction and valence band edge potentials shift of -0.059 V/pH in the same direction as the water oxidation and reduction potentials. As a result, the thermodynamic overpotentials for water splitting are pH independent, making them versatile for several different operating conditions.[20]

1.3. Material investigated: $BiVO_4$ as photoanode

Among all suitable semiconductors, the ternary metal oxide bismuth vanadate ($BiVO_4$) has been identified as one of the most promising photoanode materials. It has a band gap of 2.4-2.5 eV, which is only slightly larger than what is normally desired and its VB edge potential is located at ca. +2.5-2.6 eV vs. RHE, which makes it suitable for the water oxidation reaction. The CB edge potential is located at +0.1-0.2 eV, just short of the thermodynamic level for H_2. However, this translates into a modest photocurrent onset potential of +0.25V vs.

RHE,[22–25] much lower than those needed with other metal oxide semiconductors like Fe_2O_3 and WO_3 which photocurrent onset potential are +0.8V and +0.5V, respectively.[15,26,27] Such characteristics implicate a theoretically photocurrent generation of 7.5mAcm^{-2}, with AM1.5 illumination, assuming all photons with energies higher than the band gap are absorbed and that the generated charges are transported with faradaic efficiency. This would correspond to a STH energy conversion efficiency of 9% .[24,25,28]

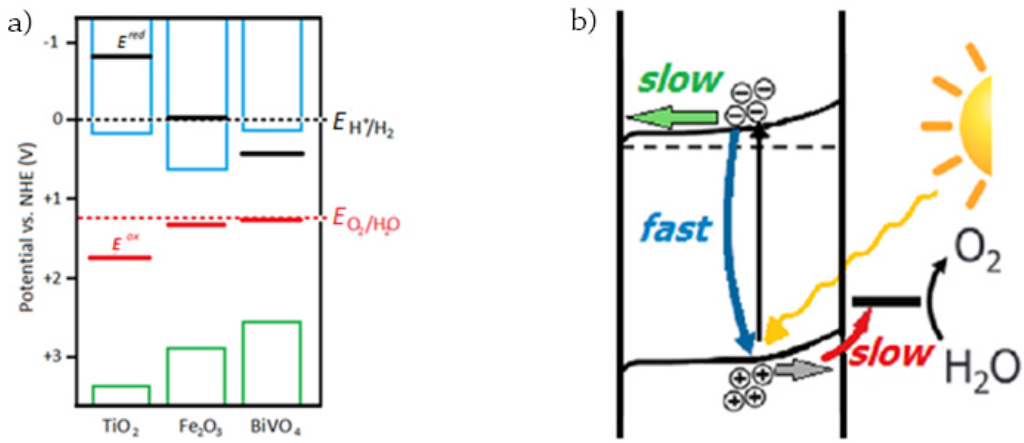

Figure 8: a) Diagram of band edges positions and redox potentials for few metal oxide semiconductor materials. The water redox potentials $E_{O2/H2O}$ and $E_{H+/H2}$ (dashed lines) and the valence (green columns) and conduction (blue columns) band positions. The red bars are the E^{ox} of the semiconductor while the black bars are their reduction potential, E^{red}. All values are relative to the NHE for semiconductors in solution at pH=0, ambient temperature, and pressure 1 bar.[21] b) Schematic representation of $BiVO_4$ intrinsic problems: slow electron mobility, fast electron-hole recombination and slow surface kinetics for water oxidation.

However, despite its promising characteristics, the typical efficiencies of unmodified $BiVO_4$ photoanodes for water oxidation were found to be ten times worse than its actual potential. This is caused by a fast electron–hole recombination, its poor charge transport properties due to slow electron mobility, and slow surface kinetics for water oxidation. Therefore, various strategies have been developed to decrease these limitations.

One of the reasons that reduces $BiVO_4$ performance may come from the presence of defect trapping states that act as recombination centres for charge carriers. These defect states can be in the bulk of the material, at the interfaces with the back contact or at the surface. Liang et al. claimed the presence of defect state at the back contact that causes accumulation of negative charges at the FTO/$BiVO_4$ interface.[29] According to them, the electrons subsequently generated are repelled by this negative charge present at the back and remain in the bulk. Such high concentration of negative charges in the bulk reduces the space charge region (see Figure 4) and thus decreases the bending of the bands. The electric field which forces the holes to reach the $BiVO_4$/electrolyte interface is also reduced. Hence, holes are more likely to recombine with the electrons trapped in these defect states. To solve this problem, they found that the addition of a SnO_2 interfacial layer between FTO and $BiVO_4$ prevented the photogenerated holes from reaching the electrons in the defect state, resulting in less recombination and higher collection efficiency.

Another cause of low efficiencies can also be the formation of a Schottky barrier when the back contact is not perfectly ohmic, preventing a good conduction of charge carriers between FTO and semiconductor. Cooper et al. have calculated a work function of 4.79 eV for $BiVO_4$,[30] while Hwang et al. reported for FTO values of 4.70 eV.[31]

This implies that $BiVO_4$ should form an ohmic contact with FTO, excluding this as a problem in charge collection at the back contact.

Other strategies can be adopted to improve a semiconductor photoperformance, including the introduction of a dopant, modifications of its morphology, the coupling with other semiconductor materials or the deposition of a catalyst for water oxidation at its surface.

The state-of-the-art $BiVO_4$ photoanode has been synthetized in Delft, by Abdi et al.[22] They introduced tungsten as a dopant in a gradient concentration through the film thickness, creating a distributed n^--n^+ homojunction, which increased the carrier separation efficiencies up to 80%. By combining this gradient W:$BiVO_4$ photoanode with an earth-abundant cobalt phosphate water-oxidation catalyst and a double-junction amorphous Si solar cell in a tandem configuration, a photocurrent of 4 $mAcm^{-2}$ was achieved under 1 Sun illumination.

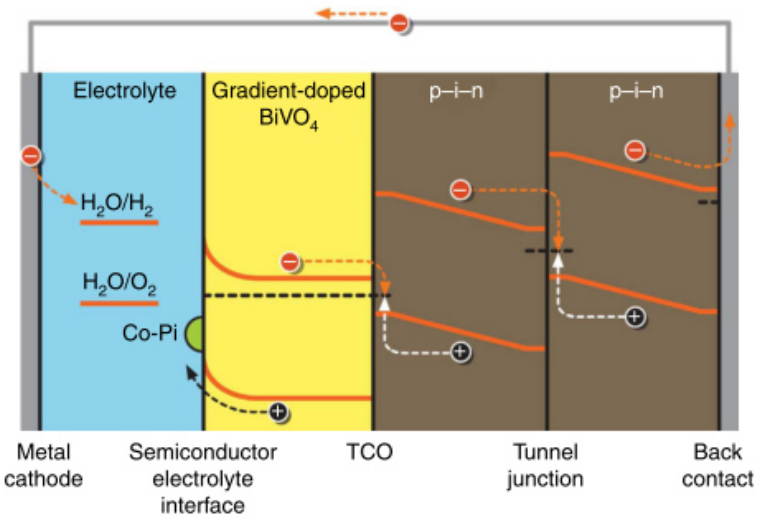

Figure 9: State of the art gradient doped W:$BiVO_4$ photoanode with an earth-abundant cobalt phosphate (CoPi) water oxidation catalyst and a double-junction amorphous Si solar cell in a tandem configuration. TCO is a transparent conductive oxide, consisting of three layers: Fluorine-Tin-Oxide in contact with the photoanode, glass and Indium-Tin-Oxide in contact with the Si cell.[22]

Before moving to the aim of this research project, a brief review of crystal and electronic structure of $BiVO_4$ is here provided, since a good understanding of these characteristics is critical in developing effective strategies to improve the photoelectrochemical properties of this material.

1.3.1. Crystal structure and electronic properties

$BiVO_4$ is known to exist in three polymorphs: orthorhombic pucherite, tetragonal dreyerite, and monoclinic clinobisvanite.[32] Of these three structures, only the thermodynamically stable monoclinic phase exhibits good photoelectrochemical behaviour.[24,33–36] The phase transition to the monoclinic clinobisvanite irreversibly occurs at 400°C.[34,35]

Its space group is C2/c, and point group is C_{2h}^{6}. This structure contains 4 bismuth atoms, 4 vanadium atoms, and 16 oxygen atoms in a unit cell. The V site is surrounded by four oxygen atoms forming a VO_4 tetrahedron, while the Bi site is surrounded by eight oxygen atoms forming a BiO_8 dodecahedron. The metal atoms are connected with the adjacent metal atoms of the same kind to form a continuous zigzag line on the $(22\bar{1})$ plan, whose distances are about 3.85A˚ . Thus, the BiO_8 dodecahedra share an edge with each other, forming chains that are parallel to the direction of $[1\bar{1}0]$, while VO_4 tetrahedra do not come into contact with other VO_4, but they are connected with BiO_8 dodecahedron through a shared oxygen atom, which results in every BiO_8 being surrounded by eight isolated VO_4 tetrahedra as depicted in Figure 10.[36]

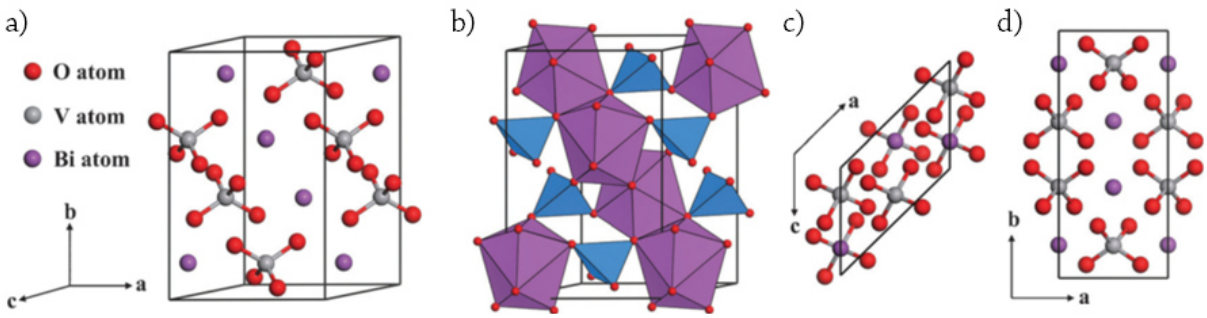

Figure 10: a) Crystal structure of monoclinic clinobisvanite $BiVO_4$. b) The corresponding polyhedron structure, with VO_4 tetrahedra in blue, and BiO_8 dodecahedra in purple. c) Top view and d) side view of the structure.[36]

Zhao et al. have calculated the presence of four types of Bi–O bond, and two types of V–O bond.[36] While Payne et al. have found three pairs of Bi-O bond lengths and two pairs of V-O bond lengths.[37] Either ways, this implies that VO_4 tetrahedron and BiO_8 dodecahedron are slightly distorted. The distortion of the dodecahedra can enhance the lone-pair impact of Bi 6s states, while the tetrahedral distortion results in positive and negative charges being located in separated points. This creates an internal electric field, which enhances the separation of electron-hole pairs. Therefore, these structure distortions are the reason why the monoclinic structure is the photoactive phase of $BiVO_4$ among the others. Indeed, the other $BiVO_4$ structures (orthorhombic pucherite, and tetragonal dreyerite), have completely symmetric polyhedra, which results in negligible photocatalytic activities.[36]

The stoichiometry of the system implies formal oxidation states of 3^+ for Bi ($5d^{10}6s^2$), 5^+ for V ($3d^0$), and 2^- for O ($2p^6$).

The ion-projected valence electronic densities of states (DOS) according to the calculation of Walsh et al.[38] are reported in Figure 11a. These calculation are well in accord with those from other researcher.[36,37,39] The highest occupied state is set at 0 eV. The band that extends from -5 eV to 0 eV is the valence band and it is mainly composed by O 2p. V makes only a small contribution to the valence density of states, because of its elevated oxidation state and formal d^0 configuration. However, hybridization with O 2p around -3.5 eV is observed. Furthermore, a closer inspection of the O 2p valence band indicates the presence of Bi 6s and Bi 6p states at the top and bottom, respectively. The conduction band is calculated to be at energies higher than 2 eV and is found to be dominated by V 3d states, with the presence of significant contributions also from O 2p and Bi 6p. An additional peak is by them found at -9.5 eV, consisting of the majority of Bi 6s states.

The band structure estimated from the DOS and drawn along the Γ-A-M lines of the Brillouin zone is shown in Figure 11b. The calculated direct band gap along the A line is of 2.16 eV, which underestimates the experimental values reported of 2.4-2.5 eV. The band edges show little curvature, but they are far from being parabolic. As a consequence, they are not well described by the effective mass approximation normally applied to semiconductors.

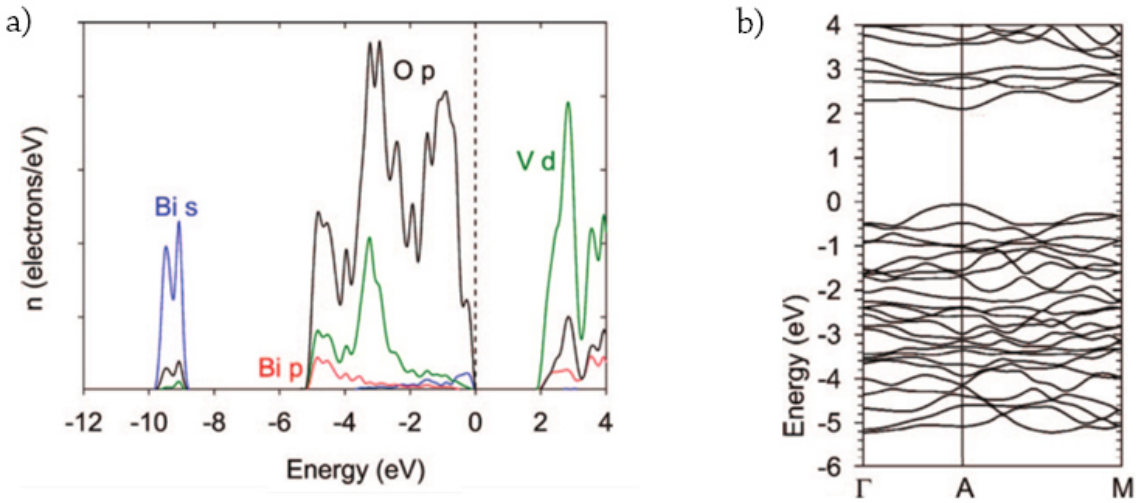

Figure 11: a) DOS of BiVO4, with the highest occupied state set at 0 eV calculated by Walsh et al. The conduction band is predominantly constituted by V 3d orbitals, while the valence band by O 2p orbitals. b) Electronic band structure along the Γ-A-M lines. Here only valence and conduction band are depicted excluding the band centred at -9.5 eV.[38]

If we compare the calculated electronic density of states (DOS) with the crystal structure we can already make some prediction on $BiVO_4$ charge transport. Since the conduction band mainly consists of V 3d orbitals but the VO_4 tetrahedra are not interconnected with each other (see Figure 10), the electrons in the conduction band have to 'jump' between VO_4 tetrahedra. This results in poor electron transport properties for $BiVO_4$ electrodes.

2. Research Project Aims

2.1. Strategies to enhance $BiVO_4$ performance

As already stated, the characteristics of $BiVO_4$ make it a promising material as a photoanode for water splitting, but the efficiencies of bare electrodes have proved to be lower than expected. The reasons behind these low performances, summarised in Figure 8b, are related to a very fast recombination of charges, poor electrons transport efficiency and slow transfer kinetics for water oxidation at the interface. These limitations can be reduced to a certain extent with different strategies and some of them have been already mentioned earlier.

The first goal of this project was to synthetized $BiVO_4$ thin films and to improve their performances by three main expedients. First of all, the increase of film thickness was investigated, as a tactic to enhance the amount of charges generated. Furthermore, a co-catalyst with high water-oxidation kinetics was deposited on the electrode surface and, finally, the addition of a dopant to the bulk of the film was also employed.

The three expedients used during this project are here described more in depth, in order to give a better understanding of how they can affect the photoelectrochemical properties and performances of $BiVO_4$.

2.1.1. Thickness

Only photons with enough energy to overcome the band gap of a semiconductor can be absorbed by it. Those that are not absorbed are transmitted through the material and some photons get reflected from the top surface.

The photons that are actually absorbed penetrate the semiconductor till a certain depth before releasing their energy to an electron, depending both on the material and on the energy of the photon itself. The absorption coefficient (α) is a value dependent on these two factors and it allows the quantification of the absorption depth. The absorption coefficient is related to the extinction coefficient (k) and to the wavelength (λ) by the relation:

$$\alpha = \frac{4 \cdot \pi \cdot k}{\lambda} \tag{4.1}$$

The relationship between absorption coefficient and wavelength makes it so that different wavelengths penetrate different distances into a semiconductor before most of the light of that specific wavelength is absorbed. The absorption depth is a useful parameter which gives the distance into the material at which the light drops to about 36% of its original intensity and it is given by the inverse of the absorption coefficient:

$$\text{Penetration depth} = \alpha^{-1} \tag{4.2}$$

Any electron that successfully absorbs a photon is therefore excited to the conduction band. However, this electron is in a meta-stable state and will eventually stabilize to a lower energy position, if not extracted from the semiconductor quickly enough. When the electron stabilizes back down into the valence band, it also effectively removes a hole. This process is called recombination.[40]

Recombination can take place in the bulk of a semiconductor or at its surface and it is a process that can occur with different mechanisms. The susceptibility to recombination is often expressed as the carrier lifetime, τ. The diffusion length of a charge carrier, L_d, is the distance the carrier can cover before recombining and it is related to the carrier lifetime through:

$$L_D = \sqrt{D\tau} \tag{4.3}$$

Where D is the diffusion coefficient.[4,41] The diffusion coefficient is related to the carrier mobility, μ ($m^2V^{-1}s^{-1}$), by the Einstein relation:

$$D = \frac{\mu k_b T}{q} \tag{4.4}$$

Therefore, the diffusion length of, for example, the minority charge carriers in an n-type semiconductor, namely the holes, will be defined as:

$$L_h = \sqrt{D\tau} = \sqrt{k_b T \mu_h \tau_h} \tag{4.5}$$

Where the charge of a hole, q_h, is equal to 1, therefore has been neglected from the equation above.[16,42] The same equation can be written for the diffusion length of an electron.

The difference in carrier mobility, hence the difference in diffusion length between electrons and holes can be experimentally verified by comparing photocurrents obtained by back-side and front-side illuminations. Back-side illumination generates electron-hole pairs near the back contact, which is where electrons are collected to be sent to the counter-electrode, while front-side illumination generates electron-hole pairs near the electrode surface at the junction with the electrolyte, where holes are used. Different studies have reported that bare $BiVO_4$ electrodes generate a higher photocurrent with back-illumination than that with a front-illumination, indicating that diffusion lengths are shorter for electrons than for holes.[22,43–45] In particular Rettie et al. have calculated a diffusion length for holes in a $BiVO_4$ single crystal of 100 nm.[46]

This implies that film thickness has an important role in the efficiency of a semiconductor. To build a good cell, the electrode should be thick enough to absorb most of the incident light, in order to achieve sufficient photogenerated charge carrier concentrations. At the same time, as we just explained, the semiconductor cannot be too thick, depending on the diffusion length of the charges. To maximize charge carrier generation and collection, the thickness of the semiconductor should be on the order of the optical penetration depth. Considering that a thickness of α^{-1} corresponds to 63% absorption of incident light, the excess of material we would have for a film thicker than α^{-1} will add ohmic resistance to the cell and enhance the likelihood of carrier recombination, decreasing therefore their lifetimes, with little gain in absorption.[4,11,42]

2.1.2. Deposition of a co-catalyst for oxygen evolution

Even when the photogenerated electrons and holes possess thermodynamically sufficient potentials for water splitting reaction, they may recombine on the surface of the semiconductor if there are no suitable active sites available. This is the reason why it is necessary to facilitate the reactions on the surface through catalytic processes.

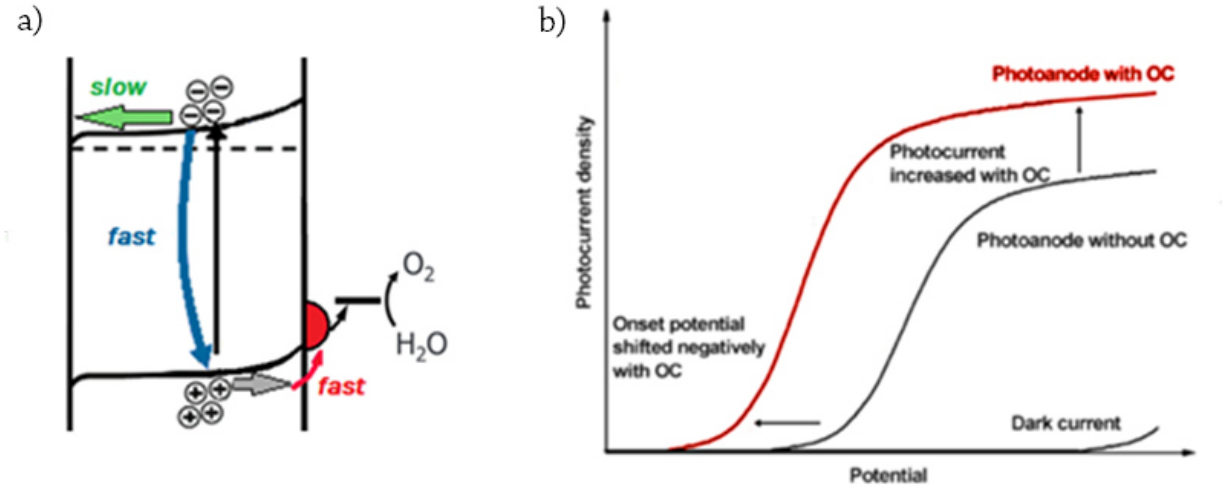

Figure 12: a) Effect of the deposition of a co-catalyst for water oxidation on a photoanode in the charge carrier transport. Specifically, the efficiency of holes injection into water is enhanced. The red semicircle represents the deposited co-catalyst. b) Comparison of the photocurrents produced by applying a potential on a photoanode with (red) and without (black) a deposited co-catalyst. As shown, both onset potential and photocurrent can be increased by the loading of a co-catalyst on the surface of the electrode.[47]

Loading oxygen-evolution catalysts (OEC) on semiconductors can increase surface kinetics by providing sites for the photogenerated holes at the surface, where their injection into the electrolyte will be more facile, while recombination with electrons will be reduced drastically (Figure 12a). The suppression of charge recombination and reverse reactions results in an enhanced efficiency. As shown in Figure 12b, the presence of a co-catalyst on a photoanode can both enhance the photocurrent density and result in a negative shift of the onset potential.

The most commonly OEC that has been used to improve water oxidation kinetics of $BiVO_4$ photoanodes is CoPi. Studies on $BiVO_4$/CoPi photoanodes indeed reported that the presence of this co-catalyst enhanced the magnitude of photocurrent, shifted the photocurrent onset potentials in the negative direction and increased the stability of $BiVO_4$ photoanodes.[20,48] The role of CoPi on both bare and doped $BiVO_4$ was found to be the reduction of the surface recombination by efficient hole extraction from the semiconductor layer and an efficient hole consumption for water oxidation.

Kanan et al. reported a model for the electrochemical deposition of such Co-phosphate species on an inert indium as well as a model of its role in the enhancement of oxygen evolution at the electrode surface. Such a catalyst forms upon the oxidative polarization of a phosphate-buffered electrolyte containing cobalt(II) ions. By means of a variety of techniques, they were able to conclude the presence of phosphate in an approximate 1:2

ratio with cobalt. Furthermore, they assume that the pH dependence of the catalytic activity of such material implicates the hydrogen phosphate ions as the proton acceptor species in the oxygen-evolution reaction. A scheme that summarizes their findings is depicted in Figure 13.

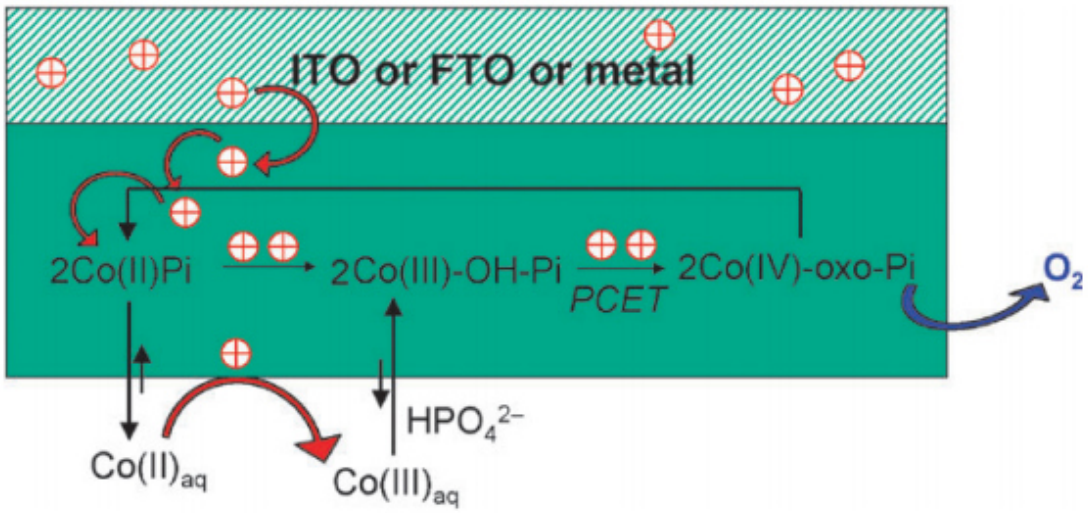

Figure 13: A model of the functioning of the cobalt phosphate (CoPi) as oxygen evolution catalyst, proposed by Kanan et al.[49]

The effectiveness of the CoPi catalyst can be estimated by comparing the photocurrents for the oxidation of hole scavengers, like Na_2SO_3 or H_2O_2, and photocurrents for water oxidation with the CoPi:$BiVO_4$ photoanode. An hole scavenger is a species that has much faster interfacial hole-transfer kinetics than that of water. That is to say, an hole scavenger oxidizes much faster than water. This implies that in the presence of such species in the electrolyte, it can be assumed that 100% of the holes that reach the interface will be successfully extracted and consumed. Ideally, an efficient OEC should improve the hole transfer kinetics at the interface in such extent to reach the same photocurrent generated in the presence of an hole-scavenger.

2.1.3. Doping

The intentional introduction of impurity atoms into a material is defined as doping and it can dramatically change the electrical and optical properties of the host, both in a favourable and a negative way.[50] Doping can indeed cause an increase in carriers density, modification of effective masses and mobilities of the charges and enhancement of local electric field nearby the dopant ions. However, doping can lead to an increase in electron-hole recombination phenomena, as it could impede charge transport by providing scattering centres, and decrease the width of the depletion layer. Therefore, in order to enhance the overall performance of the photoelectrodes, it is fundamental to identify the appropriate dopants and the optimal concentration needed.

In the case of an n-type semiconductor like $BiVO_4$, for each impurity atom of valence 6, like W^{6+} that is substituted to a V^{5+} in the lattice, there will be one valence electron left over. That's why dopant atoms as W for $BiVO_4$ are called donors. Such increase of electron density raises the Fermi level of the n-type $BiVO_4$, increasing

the difference between the Fermi level and the redox potential of the electrolyte, and resulting in a more significant band bending in the space charge region. Moreover, by increasing the concentration density of electrons, the electrical conductivity of the photoelectrode is also affected, since

$$\sigma \text{ (conductivity)} = e\, n\, \mu \tag{4.6}$$

Where e is the electronic charge, n is the concentration of charge carriers, directly dependent on their density, and μ is their mobility.

Another possible effect of doping is the creation of a local electric field around the dopant ions that may serve favourably for electron-hole separation. When a dopant atom substitutes a V atom in the crystal structure, the lengths of the V-O bonds will be different from the dopant-O ones. These two factors will induce lattice strain and creates an internal electric field. This local enhancement of electric field nearby the dopant ions will facilitate the electron-hole separation in the space charge region. However, if the dopant is present in too high concentration the lattice of the semiconductor material will be affected to strongly, with negative consequences on it photoactivity.

W and Mo have been reported to be dopants that most significantly enhance the photoelectrochemical performances of $BiVO_4$.

Ye et al. performed a screening of $BiVO_4$ doped with several metals for a certain range of concentrations and found that W, among the metals tested, was the only one showing an increased photocurrent and IPCE. In particular, the sample with a Bi/V/W ratio of 5.1/3.9/1.0 and oxidation state +3/+5/+6 was the one that exhibited the best performance. The element ratio and oxidation state were confirmed by XPS analysis, while the solution prepared to make such samples actually contained 4.5/5/0.5 ratios of Bi/V/W respectively.[51,52]

Luo et al. also prepared $BiVO_4$ electrodes doped with Mo^{6+} or W^{6+} and Sn^{4+} (Sn^{4+} as an acceptor dopant of Bi^{3+}) metal ions and observed that only doping with Mo^{6+} or W^{6+} enhanced the photocurrent. The observed improvement was attributed to the increased conductivity and a possible extension in the hole diffusion length.[53]

Consecutive doping of W and Mo into the $BiVO_4$ was found to dramatically increase the photo-oxidation current of water on the $BiVO_4$ electrode, showing higher photocurrents than $BiVO_4$ doped with only Mo or W.[54]

Abdi et al. have synthesized a $BiVO_4$ photoanode with a 10-step gradient in W doping, starting from 1% W at the interface with the back contact to 0% W at the semiconductor/electrolyte interface.[22] According to them, the presence of a gradient extends the presence of band bending over the entire thickness of the sample, resulting in a carrier-separation efficiency increase of 60% at 1.23V vs. (RHE) compared to 38% for homogeneously doped $BiVO_4$.

The dopant of choice for this research was W and it was added to the precursor solutions in different concentrations, in order to investigate the optimal amount for the specific synthesis procedure employed.

2.2. Charge carrier dynamics investigation

With the help of these and other expedients, the performance of $BiVO_4$ can be substantially increased, but even the state-of-the-art photoanode so far synthetized has still efficiencies way below its fullest potential. In order to give an insight to the intrinsic reasons behind the material problems and to contribute to the on-going research aimed at further optimize $BiVO_4$ efficiency, this project aims to further investigate charge carrier dynamics. This was accomplished by means of a transient absorption spectrometer.

Generally, transient absorption spectroscopy measures the variation in absorption of a sample as a function of time. In a typical experiment, the sample is first hit by a pulsed laser (pump) and promoted to an electronically excited state, while a second laser that measures the absorbance (probe) is sent through the sample with a delay respect to the pump. The absorption spectrum of the excited sample minus the absorption spectrum of the ground state is then calculated, a ΔA. By changing the delay time between the pump and the probe and recording a ΔA spectrum, a ΔA profile as a function of delay time is obtained. The final output is therefore a three-dimensional plot of ΔAbsorbance as a function of delay time(s) and wavelength (λ), a $\Delta A(\lambda,s)$ (Figure 14a).

A ΔAbsorbance spectrum obtained from such spectrometer contains mainly two contributions, as evident in Figure 14b. The first is by ground-state bleach, a negative signal. When the pump hits the sample, a fraction of the ground state species has been promoted to the excited state, therefore their concentration has decreased. This means that the ground-state absorption in the excited sample is now less intense than that of the reference. Consequently, a negative signal in the ΔA spectrum is observed in the wavelength region of ground state absorption. A second contribution is provided by excited-state absorption. Once the pump hits the sample, electrons from the valence band of the semiconductor are promoted to the conduction band, leaving a positive hole behind. Therefore, the excited state is now populated due to the photo-generation of these hole-electron charge carriers. Optically allowed transitions from these excited states to higher excited states may exist in certain wavelength regions, which implies that absorption of the probe pulse at these wavelengths occurs. As a consequence, a positive signal in the ΔA spectrum is detected. However, these excited states are transient species, i.e. their concentration decays in time after the excitation. This is due to the fact that the electrons and holes eventually recombine through different pathways or are injected into the external circuit. Such decrease in excited species concentration translates in an absorbance signal that decreases in time. This is shown in Figure 14c, where we can see the decay of absorption in time for a selected wavelength. Hence, this spectrometer allows to investigate the decay phenomena of excited species in $BiVO_4$ samples and by fitting the kinetics (decay profiles) the lifetime of such species can be extrapolated.

Other possible contributions to the ΔA spectrum are the further excitation of excited species, or a negative signal due to stimulated emissions. Stimulated emission is related to the fluorescence spectrum of the sample and it is expected to be Stokes shifted respect to the bleach.[55]

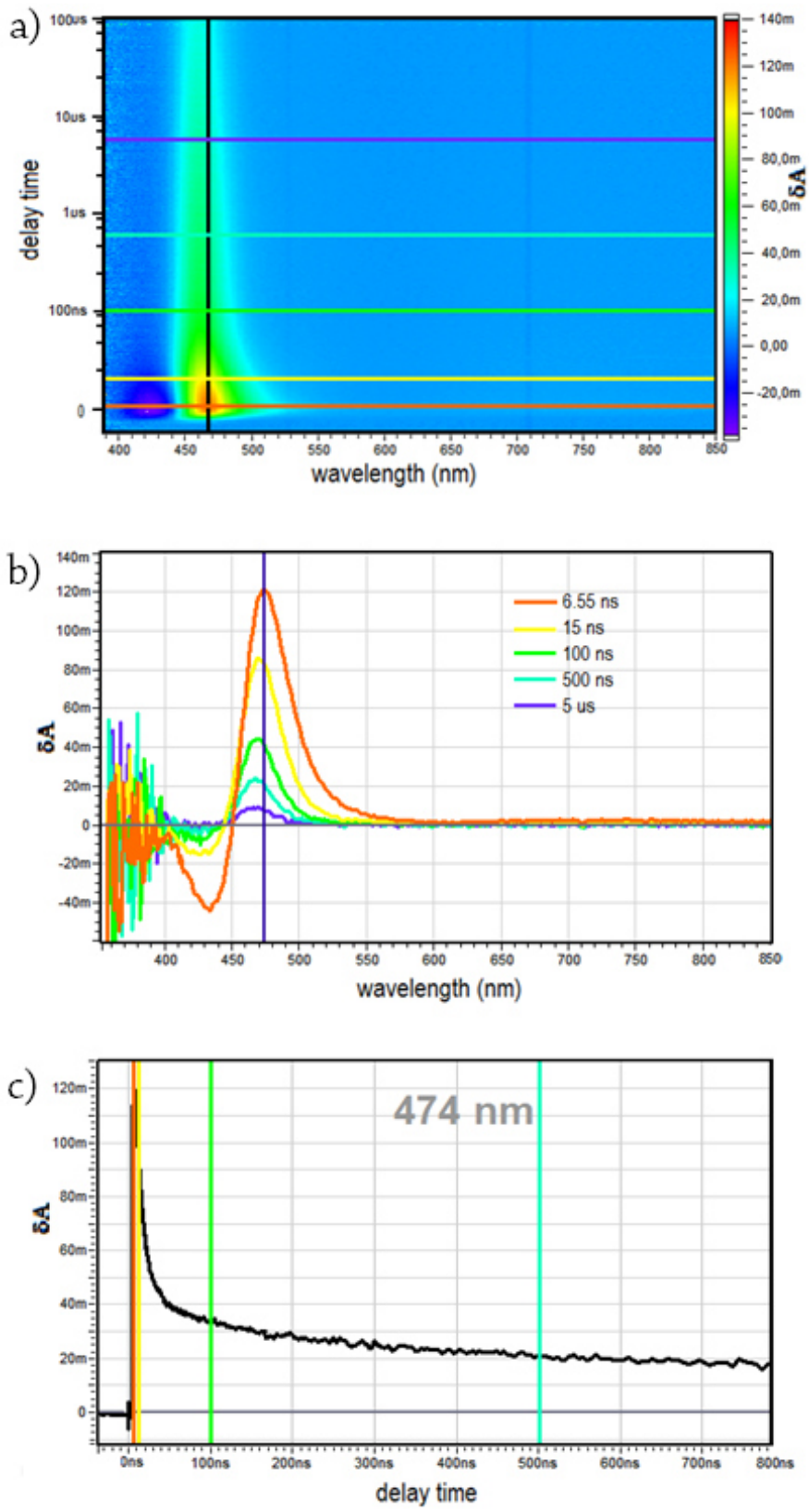

Figure 14: a) 3 dimensional plot of ΔA as a function of delay time (vertical axes) and wavelength (horizontal axes). The vertical scale on the right side of the graph represents the ΔA z-axes. The spectra at each selected delay time marked by a horizontal coloured bold line are reported in b), while the black vertical bold line is a selected wavelength (474 nm), which decay in time is reported in c).

3. Methods

3.1. Synthesis method: Metal Organic Decomposition

The synthesis method employed for the preparation of $BiVO_4$ thin film electrodes in this research is metal organic decomposition (MOD).

The first step of this technique consists of the dissolution of organometallic species containing the desired ions, followed by the deposition of the obtained solution on a conducting substrate (F-doped tin oxide, FTO) by means of spin coating or spray pyrolysis. The film is then heated at relatively high temperatures (350-500°C) at which the organometallic precursors decompose, leading to the formation of inorganic $BiVO_4$. For spin coating deposition methods the heating phase occurs after deposition, while spray pyrolysis techniques involve the decomposition of the organic phase contemporary to deposition, as it is explained more into detail in the following section. The final product is obtained by annealing for longer times at 480-500°C, at which stage features like crystallinity and further removal of organic residual take place.

Prior both deposition methods, the FTO substrate needs to be cleaned to ensure the formation of a good contact with the semiconductor. This was done with a three steps procedure. First, by sonication in a solution of equal parts of deionized water, acetone and ethanol. Then, a second sonication step was carried in a 0.1 HCl solution. Both sonication steps were carried on for 20 minutes. Finally, the FTO substrate was cleaned in a UV/ozone ProCleaner™ Plus for 20 minutes.

3.2. Deposition methods

3.2.1. Spray pyrolysis

Spray pyrolysis is the first deposition technique that was used to attempt the synthesis of $BiVO_4$ thin films.

Typical spray pyrolysis equipment consists of a precursor solution injector, an atomizer, a substrate heater, with temperature controller, a flow meter and an air pressure regulator. A scheme of the setup is represented in Figure 15, which resemble the one used during this project. Spray pyrolysis thin film synthesis can be divided in three main steps. First of all, the precursors solution is atomized. Different kinds of atomizer can be employed: air blast, where the liquid is exposed to a stream of air, ultrasonic, in which ultrasonic frequencies produce the short wavelengths necessary for a fine atomization of the precursors, and electrostatic, where the liquid is exposed to a high electric field.[56,57] Then, the droplets are transported to the substrate, while the evaporation starts to occur.

Finally the evaporation completes while the droplets spread on the substrate and the decomposition of the precursors initiates crystallization reaction and film growth.

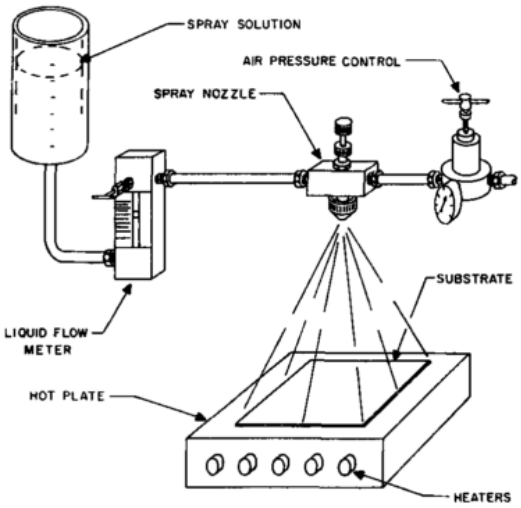

Figure 15: Typical spray pyrolysis setup. The solution is prayed through a nozzle onto a heated substrate. The flow of the liquid, the air pressure and the substrate temperature can be adjusted to obtained optimal results.[58]

In the work of Siefert the changes that precursor undergoes while moving toward the substrate are analysed.[59] Depending on droplet initial size and speed and on the temperature of the substrate the generated aerosol can undergo different processes, which are depicted in Figure 16. In case (A) large droplets reach the substrate and the evaporation of the solvent is complete only after impact. After vaporization a dry precipitate is formed. Furthermore, during vaporisation the substrate temperature drops since the process requires heat, this negatively affects the reaction kinetics. Besides, this process has a feeble sticking probability. In case (B) evaporation starts to occur earlier. As the droplet approaches the surface, a precipitate as an amorphous salt is formed and a dry precipitate hits the substrate with randomised distribution, where then decomposition occurs. Some of these particles will then evaporate and condense into gaps between other particles which have not evaporated. The process (C) leads to the optimum film properties. The solvent is entirely vaporized from the droplet before reaching the substrate, leaving a particle still in air. This particle absorbs heat from the ambient and sublimes when hitting the substrate, where a heterogeneous reaction takes place on the surface. In the case (D) the sublimation of the particle occurs too early and homogeneous reaction occurs in the vapour phase, forming a powder which will be deposited on the substrate, instead of a thin film.

Which one of the four cases depicted will occur depends on the initial droplet size and speed and on the temperature of the heating plate, which will influence the gradient of temperatures that the droplet will go through before reaching the substrate. Therefore film quality will depend on the arrangement of parameters that will be set on the spray pyrolysis system.

The available setup was a custom-made system and several adjustments had been necessary in the course of the project. However, several combinations of solvents, precursors' concentrations, solvent flow rate, air flow and heating plate temperature were tuned while attempting to synthetize homogeneous $BiVO_4$ thin films.

Unfortunately, none of the attempted procedures seemed to be successful. A table with a summary of the different procedures employed is presented in the result section 4.2.1.

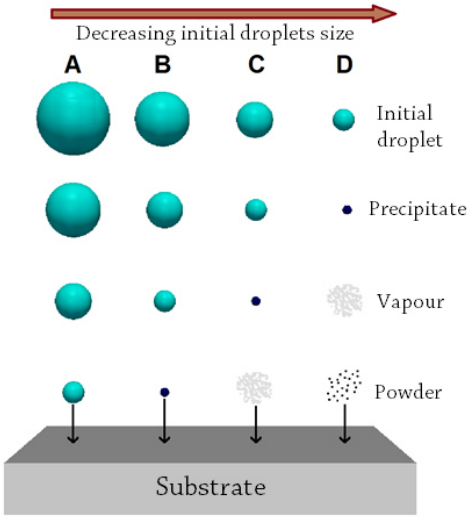

Figure 16: Four potential cases which the droplet can undergo during spray pyrolysis deposition as it is traveling towards the substrate.[59]

3.2.2. Spin coating

Spin coating is another technique that can be used to obtain a thin film evenly distributed across the surface of a substrate. The spin coater used to prepare the $BiVO_4$ samples during this project was an EMS Model 4000 Photo Resist Spinner. The procedure consists in casting a solution containing the precursors of the desired material on the centre of a spinning substrate (FTO glass). The high speed rotation creates a centripetal acceleration that, combined with the surface tension of the solution, spreads the liquid to the edges of the substrate into an even covering, leaving a thin film on the substrate's surface. A drying step at room temperature removes the excess of solvent from the film (Figure 17). Subsequently, the substrate with the solution film is placed on a heating plate, where the organic components are decomposed and a film of the inorganic material is formed.

Final film thickness and other properties will depend on the nature of the solution (viscosity, drying rate, concentration, surface tension, etc.) and the parameters chosen for the spin process, such as rotational speed, acceleration and process duration. Slight variations of these parameters will result in different coated films and, since reproducibility is an important aspect in the preparation of thin films employed in photoelectrochemical cells, it is fundamental to find the optimal coating parameters and conditions.

Spin speed is one of the most important factors in spin coating. The speed of the substrate (RPM) affects the degree of centrifugal force applied to the liquid as well as the velocity and characteristic turbulence of the air immediately above it.

The exact thickness will then depend on the properties of the solution, like concentration and solvent evaporation rate. The maximum thickness that can be produced from a given material/solvent combination depends indeed also on the maximum concentration at which the material can be dissolved in the solvent. Hence, for high soluble

materials thicker films can be obtained. Furthermore, the evaporation rate is dependent on solvent viscosity, vapour pressure, temperature and local humidity.

For the preparation of $BiVO_4$, Bi^{3+} ions were added to the solution in the form of $Bi(NO_3)_3{\cdot}5H_2O$, while V^{5+} in the form of $VO(acac)_2$ or $V(acac)_3$. W^{6+} was employed as $W(OC_2H_5)$ 5% w/v in etOH, when preparing the doped samples. All precursors were purchased by Sigma Aldrich, except for $W(OC_2H_5)$, which was provided by abcr.

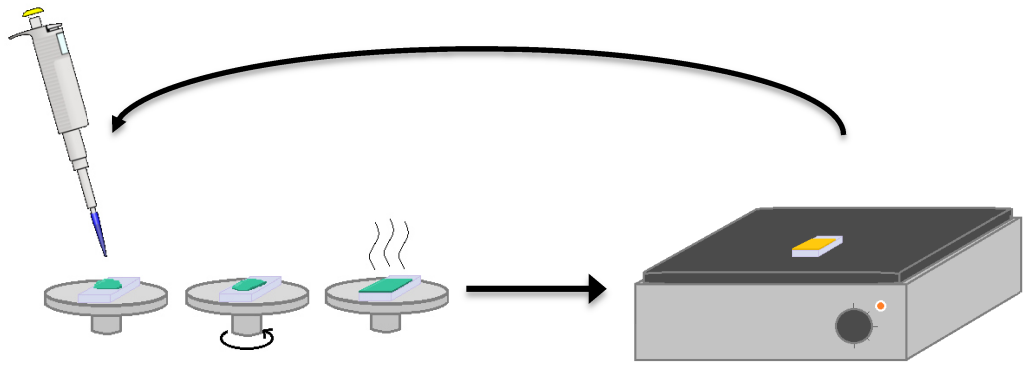

Figure 17: Representation of the synthesis of a thin film by means of a spin coater. The solution is first casted onto the substrate. The substrate rotation allows the solution to evenly spread while the solvent start to evaporate. Finally, the solvent complete evaporation results in the formation of a homogeneous film. The substrate is then placed on to a heating plate where the organic components of the solution decompose, leaving a film of the inorganic phase. Such cycle represent the deposition of one layer, which is repeated several times to increase the thickness of the film.

Many solvents and combinations of them were first used to dissolve the precursors, namely acetic acid, ethanol, DMF (dimethylformamide), actetylacetone, and a combination of all the above in different ratios. A more complete list of the solutions used to attempt the synthesis of homogeneous thin films is to be found in the results section (4.2.2).

The other parameters were kept constant as follows. The solution was drop-casted onto a clean 3x3 cm FTO support right at the beginning of the spinning step (dynamic dispense), which consisted of a single 10 seconds step at a rate of 1200 RPM. For the first layer 100 µl were casted onto the bare FTO, while for the successive layers 50 µl were enough to guarantee a total coverage of the sample with a thin layer of solution. In comparison to a static dispense method (dropping of solution before the start of the spinning step), dynamic dispense showed to be the best choice for a more homogeneous distribution of the solvent, especially for the first layer. During spin coating deposition, the FTO substrate was partially covered by a piece of tape, to avoid deposition on a small area, leaving a blank FTO which was needed to make electrical contact to the three electrode PEC cell when the sample was tested.

After the deposition of each layer, a drying step at room temperature of 10-15 minutes was necessary to avoid a too quick evaporation of the solvent from the film. Subsequently, after removal of the tape, the samples were moved onto a heating plate set at 450°C for 10 minutes. Several samples were prepared with increasing number of layers. Every 8 layers the samples were put into an oven to undergo an annealing step at 470°C for 8 h. Such temperature was chosen after an investigation that included TGA analysis (see results section 4.1) and an

annealing step study (see Appendix 8.2). The conclusion drawn by the annealing study was only based on thin samples and on photocatalytic activity, while structural analysis by SEM was not yet performed. This is the reason why only later on it was found that a second annealing step at higher temperatures, namely 600°C for 45 minutes, was needed. In fact, such extra annealing step was considered necessary only after findings obtained during the characterization of the samples. Therefore, more details are to be found in the results section. Furthermore, the 3x3cm substrate was split into two halves, in order to obtained two samples from each.

3.3. Characterization methods

3.3.1. TGA, UV-Visible spectroscopy, XRD, SEM

Thermo gravimetric analysis (TGA) where conducted on the precursors and on a mixture of them. In all cases the measurements were conducted placing 30-60 mg of the precursor in a Pt pan, cleaned by a blowtorch prior each measurement and performed under air flow. The decrease in weight percentage was monitored up to 600°C with a step of 5°C/min by a TGA Q50 V6.7 instrument.

UV-Visible absorption spectra were measured with a Carly 50 Conc UV-Vis Spectrophotometer. Prior each measurement, a clean FTO was put in the beam path and its spectra used as baseline. The absorbance spectra were collected for a range between 700 nm ad 350 nm. Above 700 nm no significance absorbance will take place, while the spectra profile near and below 350 nm will be quite noisy, due to the fact that samples are deposited on a 3 mm thick glass, coated with FTO, which interferes with the absorbance of the sample.

The absorption coefficients for each wavelength were extrapolated from the UV-Vis absorbance spectra using the equation

$$\alpha = \frac{abs}{l}$$

Where α is the absorption coefficient (m^{-1}), *abs* is the absorbance measured by UV-Vis spectroscopy and *l* is the film thickness measured for each sample from SEM images. The light penetration depth was then obtained by calculating the inverse of the absorption coefficient (as seen in equation 3.2).

Tauc plots were calculated from the absorbance spectra data, and band gaps (E_g) were extrapolated from such plots using the relation:

$$\alpha = \frac{A(hv - E_g)^m}{hv}$$

Where *A* is a constant, and m depends on the nature of the band gap. Specifically m=2 for direct band gaps, while m=1/2 for indirect ones.[4,11]

XRD patterns were collected with a D2 Phaser (Bruiker) diffractometer, which employed Co kα radiation (λ=190.26pm). Since the sample were synthetized as thin film on FTO coated glass approximately 5 mm thick, a custom made sample holder was employed, which ensure the position of the film to be at the right height respect

to the X-ray beam. The measurement were performed in the range between 12 and 65° 2Θ, with a 0.06° 2Θ increment per point and with an integration time per point of 3 seconds, to decrease the noise-to-signal ratio.

FIB-SEM was performed using a Nova nanolab 600. The acceleration voltage is 5 kV. The scale of each topograph is reported mentioned in each image.

3.3.2. Photoelectrochemical measurements

Photoelectrochemical measurement, also referred to as *JV* analysis (current density vs. applied potential) was the method employed in this research to test the photoactivity of the samples. During these experiments the sample, our working electrode, was connected to a Pt wire, which worked as the counter electrode(CE) and a Ag/AgCl reference electrode (RE). The choice of Pt as CE was based on the fact that, being a good catalyst, it would make sure the half reaction taking place at its surface would not be a limiting factor to the overall process.

Maintaining a constant pH during the measurements was also necessary, due to the fact that the potential at the WE measured with the Ag/AgCl RE is pH dependent, as evident from Eq. 5.1. This was guaranteed by using a phosphate buffer as the electrolyte in which the three electrodes were immersed. The pH was maintained at a value of 7 due to the fact that the WE, $BiVO_4$, is instable in alkaline environments.

The cell employed was made of Teflon and presented a small transparent area to allow the transmission of light from a lamp to the sample. The employed light source was a 75W Xenon arc lamp from the Optical Building Blocks Corporation. As already explained in the introduction, for standardizing PEC measurement, photocurrents are normally reported as current density, i.e. currents per area of illumination, and under an AM 1.5 simulated solar irradiation with 1 sun intensity, which corresponds to 100 mW cm^{-2}. To be able to calculate current density from the values of current measured, the illuminated area of the sample was measured and the estimated value was of 0.33 cm^2. On the other hand, in order to obtain a better simulation of the solar spectrum, UV and IR filters (which cut off wavelengths <420 nm and >100nm) were placed between the light source and the sample. Furthermore, the intensity of the light was measured with a THOR LABS PM100D Digital Optical Power and Energy Meter with a S120C sensor prior each experiment and tuned to reach the desired value of 100 mW cm^{-2} . Unfortunately, only toward the end of this project it was realised that the S120C sensor was selectively measuring only the intensity of a single wavelength, 355 nm, rather than the intensity of the overall spectra emitted by the lamp. This implies that the measurements performed and reported in this thesis cannot be compared to those from literature.

While the sample was illuminated by the lamp, a potential was applied scanning from -0.4 V to 1.4 V vs. Ag/AgCl and back. This will be denoted as one cycle. For ease of comparison with literature, where samples are tested in different electrolytes with different pH values, the *JV* curves reported in this thesis will show the applied potential horizontal axes both with the V vs. the Ag/AgCl values and a second horizontal axis with the converted values to the V vs. RHE. The equation used to calculate such values was:

$$V_{RHE} = V_{Ag/AgCl} + V^{\circ}{}_{Ag/AgCl} + 0.059 \times pH = V_{Ag/AgCl} + 0.6179\,V \tag{5.1}$$

Where $V^{\circ}_{Ag/AgCl}$ is equal to 0.199V in the case of the saturated KCl reference electrode used. The potential at which a photocurrent begins to be generated is referred to as onset potential, and it is therefore the minimum potential at which water splitting starts to occur. Further increasing of the applied bias gives rise to higher photocurrents. At higher potentials the semiconductor starts to act as a metal and a so called dark current also appears, contributing to the total current measured during the experiment. For this reason, a cycle is also always performed without illumination, which reveals the onset potential and the contribution of the dark current to the value measured while performing a cycle with the light on. The difference between the current produced while illuminating the sample minus the current produced in the dark is therefore the actual photocurrent produced by the sample. Furthermore, for experiments performed in the presence of light, the first few cycles always showed a high photocurrent that would decrease with the following cycles. This is due to the presence of unwanted surface species that will be gradually be removed by oxidation with each cycle. All the cycles obtained before reaching a stable point were therefore discarded.

An expedient to acquire more information about the sample's properties is by means of a light chopper. Using the same setup, a cycle is scanned while turning the light on and off at a constant rhythm. With this technique, small differences between photocurrent and dark current can be observed more easily, which is an advantage when trying to determine the onset potential. Furthermore, as soon as the light is switch on, transient currents can be observed (as anodic spikes), which are not detectable when performing a normal cycle with a constant illumination. The decrease in photocurrent is due to fast recombination of the photogenerated electrons with the accumulated holes. In the same way, transient cathodic currents can appear when the light is turned off. This happens when electrons recombine with the accumulated holes, forcing electrons form the external circuit back to the semiconductor.[4,11,48]

As already explained, these transient currents are caused by fast electron-hole recombination. This phenomenon can be due to many reasons. In particular, the slow kinetic for water oxidation is one of the main problems, being the factor that mainly limits photocurrent generation. A way to test if this is the case for the examined samples, is to compare the *JV* curve obtained using the usual electrolyte, to the photoperformance of the same sample in presence of a hole scavenger. A hole scavenger is a chemical species that has really fast interfacial hole-transfer kinetics. If the sample shows to have higher photocurrents in presence of a hole scavenger, than hole transfer at the interface with the electrolyte being water is definitely a limiting factor for the overall efficiency of the semiconductor, meaning that the photoelectrode is poorly catalytic for water oxidation. This was found to be the case for $BiVO_4$.[25,48,60] As described already in section 3.2.3, the photocurrent generated in the presence of a hole-scavenger can be used as an upper limit of photocurrents achievable for water oxidation with the help of an efficient OEC. The hole scavenger employed was Na_2SO_3 at a concentration of 0.1M.

Another interesting test performed was the comparison between performances of the electrodes between front and back illumination. Front illumination is referred to the light coming from the side of the semiconductor-electrolyte junction, while for experiment performed with back illumination, the light would first hit the glass/FTO/semiconductor junction. The photocurrent is expected to differ due to the penetration depth of light in the sample (see 3.2.1), which causes the generation of charge carriers in higher concentration on the side of the sample were light hits first.

The same setup used for photoelectrochemical measurements was employed for the photo-electrodeposition of a co-catalyst on the samples surface. The electrolyte was the same phosphate buffer with pH=7, but with the addition of 0.1 M $Co(NO_3)_2 \cdot 6H_2O$ (Sigma Aldrich). The deposition was assisted by light, and a larger area was illuminated compared to the measurements settings. This was done to ensure a deposition of the CoPi catalyst on a large area, and it was obtained by replacing the transparent component of the Teflon cell with a bigger one. The photo-assisted electro-deposition was carried out for 5 seconds at an applied voltage of 0,3 V vs. Ag/AgCl.

3.3.3. Transient Absorption Spectroscopy (TAS)

Figure 18 is a scheme of the EOS ultrafast transient spectrometer used for this project to conduct charge carrier dynamics investigation experiments. The probe is generated by a LEUKOS super continuum light source and it is a pulsed laser that covers the visible range between 300 and 900 nm. This is split into two beams (at BS1 in figure). One goes through the sample, before going into a detector (FO1), while the second one goes directly into a second detector (FO2) and will be used as the reference. Prior to the start of each experiment, the spectra profiles and intensities of the two beams (probe and reference) are adjusted to make sure they correspond to each other. This probe-reference detection scheme allows compensations for fluctuation of the probe and permits an optimization of the signal-to-noise ratio. The visible detector is composed of two fibre optics (FO1 and FO2) coupled to a multichannel spectrometer with CMOS sensor with 1.5 nm intrinsic resolution, a sensitivity range of 350-900 nm and a maximum spectral acquisition rate of 2000 spectra/s.

A second laser, the pump (green line in Figure 18), is generated by an Nd:YAG crystal which emits a beam of 1064 nm. The pulse was set at 1ns width and 1kHz repetition rate. The system allows the generation of harmonics from this beam into separate beams of 532 nm, 355 nm and 266 nm. The wavelength used as pump for all the experiment reported is the 355 nm.

Both pump and probe beams have a spot diameter of <1mm and prior to each measurement the overlap of these two beams must be verified. The time range that can be investigated with this setup is in the order of ns up to 100 μs and it is dependent on the laser properties mentioned above. The frequency of the laser will determine the upper limit of the time window that can be investigated, while the bottom limit, the resolution of the spectrometer, is dependent on the laser pulse width.[61] The average power intensity of the pump was regulated through a neutral density filter (ND1 in Figure 18), ranging from 0.50 mW to 2.0 mW, and measured with a THOR LABS PM100D Digital Optical Power and Energy Meter with a S120C sensor. This range of power intensity corresponds to a range of excitation energy of 500-2000 nJ, which corresponds to 10-40 Sun.

During experiments in air, the sample was simply placed in the holder, except for O_2- and Ar-rich measurements, where it was placed in a sealed glass cuvette, in which the specific gas was injected, prior the measurement. The same cuvette was employed for the experiments conducted in an electrolyte. In all cases, the sample was held in a perpendicular position respect to the probe beam direction. When a voltage needed to be applied, the sample was connected to an AUTOLAB cell in a three electrode system, where a Pt wire was used as CE and a Ag/AgCl as a reference electrode (RE). The electrolyte employed was a phosphate buffer (pH=7) and when experiments with a hole scavenger were required, 0.1M Na_2SO_3 was added to the buffer solution.

A general rule that was followed during all experiments was randomizing the collection of data. For example, the increase in excitation energy was carried on in a random order and not increasingly from 0.5 mW to 2.0 mW. Furthermore, the first test of each set was repeated at the end of the series, to prove the reproducibility of the experiment. The same expedient was applied to all types of experiments.

The software used for the collection of $\Delta A(\lambda,s)$ controls the delay time between pump and probe and collects spectra at each selected delay time in an automated way. The selection of delay time occurs in a random order from 0 to 100 us, and the software collects the data according to an algorithm which ensures more spectra will be collected at the beginning of the decay. All spectra collected at the same delay time are then averaged. Such expedient is meant to allow the acquisition of a better resolved decay function, with less signal-to-noise ratio, at the beginning of the decay. This should guarantee a more meaningful fitting of the data. For the same reason, since the ΔA signal is expected to decay to zero after a certain time, less data will be collected in the range of more distant delay times. The longer the total collection time, the lower the signal-to-noise ratio. However it is better to not expose the sample for prolonged times to the laser beam, in order to prevent material damaging. Therefore, for all experiment conducted, the total time was kept fixed to 20 minutes, which allowed to obtain a clear enough signal, without exposing the sample for too long to the laser. For the same reason, the sample was slightly moved after each measurement to allow the laser to focus on a different spot.

Surface Explorer software was then used to analyse the data. With such software it is possible to select both absorption spectra at a desired delay time and decay profiles at a chosen wavelength. For all the data reported in the results, the absorption spectra are selected at the delay time at which absorption was at its maximum, while the decays are selected at the maximum absorption wavelength. To better interpret the differences in lifetimes between different decays profiles, the data were normalized to their maximum.

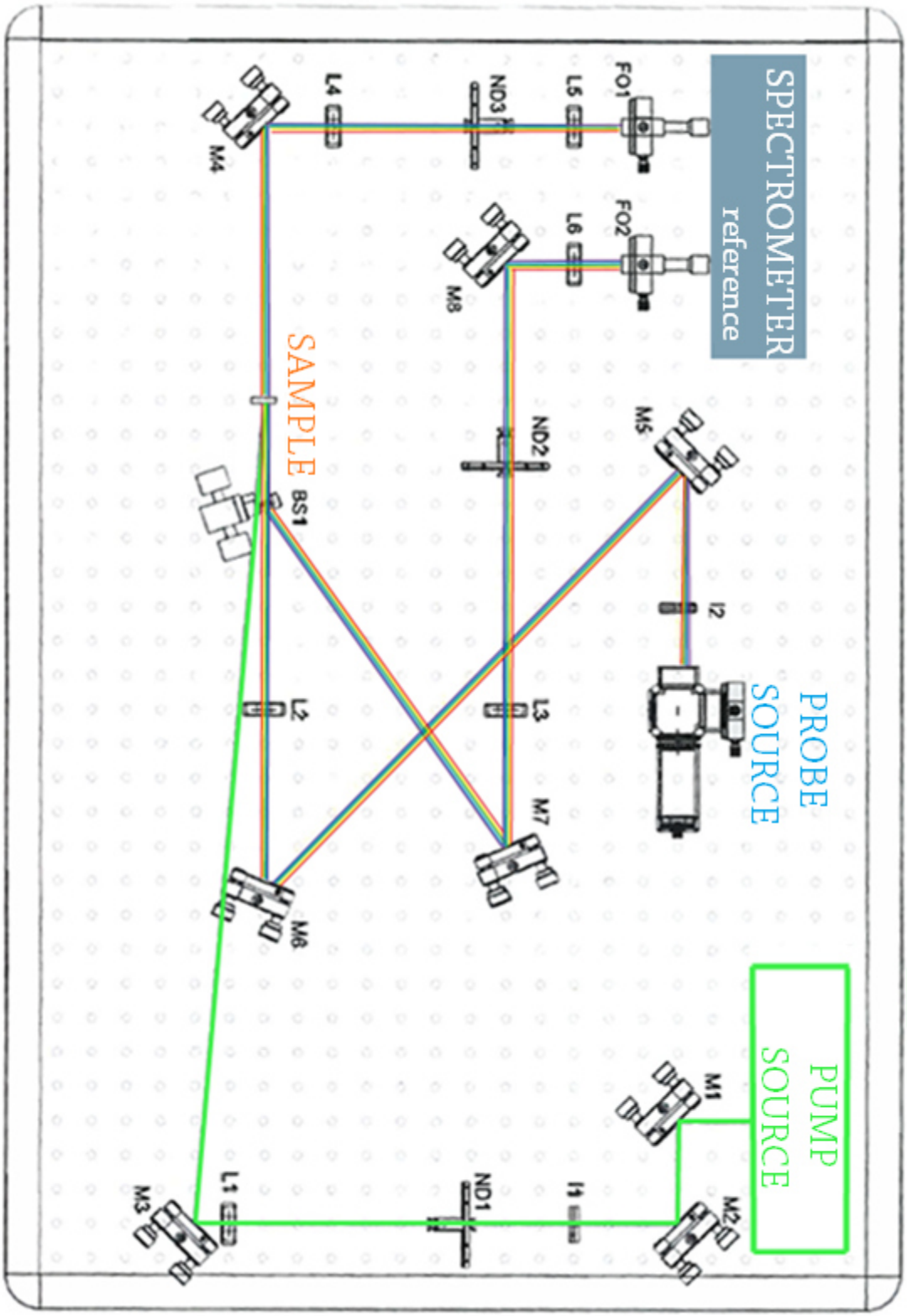

Figure 18: Transient Absorption Spectrometer scheme. A description of its functioning is to be found in the chapter. M = mirrors, L = lenses, ND = neutral density filters, BS = beam splitters, FO = fibre optics.

4. Results

4.1. TGA on precursors

Literature reports both heating plate during deposition step and oven temperatures during annealing phase between 400°C and 500°C when using MOD combined to spin coating or spray pyrolysis to synthetize $BiVO_4$ thin films samples.[22,24,62–65] We also know that the change of crystalline phase of $BIVO_4$ to the monoclinic phase occurs around 400°C. Nonetheless, thermogravimetry analysis (Figure 19) was conducted on the chemicals used to prepare the precursors solutions. Such analysis aim was to investigate their decomposition steps in the range of temperatures that will be employed during the synthesis procedures.

Figure 19b shows the derivative weight percentage as a function of the temperature for the mixture of the two precursors. The initial weight loss which occurs between 100°C and 200°C is due to water removal. In the 200-300°C range the weight loss is attributed to pyrolysis of metallo-chelate ligands, i.e. their oxidation to a gas, volatile phase. Above 300°C the weight loss is very minimal and probably due to residual organic materials decomposition and further crystallization. The weight remains constant after 530°C indicating that the decomposition of all organic materials is completed. From these results, we could assume that temperatures of 530°C seem to allow complete decomposition of the organic residual of the precursors, leaving only the species needed to form the wanted $BiVO_4$. However, such analysis does not take into account the solvent the precursors are dissolved in, which has its own decomposition temperatures. Therefore, a more significant analysis should be performed on the precursors solution dried to a gel state.

Furthermore, the heating plates used both during spray pyrolysis and spincoating synthesis could only reach 500°C and in both cases problems where encountered when such temperatures were used. In the case of spray pyrolysis, the small and close environment of the setup was cause of a local increase in temperature which was not ideal, especially for the ultrasonic nozzle. Therefore at such temperatures, only few cycles could be sprayed before being forced to turn off the heating plate. On the other hand, during the first attempt of spincoating, when the FTO with a newly deposited layer was put on the plate, the top layer of the heating plate fractured, At 450°C the heating plate seemed to sustain the heat. For this reason higher temperatures were not employed during this step. Furthermore, as obtained from the TGA analysis, most of the weight loss has already occurred at this temperature, therefore 450°C was considered as appropriate temperature for this phase of the synthesis. However, a final annealing step is also necessary to guarantee the formation of the monoclinic phase of $BiVO_4$ and the complete removal of the organic phase. At this stage an oven is used and higher temperatures can be reached with fewer problems. It is anyway necessary to note that $BiVO_4$ is deposited on FTO coated glass, which is a material that melts around 550-600°C, therefore higher temperatures than those should be avoided.

Because of the results obtained by TGA analysis, 530°C was the temperature of choice for the first synthetized samples. However, the films that appeared homogeneous before such annealing step, presented large scattered areas at the edges once removed from the oven. It was therefore decided to investigate the effect on photoperformance of a range of temperatures between 470°C and 530 °C for the annealing step (see Appendix 8.3). The conclusion of this investigation was that annealing the samples at 470°C resulted in the best appearance of the film, while the photoperformance was not conclusively affected. Therefore, all samples were then synthetized using this temperature. As it will be evident from the following results sections, this temperature didn't indeed allow total removal of carbon. It was therefore decided to add an extra annealing phase at 600°C for 45 minutes. The consequent results of this choice are discussed in section 4.3.4.

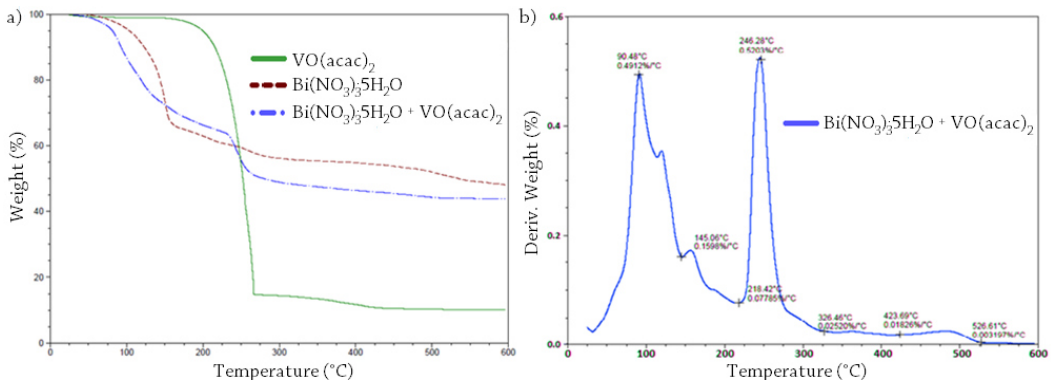

Figure 19: a) TGA Weight percentage as a function of the temperature of the precursors and of the mixture of both. b) Derivative weight percentage as a function of the temperature for the mixture of the two precursors used to synthetize the $BiVO_4$ samples.

4.2. Synthesis procedures

4.2.1. Spray pyrolysis

As mentioned in the methods section, different parameters can be tuned when employing a spray pyrolysis setup. Table 1 is a summary of all the procedures used to attempt the synthesis of homogeneous thin films of $BiVO_4$. Unfortunately, none of the attempted methods was successful. The difficulties encountered were due to the fact that the machine was not purchased, but built from zero at the university and was completed only toward the end of the research. Once arrived, several adjustments were continuously required to improve the performance of the machine. In particular, the direction of the flow was hard to control. The heating plate positioned at the bottom of the glass box containing the main part of the setup created a gradient of temperatures which diverted the flow away from the FTO support. Furthermore, following procedures from literature was not trivial both for the uniqueness of our setup and because the only mentioned parameters usually reported in literature were precursors, solvents and concentrations, while as explained in the methods, the most important ones are solution flow rate and atomizer settings, which were left out from the reports.

The best results achieved were with DMF as solvent. More specifically, the Bi precursor was previously dissolved in acetylacetone before being diluted with DMF. Such solution was then added to the DMF solution of

$VO(acac)_2$. The solution flow rate was kept high (4-6 ml/min), which guaranteed the deposition of most of the solution on the FTO support and lower temperatures (250-300°C) were found to be better than higher ones. With this combination of parameters, the FTO resulted homogeneously covered, unlike all the previous attempts. Unfortunately, a very thin powder of $BiVO_4$ seemed to be deposited rather than a film, which means that the droplet underwent the variations labelled as (D) in the methods section (3.2.1) . Such powder was found to be crystalline by XRD analysis (Figure 20) and photoactive when tested in a PEC cell (Figure 21). Nevertheless, the photoactivity was very low, and an electrode synthetize as a powder with very low sticking force to the substrate and among the particles, which made the so-obtained material a bad candidate for employment as a photoelectrode.

Table 1: Summary of settings used to synthetize $BiVO_4$ by means of spray pyrolysis. Bi indicates the $Bi(NO_3)\cdot 5H_2O$ precursor and V stands for $VO(acac)_2$. When it's indicated that one precursor was pre-dissolved in a different solvent than the one used in excess, the amount of solvent was 1 ml out of a 100 ml of the final solution. The carrier gas flow rate was kept between 3.5 and 6 lpm, the nozzle scan rate was 15 mm/s and the waiting time between each cycle was of 30s.

Solvents	Concentration /[mM]	Solution Flow Rate /[ml*min^{-1}]	Carrier Gas	Heating Plate Temperature	N° of Cycles	Ultrasound power / [W]
DMF (Bi pre-dissolved in acac)	25	2	air	350	25	
	25	2	air	460	10; 20; 30; 40	
	12. 5	2	air	460	30; 40	
	6.25	2	air	490	30;40	
absolute etOH (Bi pre-dissolved in acac)	5	2	air	490	30; 60	
DMF	10	2	air	460	30; 60	6; 2,3
	5	5	air	250	20; 40	6; 2,3
absolute etOH (V pre-dissolved in DMF and Bi in acac)	10	2	air; N_2	260 (+4h at 480 in oven)	20; 40	6; 2.3
absolute etOH (Bi pre-dissolved in acetic acid)	5	2; 2.5; 3; 3.5	air	260 (+4h at 480 in oven)	30; 60	6; 2.3
DMF (Bi pre-dissolved in acetic acid)	10	2; 3; 5	air	350; 430	40; 60	1,65; 2,3
		3	N_2	350; 430	20;40;60	2,3
only Bi(pre-dissolved in acetic acid) +DMF in excess	10	3	air	350; 460	30	2,3
only V in DMF	10	3	air	350; 460	30	2,3
only Bi(pre-dissolved in acac) + DMF in excess	5	3	air	395	20	2,3
only V(pre-dissolved in acac) + DMF in excess	5	3	air	395	20	2,3
DMF (Bi pre-dissolved in acac)	**5**; 2.5	3; **4**; 5; 6	**air**	250; 290; **350 (+3h 470 in oven)**430; 470	20; 40; 50; **60**	**2,3**

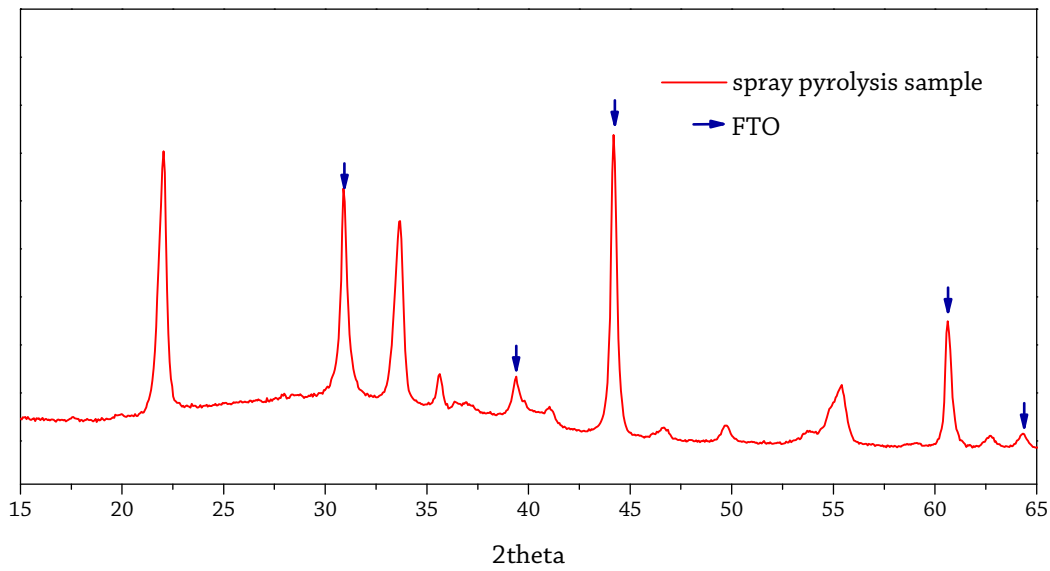

Figure 20: XRD of the powder deposited on FTO by spray pyrolysis. The sample is crystalline, but some of the peaks of the monoclinic phase have very low intensity.

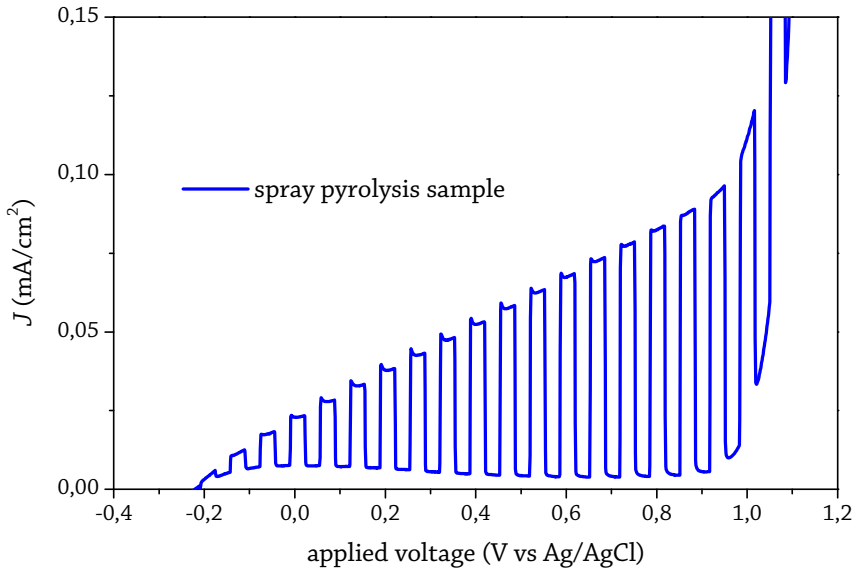

Figure 21: Photocurrent density produced by the sample synthetized with the green highlighted settings in Table 1. This sample consisted of a powder deposited on FTO, rather than a thin film.

4.2.2. Spin coating

As anticipated in the methods section (3.2.2) several combination of precursors solution were prepared and deposited on FTO by spin coating. A summary is reported in Table 2.

Table 2: Summary of the solutions prepared and deposited on FTO for the synthesis of $BIVO_4$. The combination that resulted in the most homogeneous and photoactive film is the one in bold blue.

Bi		V	
Concentration [M]	**Solvent**	**Concentration [M]**	**Solvent**
0.2	Acetic acid	0.03	Acetyl acetone
0.2	Acetic acid	0.03	etOH
0.2	Acetic acid : Acetyl acetone =1 : 8	0.03	Acetic acid : Acetyl acetone =1 : 8
0.2	Acetic acid : Acetyl acetone =1 : 8	0.7	Acetic acid : Acetyl acetone =1 : 8
0.2	Acetic acid : Acetyl acetone =1 : 8	0.03	Acetyl acetone
0.2	DMF	0.1	DMF
0.2	EtOH	0.03	Acetyl acetone
0.2	DMF	0.03	Acetyl acetone
0.2	Acetyl acetone	0.03	DMF
0.2	**Acetyl acetone**	**0.03**	**Acetyl acetone**

Some of these solutions resulted in very inhomogeneous film, which was due to a too fast evaporation of the solvent. Other led to very scattered film, with very low photoactivity due to very low light absorption. Other solvents and concentrations were also tried, but the V precursor was not easily dissolved in many of them. As a conclusion of such investigation, the solution that showed to guarantee the formation of an homogeneous and not scattered thin film (Figure 22) was a 30 mM in acetyl acetone, with $Bi(NO_3)_3{\cdot}5H_2O$ and $VO(acac)_2$ in a 1:1 ratio (highlighted in green in Table 2). Furthermore, to allow better dissolution of the precursors both Bi and V solutions were sonicated for 30 minutes and so it was for the final solution.

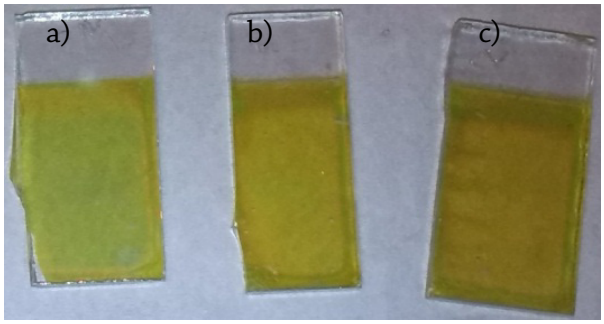

Figure 22: Picture of $BiVO_4$ thin film electrodes deposited on FTO-coated glass. The top section was covered by a piece of tape during spin coating deposition of the precursors solution. In this way, a portion of FTO was left exposed in order to allow connection to the circuit. The three samples have increased thickness a) 16-layers, b) 20-layers, c) 23-layers.

4.3. Structural characterization and photocatalytic analysis

Since, unlike spray pyrolysis, the synthesis by means of a spin coater was successful and allowed the preparation of homogeneous photoactive samples in a reproducible way, the following results all present investigations conducted on spin coated samples.

4.3.1. Thickness investigation

We discussed how the capacity of a semiconductor to absorb light influences its photo-performance, since an increase in absorption corresponds to a higher amount of photo-generated charges. To obtain such improvement in absorption, one can increase the thickness of the film. However, it is also known that the photo-performance will improve until a certain thickness and then decrease again for too thick samples, as previously explained. Therefore, every semiconductor has its optimal thickness that depends on its specific properties.

Several samples were prepared by spincoating as described in the methods, with an increasing number of layers, namely 8, 12, 16 , 20 and 23. Figure 24 shows the UV-Vis absorption spectra for each sample. All spectra had the same shape, with most of the absorbed light being in the range of 350-450 nm. As expected, for thicker samples the absorption was more intense. However, all samples thicker than 8 layers, showed a negative absorption in the range of 500-700nm. All measurements were conducted with the spectra of the FTO support as baseline. Therefore, this apparent negative absorption could be due to the addition of a new interface (FTO-$BiVO_4$), which is not present while collecting the baseline spectra. When light goes through the interface of two media with different refractive indices, transmission and reflection occur, on an extent that depends on the two materials characteristics. Hence, the presence of a new interface respect to the baseline might be the reason of this negative feature. As a further confirmation of the role that the new interface plays in this effect, the samples that show a negative absorption in their spectra, are those that show mirror-like features at the $BiVO_4$-FTO interface at the naked eye.

Multiple samples were synthetized for each thickness, and it was found that UV-Vis spectra for different samples with an equal number of layers had the same absorption intensity. This information was used to assume that all samples with the same number of layers could be expected to have same thickness.

Tauc plots were also calculated (see Appendix 8.1). The band gap values estimated are higher than expected (ca. 2.65 eV instead of 2.4-2.5 eV). However, the same values were in few cases reported in literature for direct band gaps.[23,45] Yet, the interference that resulted in an apparent negative absorption might add an error to the calculations and therefore be the reason of the mismatch with literature. The calculated values are reported in Table 3.

Table 3: Calculated band gaps values and average thickness estimated from FIB-SEM cross-sections of each samples.

Number of layers	Direct band gap (eV)	Average thickness (nm)
8	2.65	-
12	2.68	54.4 ± 9.3
16	2.65	63.6 ± 9.2
20	2.65	92.5
23	2.65	111.6 ± 2.3

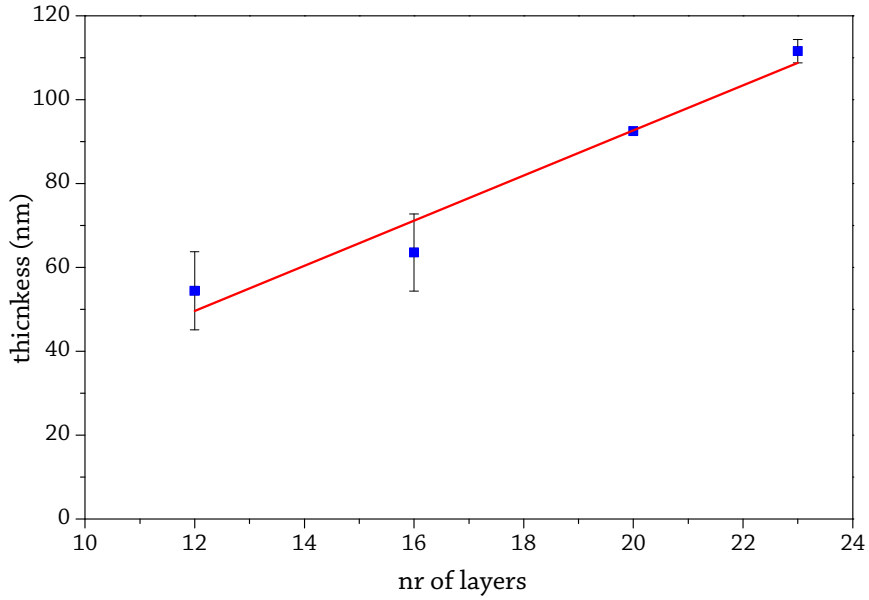

Figure 23: Plot of the correlation between thickness and number of deposited layers. The slope indicates that for thicker samples, each deposited layer would increase the thickness of approximately 5 nm. The error on each data is the deviation standard on the calculated average thickness.

FIB-SEM cross-sections were used to evaluate the thickness of each sample and the morphology of their surface. The images also revealed that the layer right beneath the $BiVO_4$ film, the conductive FTO, was not flat. On the contrary, its surface presented crystals of different dimensions resulting in a quite rough interface between FTO and $BiVO_4$. This can be easily seen in the cross-section FIB-SEM images reported in Figure 26 (while a front image of bare FTO is to be found in Appendix 8.2). Therefore, due to the FTO rough features, the calculation of the thickness of $BiVO_4$ films was not trivial, especially for the thinnest samples. In Table 3 the average thickness values calculated from the cross section images are reported. If we exclude the thinnest samples, a linear correlation is expected between number of layers deposited and thickness. The slope of the fitted curve suggested that for each deposited layer the thickness increases of approximately 5 nm. This cannot be applied for the first layers due to the roughness of the FTO surface. The fitting line has indeed a negative intercept with the X axis, which confirms that such linear fit cannot be applied to the thinnest samples. To be noted, the thickness was not calculated on multiple samples, but by measuring the thickness on different points of each samples. Therefore, these linear fit is not meant to be of indication of thickness reproducibility, but as average distance between FTO and surface for each sample.

FIB-SEM front images also show a good coverage of the entire substrate surface and the enlargement in particle size that follows the increase of thickness (Figure 28). However, the images show darker areas distributed non-homogeneously over the surface of the samples. This might be due to residual carbon. Such surface contamination is expected to strongly affect the performance of the photoelectrodes. Therefore, an extra annealing step was carried out in order to remove the excess of carbon. This issue will be discussed more in detail in section 4.3.4.

From the UV-Vis absorption spectra, the penetration depth of each wavelength was calculated. The results are shown in Figure 25. Most of the light absorbed from $BiVO_4$ is between 350 nm and 450nm, as shown in the

absorption spectra. For this range of wavelengths, the penetration depth was calculated to be between 60 and 120 nm, which is in the scale of the samples thickness.

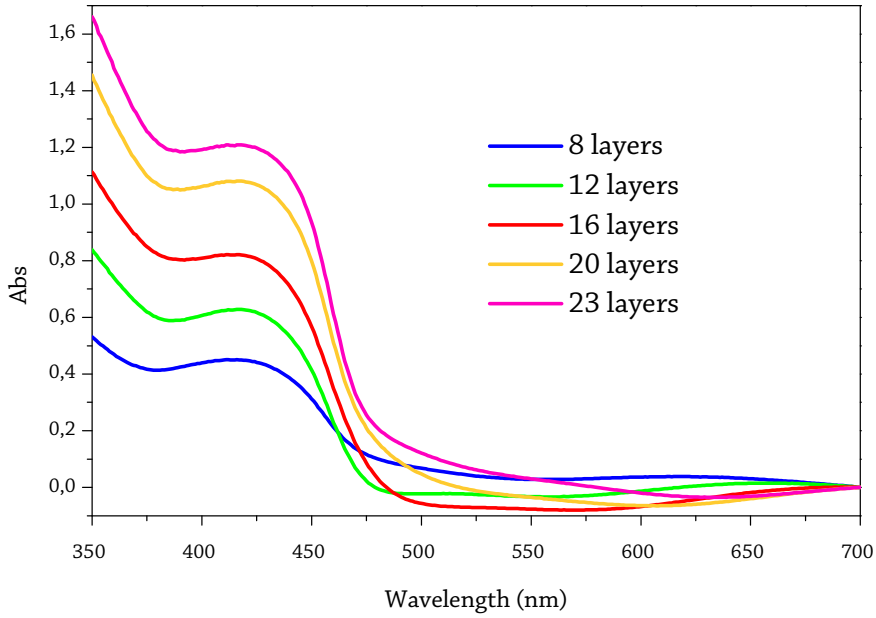

Figure 24: UV-Vis absorption spectra of $BiVO_4$ thin films for different number of layers deposited. The maximum absorption is found at 430 nm ca. The increase in absorption near 350 nm is due to interference caused by the glass support.

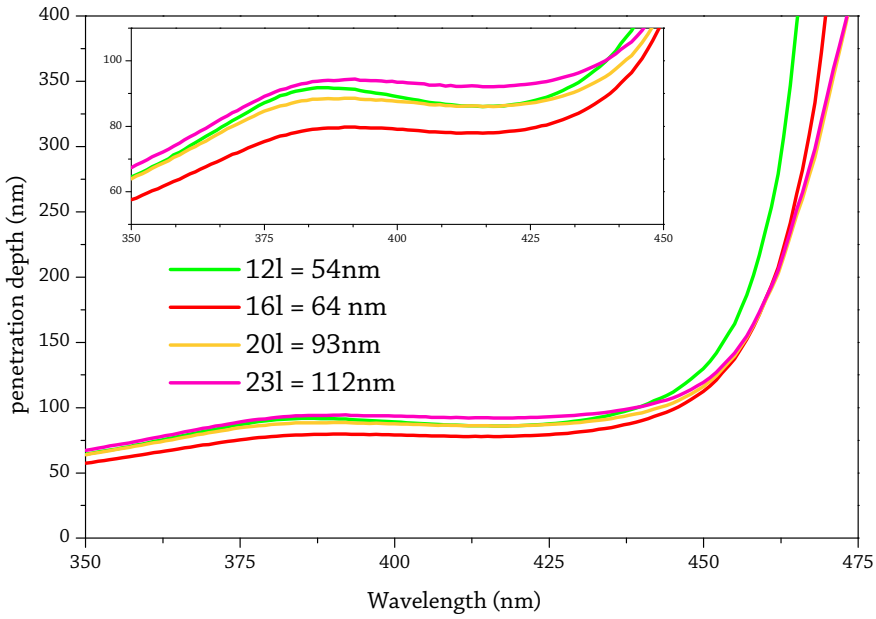

Figure 25: Calculated penetration depths for $BiVO_4$ different samples. The inset shows a zoom-in of the plot between 350nm and 45 nm, underlying the penetration depth to be between 60 and 120 nm for such range of wavelengths.

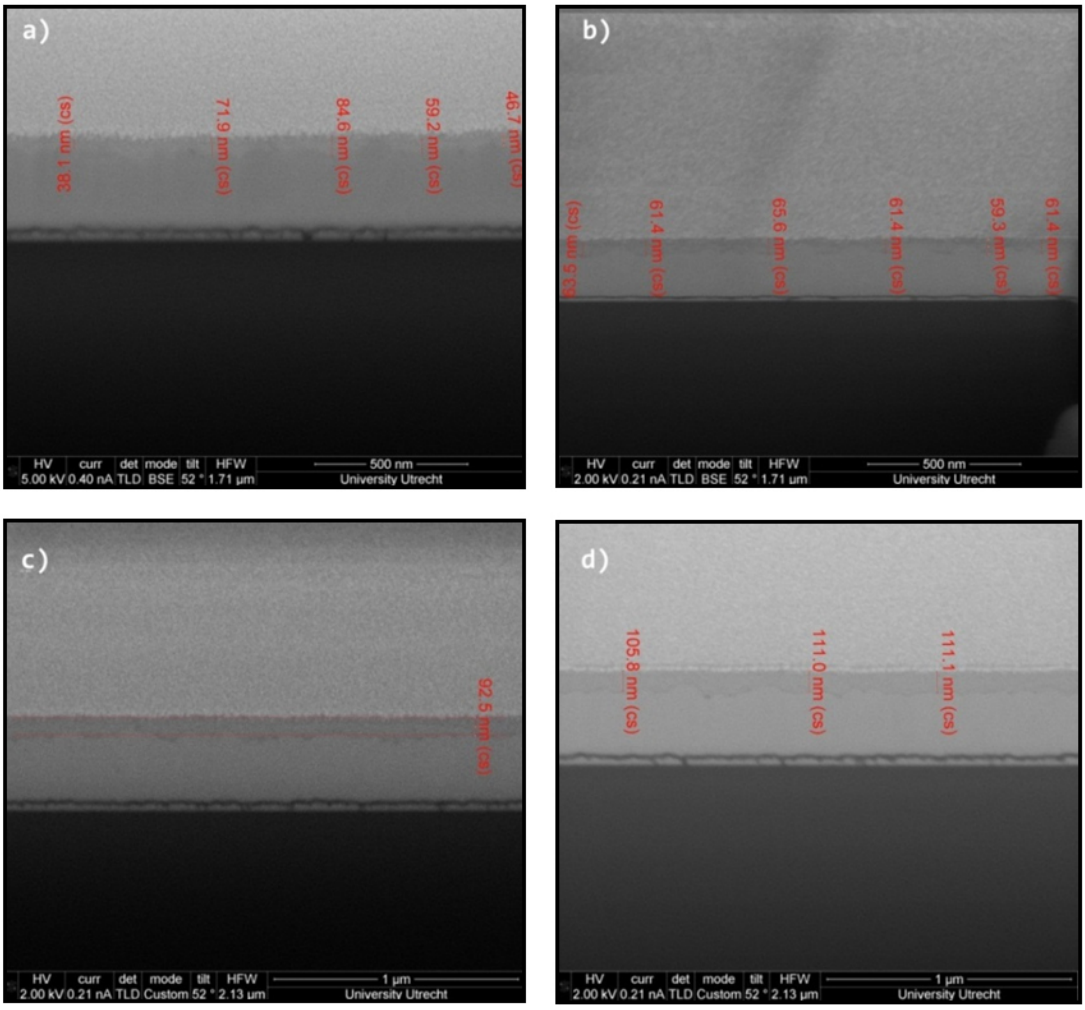

Figure 26: FIB-SEM cross images of the samples prepared with increasing number of layers. a) 12-layers; b) 16-layers; c) 20-layers and d) 23-layers sample. For the thinnest sample it was not possible to take a cross section image.

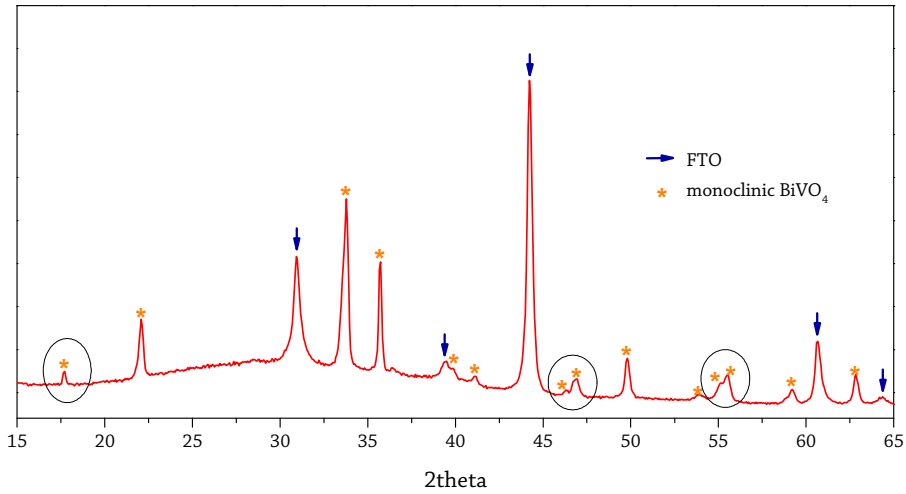

Figure 27: XRD of bare $BiVO_4$. The yellow marks indicate $BiVO_4$, while the blue arrows correspond to the peaks generated by crystalline FTO. The peaks marked by a circle are those that confirm the presence of monoclinic phase.

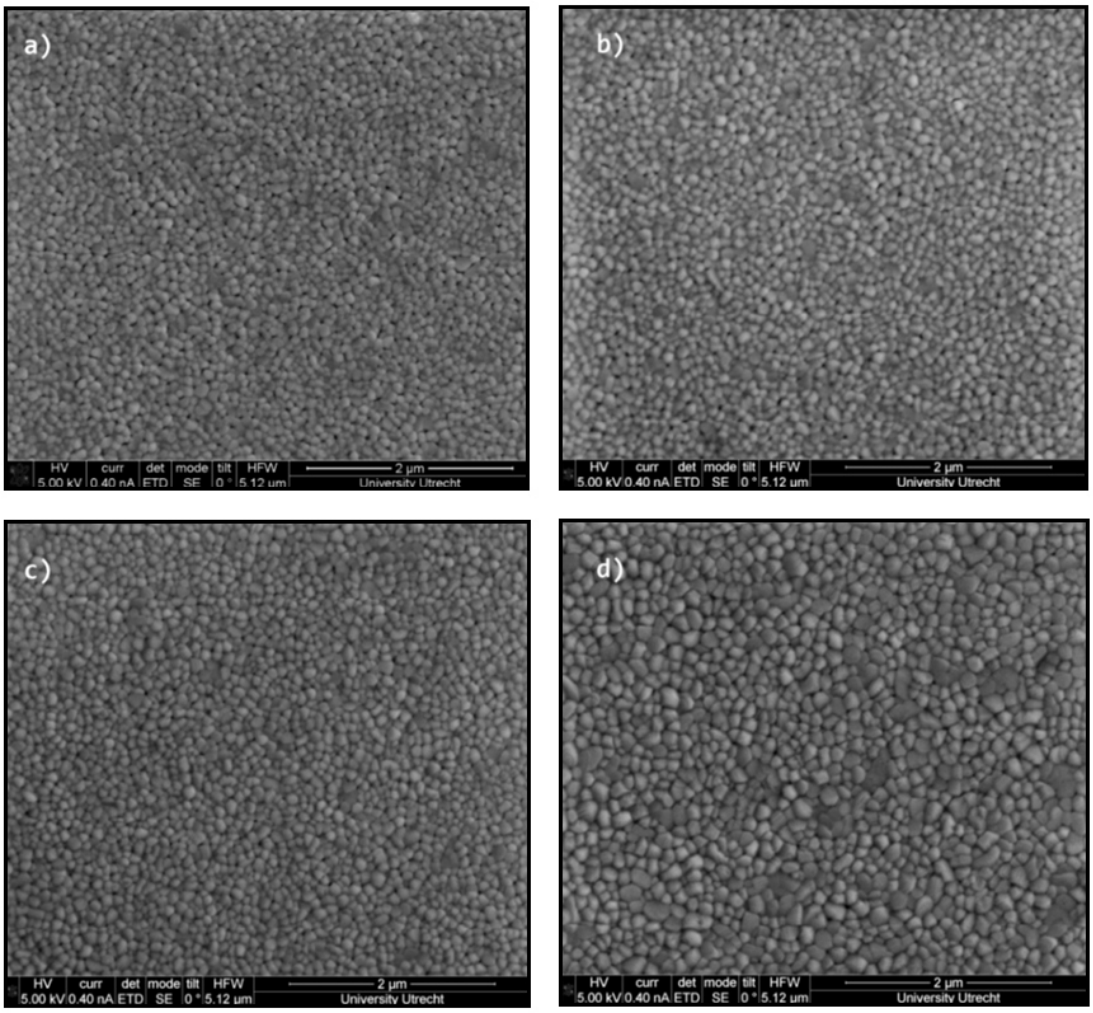

Figure 28: FIB-SEM surface images of different samples. a) 12-layers, b) 16-layers, c) 20-layers and d) 23-layers sample. The particle size increases with the thickness of the sample.

The XRD pattern for a representative sample is shown in Figure 27. According to literature, the presence of monoclinic $BiVO_4$ can be judged by the existence of a peak at 17.5° and splitting of peaks at 22°, 46.5°, and 55° of 2θ.[34,39]

Being a thin film deposited on a crystalline substrate, the XRD patterns will differ from those of a pure crystalline powder of the same material. The most intense peaks are indeed assigned to the crystalline F-SnO_2 (FTO), which lies beneath the $BiVO_4$ layer. Nonetheless, most of the significant $BiVO_4$ peaks are present and we can see the presence of a peak at 15° 2θ, and the splitting of peaks at 46.5° and 55° 2θ, while the splitting at 22.5° is not detectable. Nonetheless, we can assume our samples to be mostly in the desired monoclinic phase.

The photoactivity of the samples was then tested as explained in the methods. All samples showed photoactivity and, as expected, the increase in thickness enhanced the photocurrent produced (Figure 29a). When comparing the photocurrents between front and back illumination, differences were not seen for thin samples, while more significant variation were shown in thicker samples, as a consequence of the penetration depth of light becoming shorter than the sample thickness (see Figure 29b). However, the results showed to be opposite to those reported in literature.[22,43–45,66] That is to say, front illumination proved to induce a better photo-performance than back

illumination. This discrepancy with literature was attributed to the presence of high quantities of residual carbon on the surface of the samples (and possibly in the bulk too), as detected by FIB-SEM analysis.

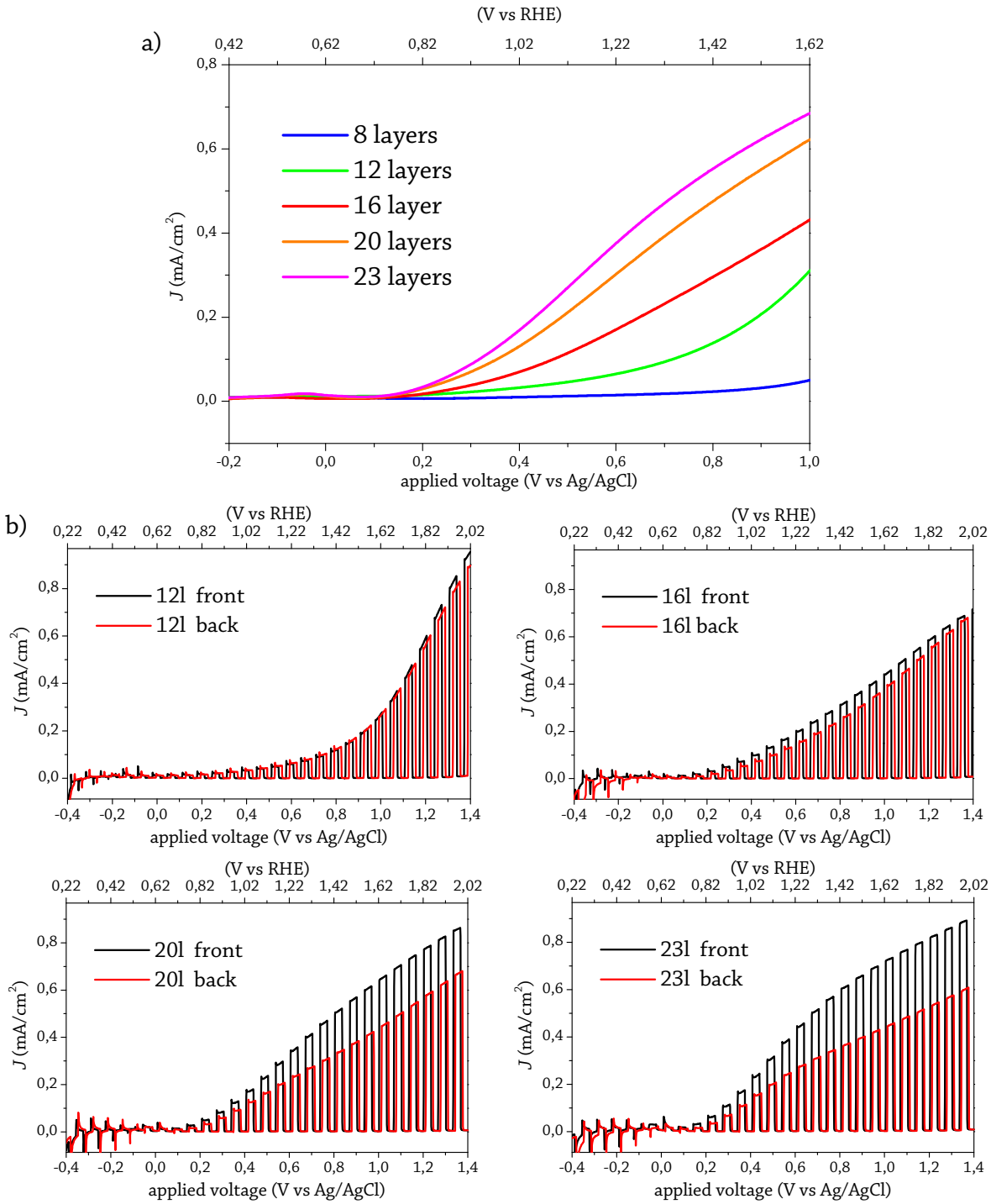

Figure 29: Photoelectrochemical performance of $BiVO_4$ in a phosphate buffer solution at pH=7. a) Comparison of electrodes with increasing thickness. The difference in current with the dark confirms that all the samples are photoactive and that the thicker the sample, the higher the current produced. b) Comparison between photoelectrochemical performance between front and back illumination for a set of thicknesses. For 8-layers (not in figure) and 12-layers samples no difference is shown, while front illumination resulted in a better performance for the 16-layers, 20-layers and 23-layers samples. The cycles were performed with a chopped light.

It is known that a major problem in $BiVO_4$ photoanodes is the slow kinetic of surface transfer to the electrolyte. To verify if this was the case for our samples, we tested their photoperformance in the usual electrolyte, but with the addition of a hole scavenger, namely 0.1M Na_2SO_3. The SO_3^{2-} anions have faster oxidation kinetics than water, and if such species are present, we can assume that all the holes that reach the surface will be injected into the electrolyte and oxidise the SO_3^{2-} into SO_4^{2-}. Since the extraction of holes will prevent them to recombine with the photogenerated electrons, therefore permitting the flow of charges in the circuit, this will result into higher photocurrents. Hence, the extent of current density enhancement measured by the addition of a hole scavenger into the electrolyte is a measure of how slow surface kinetics for water oxidations are. Such effect is shown in Figure 30 for a sample with 12 layers in thickness. The photocurrent density was drastically improved and the same was proved for all samples, with more pronounced effects for thinner samples compared to the thickest ones. These experiments were performed with chopped light and we could see the presence of transient spikes for the sample tested in the buffered solution (red line in Figure 30). Such spikes are an indication of fast recombination of charge carriers and they are no longer present once the sample was tested with a hole scavenger added to the electrolyte (blue line in Figure 30). This is a further confirmation that slow surface kinetics is a big issue for the synthetized samples.

This suggests that the deposition of a co-catalyst on any of the samples prepared should then also result in a similar improvement. To be noted is that, as for the performance in absence of a hole scavenger, also with the addition of Na_2SO_3, the thicker samples showed to produce higher photocurrents when illuminated from the front compared to photocurrents obtained by back illumination. This suggests that even when drastically improving surface kinetics, the presence of carbon still affected the performance of our samples.

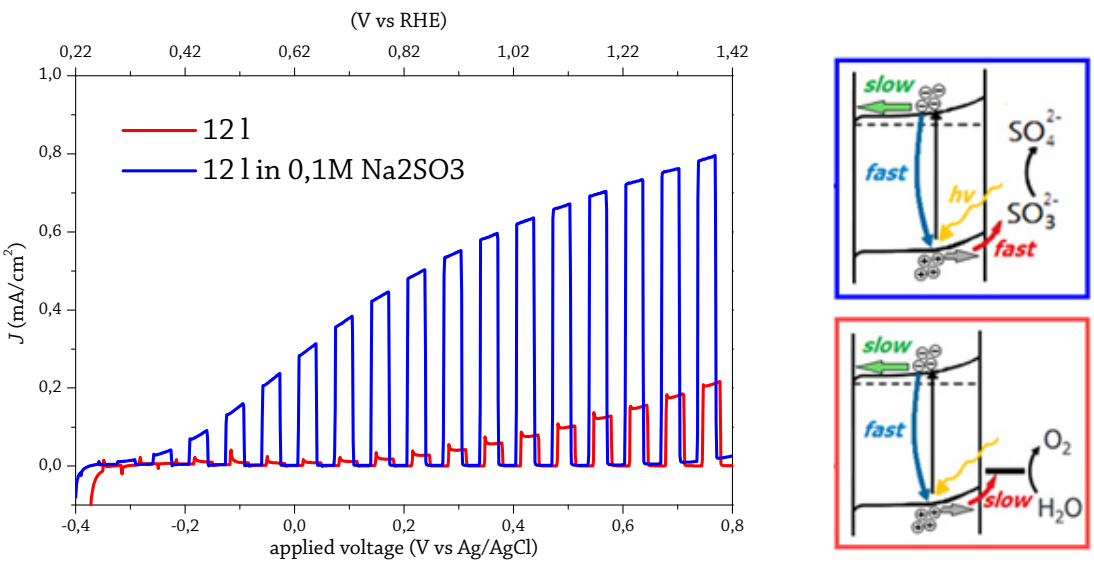

Figure 30: Photoelectrochemical performance with chopped light of a 12-layer $BiVO_4$ electrode in a phosphate buffer solution at pH = 7 (red line) and with the addition of a hole scavenger (blue line). On the right side, a graphic representation of semiconductor-electrolyte junctions in the two cases of water and hole scavenger as available species in the electrolyte to accept the photogenerated holes. The image stresses the difference in surface kinetics between the two cases.

4.3.2. "CoPi" photo-assisted electrodeposition

As we saw in Figure 30, once a hole scavenger was introduced to the electrolyte, the photoperformance of $BiVO_4$ significantly improved. This suggested that the main problem with our samples was due to slow surface kinetics. To address this problem an oxygen evolution co-catalyst (OEC) was employed. The OEC of choice was a CoPi, which was photo-electrodeposited as explained in the methods, on different samples. The efficacy of the deposition was tested by comparing the performance of the bare sample in presence of a hole scavenger with the performance of the same sample after deposition of the CoPi catalyst in an electrolyte not containing Na_2SO_3. In all cases the photoperformance obtained by addition of a co-catalyst proved to enhance the photocurrent almost to the level reached by the presence of Na_2SO_3, denoting that the deposition was in all cases successful. The results for the 8-, 12- and 16-layers samples are reported in Figure 31 and similar outcomes were found for all samples.

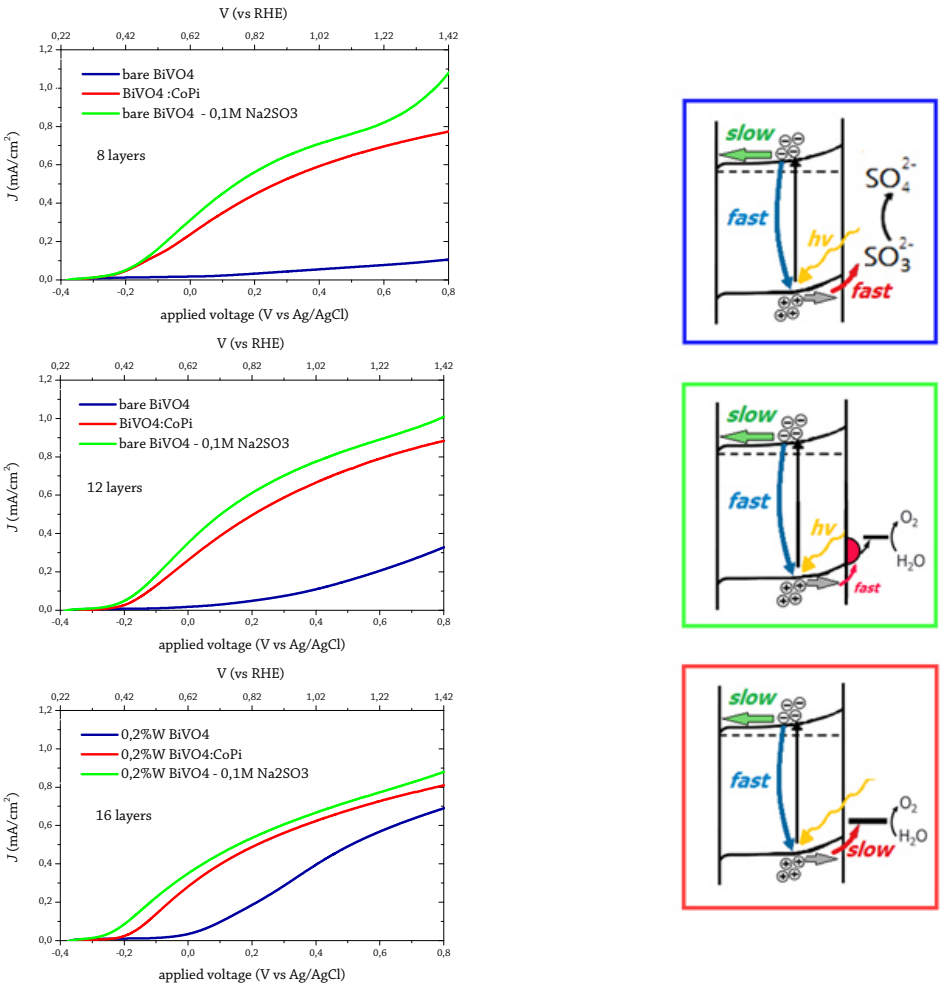

Figure 31: The three *JV* graphs on the left side represent the photoperformance comparison between a $BiVO_4$ sample tested in a phosphate buffer (red line), the same sample tested in presence of a hole scavenger (blue line), and the same sample after photoelectrodeposition of CoPi (green line). a) 8-layers, b) 12-layers and c) 16-layers samples. On the right side, a graphic representation of semiconductor-electrolyte junctions in the three cases of bare electrode placed in water (red square), same electrode in presence of a hole scavenger (blue square) and electrode with a deposited OEC on its surface, placed in water (green square). The images stress the difference in surface kinetics among the three cases.

CoPi was also deposited on bare FTO and a photoelectrochemical test was conducted. The results are shown in Figure 32. It is evident how CoPi by itself produces very little current, which starts at voltage values corresponding to its oxidation potential. This shows how the enhancement of photocurrent due to CoPi deposition on $BiVO_4$ samples is the result of the combination between semiconductor's photoactivity and catalyst activity for water oxidation.

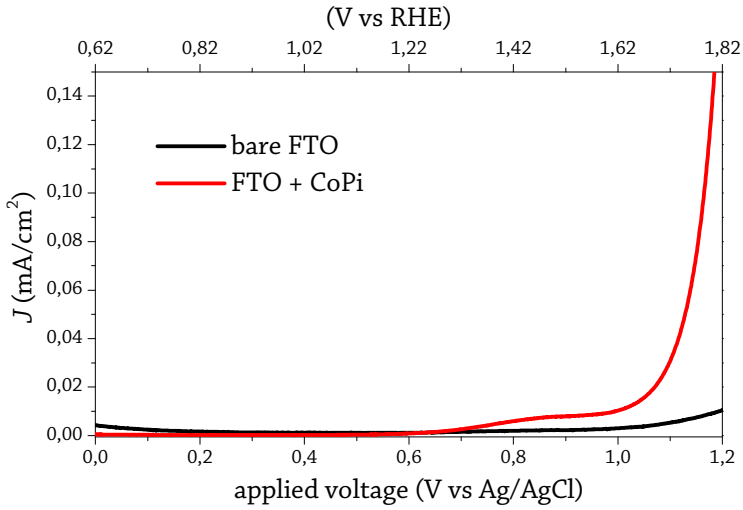

Figure 32: *JV* curves for a bare FTO-coated glass and CoPi deposited on a FTO substrate. Current is generated only at high voltages, correspondent to the oxidation of the catalyst. This proves that the enhancement of photocurrent measured when the catalyst is deposited on $BiVO_4$ samples is due to a combined effect between photoactivity of the electrode and catalytic activity for water oxidation of the CoPi.

4.3.3. Doping with W

While the deposition of a co-catalyst addresses the poor surface kinetics of a semiconductor for water oxidation, to improve the bulk properties of our samples a dopant was employed.

Doped samples were prepared with the same procedure of undoped ones, with the addition of small quantities of $W(OC_2H_5)$, namely 0.2%, 0.5% and 0.9% to the precursor solution. The W^{6+} should replace the V^{5+} cation in the $BiVO_4$ crystals, therefore when $W(OC_2H_5)$ was added, $VO(acac)_2$ concentration was also reduced, in order to maintain the Bi:(V+W) ratio equal to 1:1. All samples were synthetized depositing 16 layers on FTO, so difference in photoperformance could not be caused by difference in thickness.

The doped samples had a XRD pattern showing the same peaks of the undoped ones, which suggested no segregation of a WO_3 phase took place (Figure 33) and that the photoactive monoclinic crystalline phase of $BiVO_4$ was not affected by the introduction of a dopant. The UV-Vis absorption spectra of all samples presented the same profile, confirming the thickness to be equal for all of them (Figure 34). These results allowed us to assume that any possible photoperformance difference among these samples could only be attributed to the presence of the dopant.

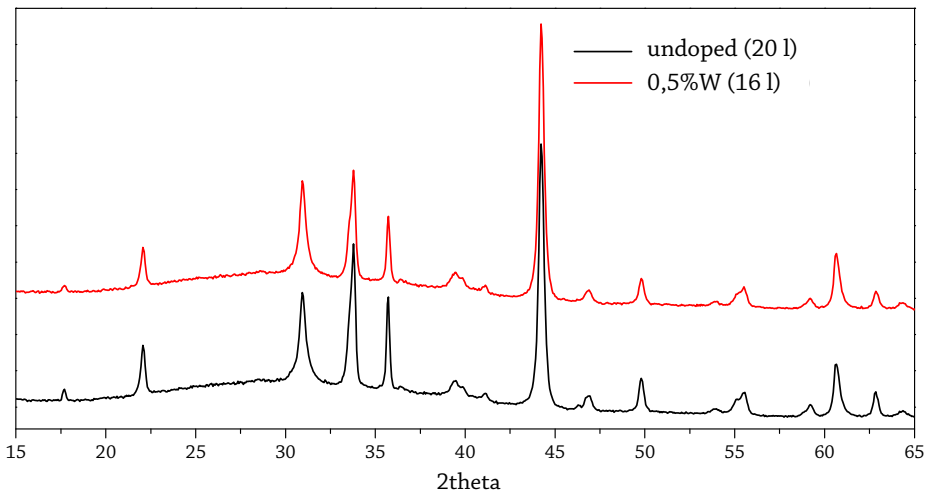

Figure 33: XRD of a doped $BiVO_4$ compared to a bare sample. No difference in the patterns and no extra peaks can be detected, suggesting that the atoms of the dopant were incorporated in the $BiVO_4$ crystal structure, rather than segregated in separate crystals as WO_3.

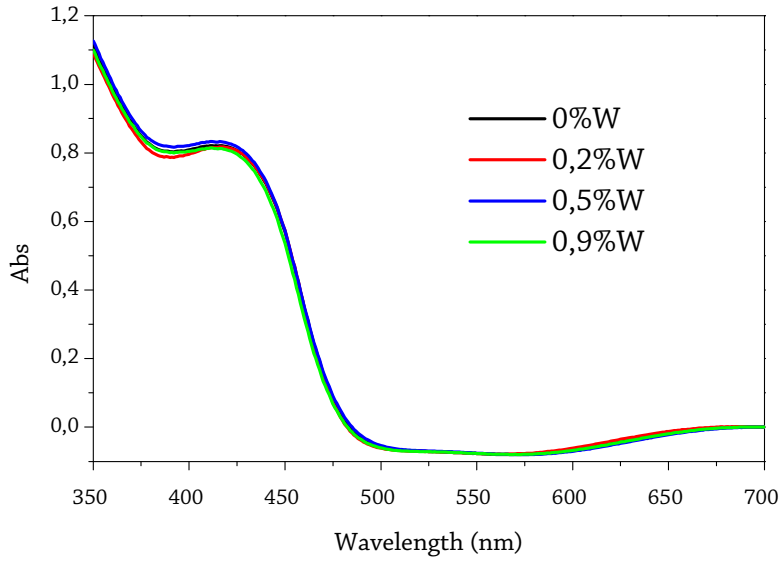

Figure 34: UV-Vis absorption spectra of $BiVO_4$ thin films with same number of layer deposited, but different concentrations of dopant. The perfect overlap of all spectra suggests that all samples have same thickness.

When photoelectrochemical tests were performed, the optimal concentration of dopant resulted to be 0.2% (Figure 35). This was confirmed by both experiments conducted with and without the addition of a hole scavenger. However, the experiments conducted in the presence of Na_2SO_3 showed that for concentrations above 0.5% , the photocurrent produced was lower than for undoped samples (Figure 36). This could be related to the presence of carbon, but in general, it is known that too high concentrations of dopant have a counterproductive effect.

Photocurrent densities produced by back and front illumination were also compared and the doped samples showed to have better photoperformance when front illuminated, as in the case of undoped samples. However, the difference in photocurrents was more pronounced in the case of doped samples than for the undoped one with same thickness (Figure 37).

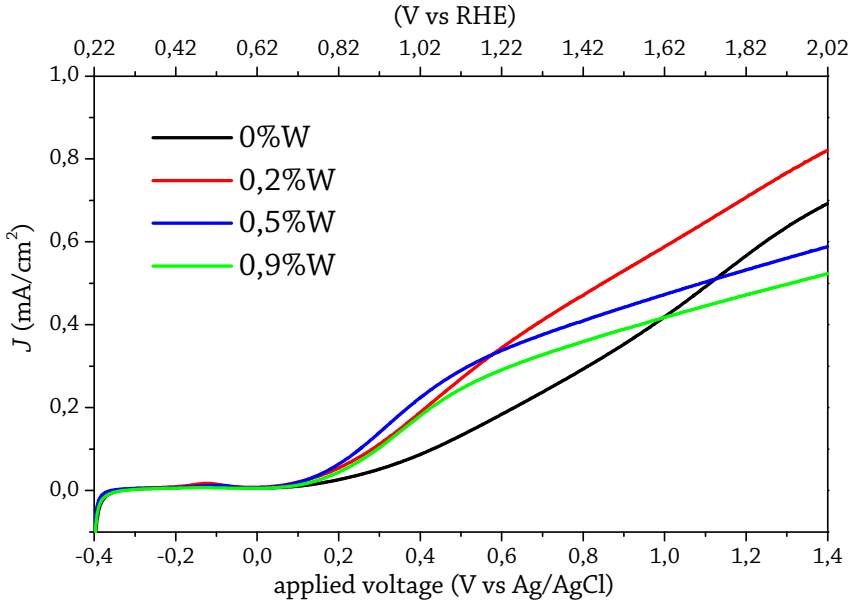

Figure 35: Photoelectrochemical performance of undoped $BiVO_4$ (black line) with $BiVO_4$ doped with different concentration of W (the percentage is referred to the amount of W added to the precursors solutions). The photocurrent is measured with the samples immersed in a phosphate buffer solution at pH=7. All samples have same thickness of 16-layers.

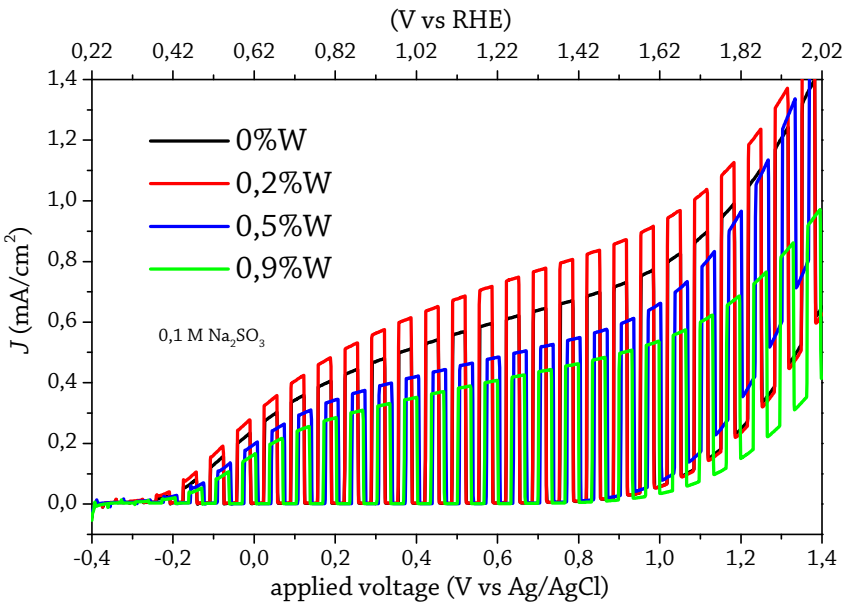

Figure 36: Photoelectrochemical performance of undoped $BiVO_4$ (black line) with $BiVO_4$ doped with different concentration of W (the percentage is referred to the amount of W added to the precursors solutions). The photocurrent is measured with the samples immersed in a phosphate buffer solution at pH=7, with the addition of a hole scavenger. The experiment was performed by exposing the sample to light and dark by means of a chopper. All samples where synthetized with same thickness of 16-layers.

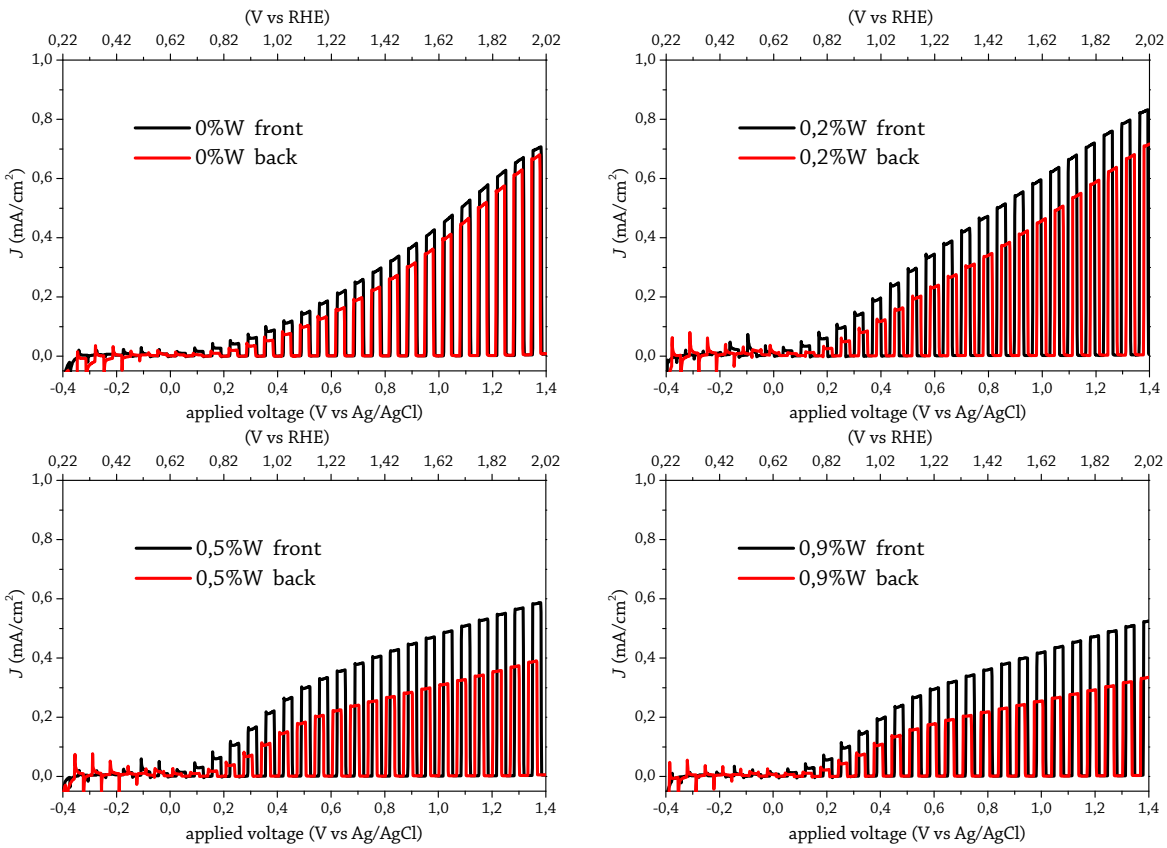

Figure 37: Comparison between front (black line) and back (red line) illumination in doped samples. As it was in the case of bare samples, also for doped $BiVO_4$ the photocurrent generated while illuminating from the front is higher than when illuminating from the back. However, when comparing these results to those of an undoped sample with same thickness (top-left plot), the difference between front and back photocurrents is more evident for doped samples.

4.3.4. Extra annealing treatment at 600°C

As we could see from the FIB-SEM front images, all samples seemed to have black areas distributed on the entire surface (Figure 39a). This was presumed to be residual carbon, which might be due to the use of acetyl acetone as only solvent for the precursor solutions preparation. To verify whether or not this was the case, it was decided to make the samples undergo an extra annealing phase at higher temperatures, that is to say 600°C, which should burn off the remaining carbon. $BiVO_4$ is in itself stable at temperatures higher than 550°C, while that's not the case for the glass support on which the samples are deposited. Therefore, this high temperature annealing treatment was carried on for 45 minutes only, while the samples were placed on a borate-silicate support, which prevented the glass from the melting. One sample for each thickness was treated at 600°C and then tested. At a first inspection, those areas that before the extra annealing step showed inhomogeneity in the form of small scattered spot, had become broader, making look the samples much less homogeneous than before. This was attributed to the presence of higher concentration of carbon in such areas, which might have affected the film growth negatively, leaving an even less homogeneous spot behind once the carbon was removed. To be noted is that such areas where mostly situated at the edges of the samples, leaving the middle still homogeneous and allowing the samples to be tested and compared to the pre-annealed results (see Figure 38). To confirm this

preliminary theory, FIB-SEM front images were taken. Images of the areas that still appeared homogeneous at the naked eye clearly showed the disappearance of the blackness from the sample surface (see Figure 30b).

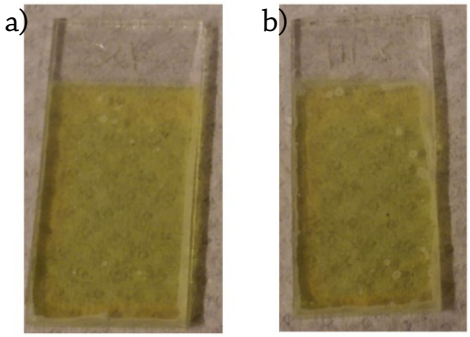

Figure 38: Picture of $BiVO_4$ thin film electrodes deposited on FTO-coated glass. a) Sample before the extra annealing step, b) sample after the extra annealing step at 600°C for 45 min. In the latter case the sample shows exposed FTO at the sides and in some spot distributed randomly on the surface.

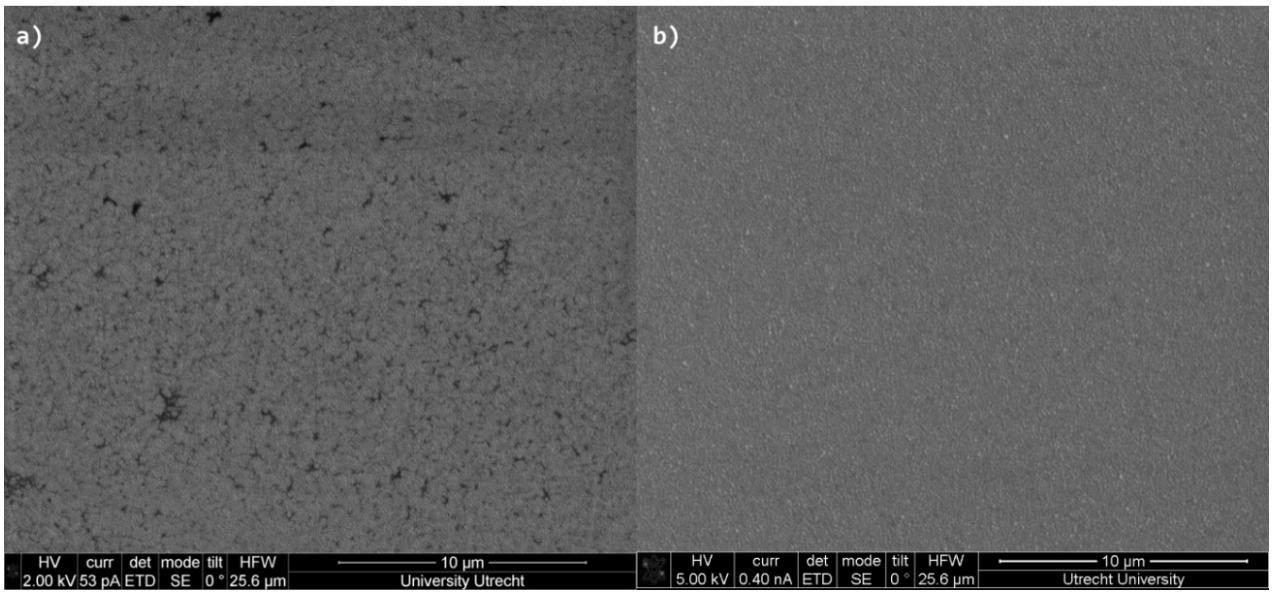

Figure 39: FIB-SEM front images of $BiVO_4$ on FTO. a) Pre-annealing step at 600°C; b) after annealing at 600°C for 45 min. The black areas are no more present after the extra annealing step.

A zoom-in was also done on the inhomogeneous areas. Two different phenomena were detected. On the small inhomogeneous spots on the sample, it seemed like the removal of carbon on those areas resulted in the exposure of the FTO beneath the $BiVO_4$ layer (Figure 43). This would prove the theory that those areas had a higher concentration of carbon, which did not allow the formation of crystalline $BiVO_4$ on that portion of the surface, leaving the FTO exposed once the carbon was removed. A second type of inhomogeneity was distinguished on the edges. In these areas not only the FTO was exposed, but also carbon was still present in large quantities. This is shown in Figure 44a and the zoom-in on such area (Figure 44b) showed agglomeration of residual carbon on top of FTO with no presence of $BiVO_4$. Figure 44c shows the same image after focusing the ion beam on the area marked by the red square. The agglomeration of carbon in that area appeared flattened after focusing the ion beam on it, which suggested the beam removed a fairly abundant portion of the carbon, confirming its amorphous phase.

These inhomogeneities are surely not desirable in semiconductor thin films. However, as already stated, since these two types of inhomogeneity where mostly placed away from the middle of the sample, which is the area normally tested during all experiments, the results obtained were accepted to be valuable for drawing conclusions about the effect of the decrease in carbon content. This was also considered after comparing UV-Visible absorption spectra and XRD between pre- and post-annealed samples. In fact, the UV-Vis spectra of the post-annealed samples overlapped almost perfectly with the pre-annealed ones, confirming that no change in absorption was evident for areas in the middle of the samples (Figure 40). The only exception was the case of the thickest sample (23-layers), which showed a decreased absorption (Figure 41: UV-Vis absorption spectra of the 23-layers sample compared to the 20-layers one. The 23-layers post annealed absorbs less than the pre annealed one, but still more than the post annealed 20-layers sample.Figure 41), but was still higher than the absorption of the 20-layers sample. Nonetheless, this should be considered when drawing conclusion about the photoperformance of this particular sample. Also the XRD of pre and post-annealed samples showed the same pattern, therefore we could also deduce the annealing step removed amorphous carbon, while not affecting the crystallinity of $BiVO_4$ (Figure 42).

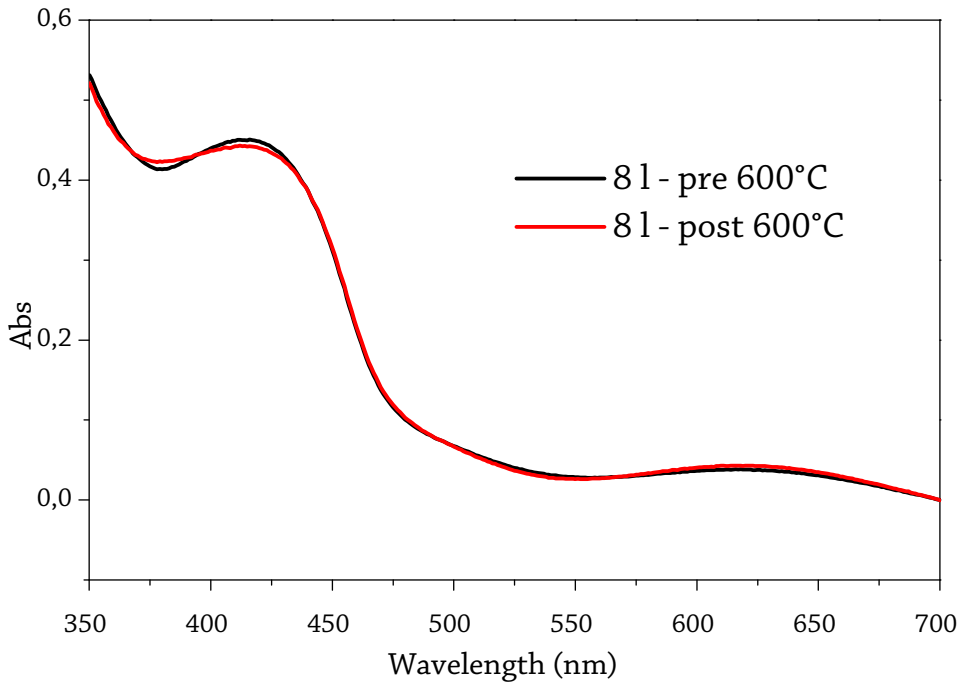

Figure 40: Comparison between the UV-Vis absorption spectra measured on an 8-layers sample before (black) and after (red) the annealing step at 600°C.

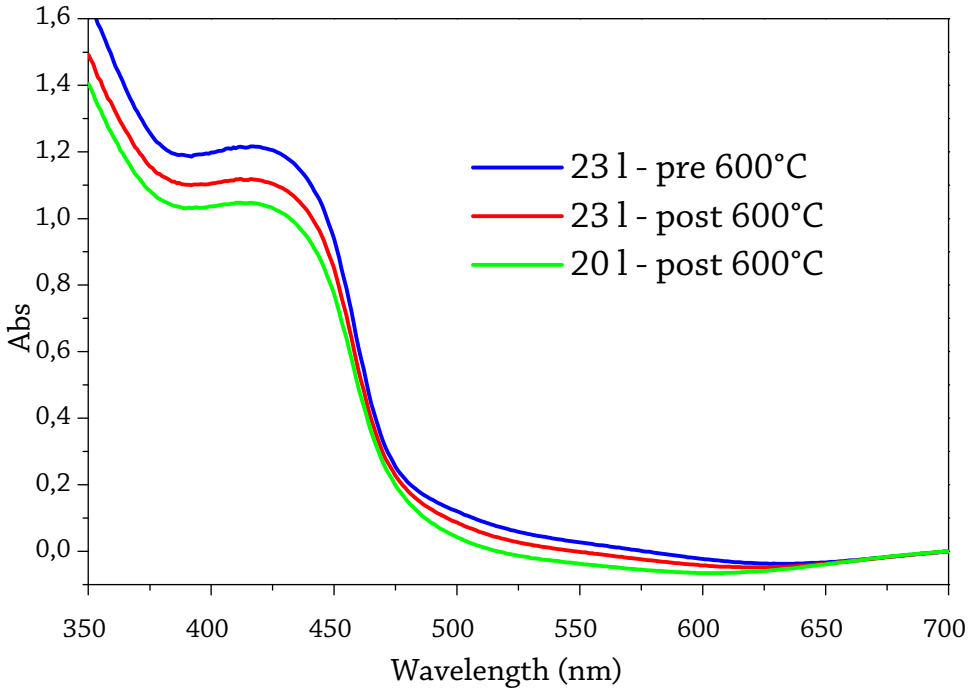

Figure 41: UV-Vis absorption spectra of the 23-layers sample compared to the 20-layers one. The 23-layers post annealed absorbs less than the pre annealed one, but still more than the post annealed 20-layers sample.

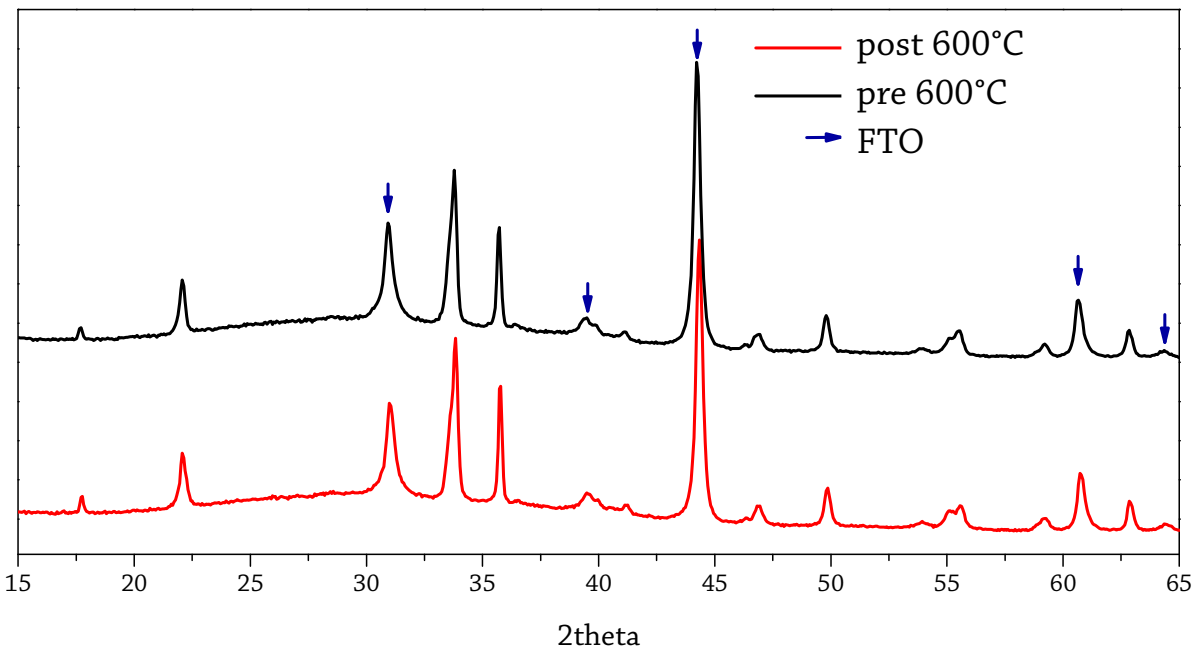

Figure 42: Comparison of XRD analysis of samples before (black) and after (red) the annealing step at 600°C.

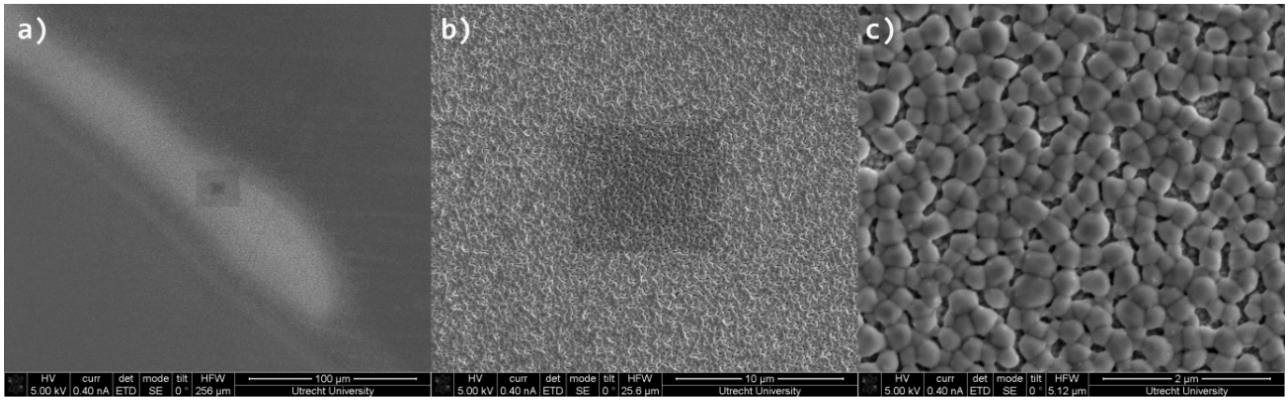

Figure 43: FIB-SEM front images of an area presenting inhomogeneity of the first type. At the naked eye the dark grey area in image a) appeared as scattered. The zoom-in on such area in b) 10 µm scale and c) 2 µm scale show $BiVO_4$ not completely covering the substrate surface, leaving exposed FTO.

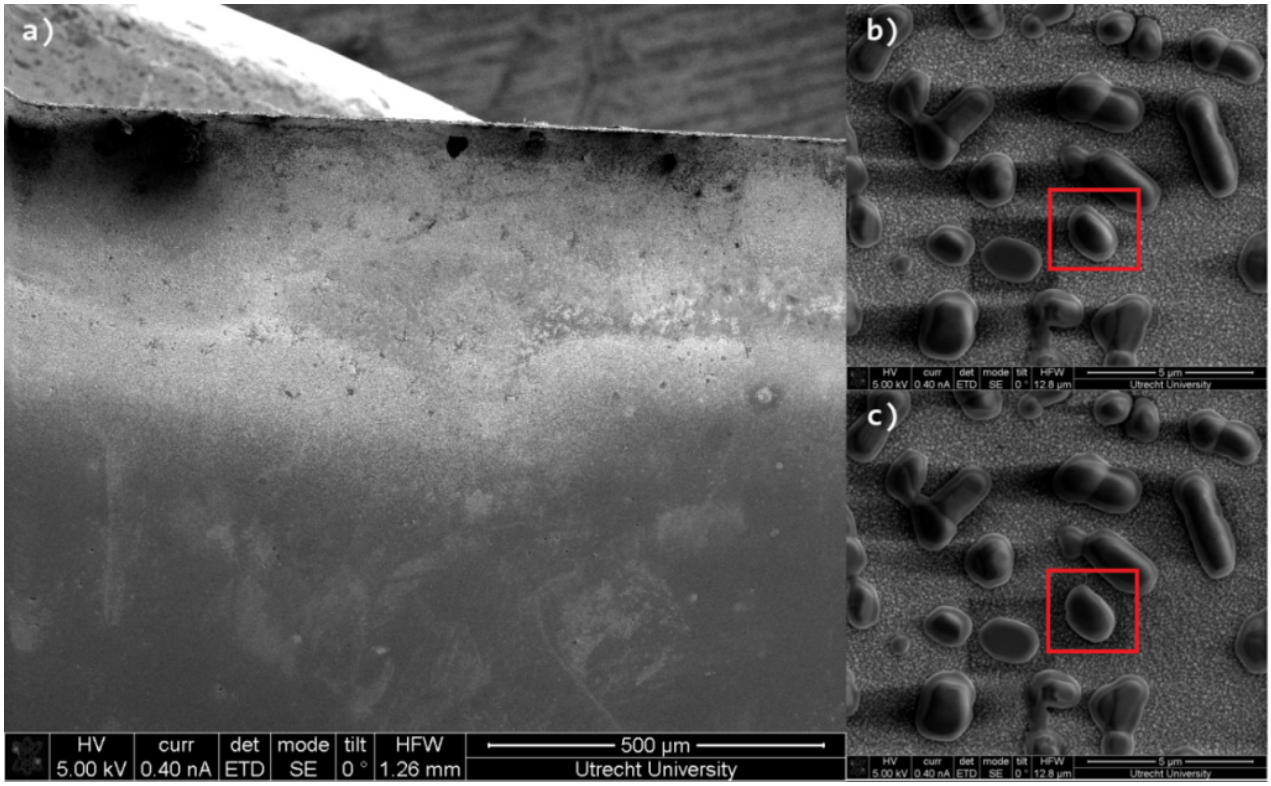

Figure 44: a) FIB-SEM front images of an area presenting inhomogeneity of the second type on the edges of the sample. At the naked eye such areas look scattered and highly inhomogeneous. b) Zoom-in on such area showed agglomeration of residual carbon. c) The same image after focusing the ion beam on the red square. The agglomeration of carbon on that area appeared flattened, which suggested the ion beam removed a fairly abundant portion of the carbon, confirming its amorphous phase.

The samples that were treated at higher temperatures were then tested to check how the removal of carbon affected their photoperformance. This extra annealing step proved to have a positive effect on all samples, as shown in Figure 45a. As mentioned, the 23-layers sample was the only one showing evident lower UV-Vis absorption and we can also see that the improvement in its photoperformance is not as great as those of the other samples. Nonetheless, the removal of carbon surely enhanced the performance of all samples. The effect is even more evident when testing them with back illumination. Before the removal of carbon, the back illumination

showed to generate lower photocurrents than the front (Figure 29b) On the contrary, after the annealing step at 600°C, the back illumination improved in such way to overcome the performance by front illumination (Figure 45b). This was verified for all thicknesses above 12 layers, while for the thinnest sample the difference between front and back was still negligible.

The post annealed samples tested in presence of a hole scavenger showed also higher photocurrents generated by back illumination compared to those produced by front illumination (Figure 46), while this was not the case before the treatment at 600°C.

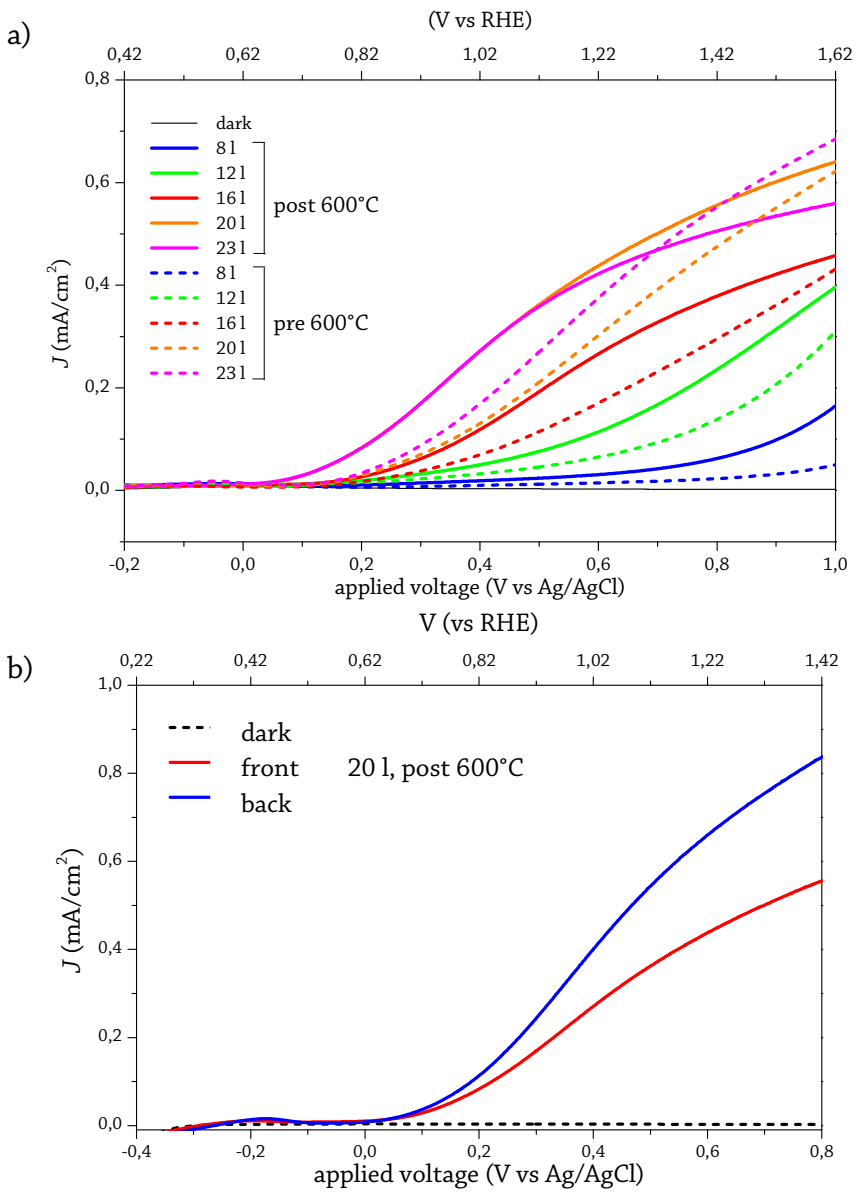

Figure 45: a) Comparison of photoperformance by front illumination of samples before (dashed lines) and after (solid lines) the annealing step at 600°C. b) Comparison between front (red line) and back (blue line) illumination in a post annealed sample. The measurements are performed in a phosphate buffer at pH=7.

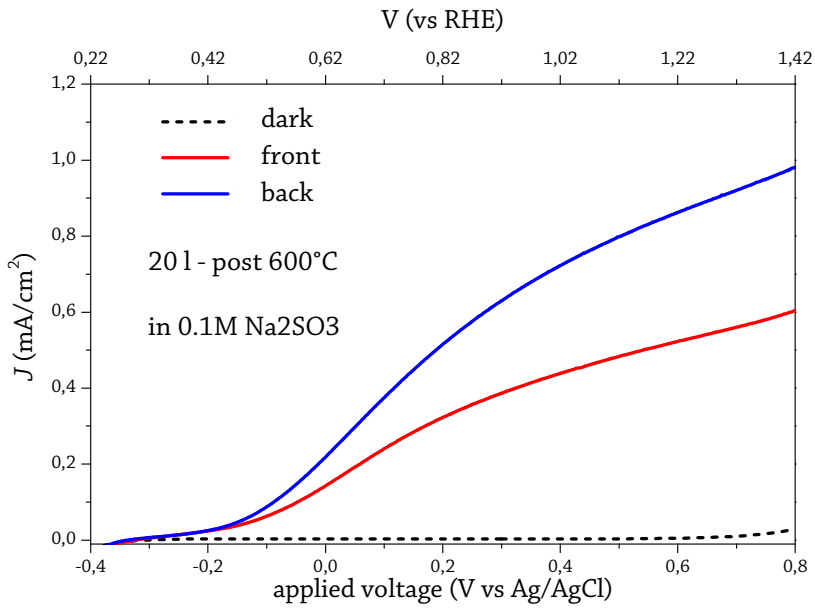

Figure 46: Comparison between front (red line) and back illumination (blue line) in a post annealed sample. The measurements are performed in a phosphate buffer at pH=7, with the addition of 0.1M Na_2SO_3 as hole scavenger.

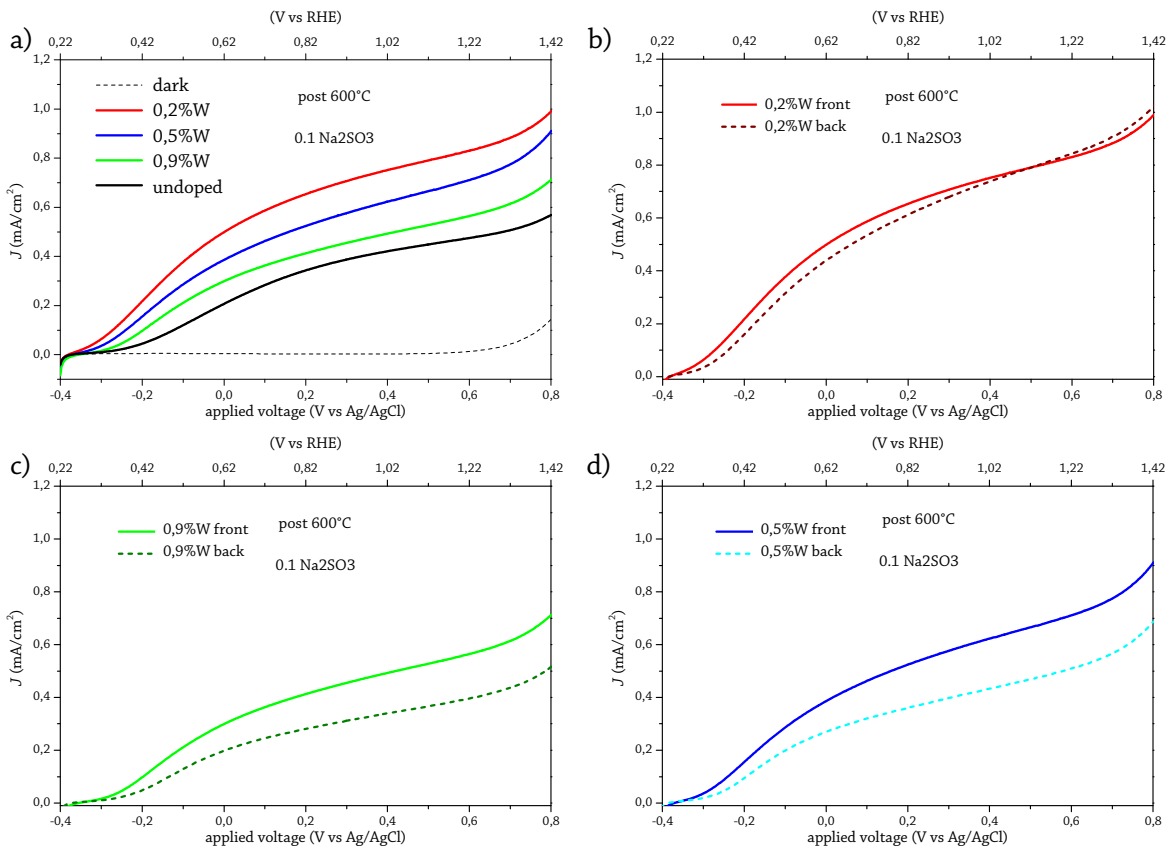

Figure 47: a) Photoperformance comparison by front illumination of samples with concentration of dopant between 0% and 0.9%, after the annealing step at 600°C. The inset shows the results obtained before the extra annealing step. Comparison between front and back illumination in a post annealed sample with b) 0.2%W, c) 0.5%W and d) 0.9%W. The measurements are performed in a phosphate buffer at pH=7, with the addition of 0.1M Na_2SO_3 as hole scavenger and all samples where synthetized with the same number of 16-layers.

The extra annealing step was carried out as well on the doped samples and also in this case the improvement was not negligible. Before the annealing step, we found out the optimal concentration which improved bulk performances of our samples was 0,2% of W, while higher concentrations seemed to affect negatively $BiVO_4$ (Figure 36). However, after annealing at 600°C, even higher concentration of W outperformed the undoped samples, with 0,2% still being the best concentration of the investigated range (Figure 47a). Nonetheless, unlike the results obtained with the undoped samples, the comparison between back and front illumination still showed better higher photocurrents when the samples where illuminated from the front (Figure 47c-d). The only exception was the case of the sample with 0.2% of W, which showed essentially same photocurrents irrespective of the light source's position (Figure 47b). This finding confirms that such concentration of dopant is the optimal amount which benefits the bulk transport kinetics of charge carriers.

4.3.5. Structural and photocatalytic results summary

From the structural analysis it was possible to establish that the films prepared were homogeneously covering the FTO substrate, with the exception of few scattered spots randomly distributed on the sample. In all cases the monoclinic photoactive phase $BiVO_4$ was successfully synthetized, also for doped samples, even though band gaps values calculated from the Tauc plots revealed to be of 2,65 eV, slightly higher than expected. Furthermore, the deposition of one layer corresponded to an increase in average thickness of approximately 5 nm, with a consequent increase in particle size as detected form SEM images.

However, the presence of black areas on the surface of the sample, which were detectable only by FIB-SEM analysis, made us believe that carbon had not entirely been removed. This was confirmed by the almost complete disappearance of such areas after the samples were put through an extra annealing step at 600°C. However, to be noted is that at naked eye inspection the samples homogeneity seemed to be compromised after this treatment, especially on the edges. FIB-SEM analysis on those areas revealed that high concentrations of carbon were still present, while in few spots the FTO resulted exposed. Nonetheless, these areas were mostly placed away from the centre of the sample, which is the area illuminated, i.e. tested, during photocatalytic experiments. For this reason the samples were considered more than acceptable to be used in the investigation of the effect of carbon removal from the $BiVO_4$ synthetized during this project.

The photocatalytic analysis on bare $BiVO_4$ synthetized with incremented number of layers revealed that the increase in thickness corresponded to a rise absorption and photocurrent produced. This results are summarised in Figure 48, were the values of photocurrent densities corresponding to an applied voltage of 1.23V vs. RHE are reported. The reason of this choice is that this is normally the reference value used to compare results in literature. The performances of samples both before and after the extra annealing step are shown.

Before the annealing at 600°C, the photocurrent density increased almost constantly with thickness. This was expected, since more intense light absorption corresponds to higher concentrations of photogenerated charge carriers, therefore higher photocurrent densities produced. However, experiments with back illumination (blue circles in Figure 48) revealed to produce lower photocurrent than with front illumination (red circles), which was unexpected for a semiconductor like $BiVO_4$, which electrons mobility was reported to be very slow. In fact,

photocurrents are predicted to be higher when generated by back illumination, since in such case the excited electrons would be generated next to their destination, the back contact. The unusual behaviour of our samples was attributed to be caused by the presence of residual carbon. It is possible that, in the presence of carbon, charge carrier mobility in the bulk of the semiconductor was compromised to the point of lowering substantially the conductivity properties of the material. Furthermore, carbon was mostly present at the surface, severely impairing the injection of holes to the electrolyte. As a confirmation of this suspicion, after the treatment at 600°C, the photoperformance with both front and back illumination conditions improved drastically, with back illumination (blue triangles) overcoming the values of front illumination (red triangles).

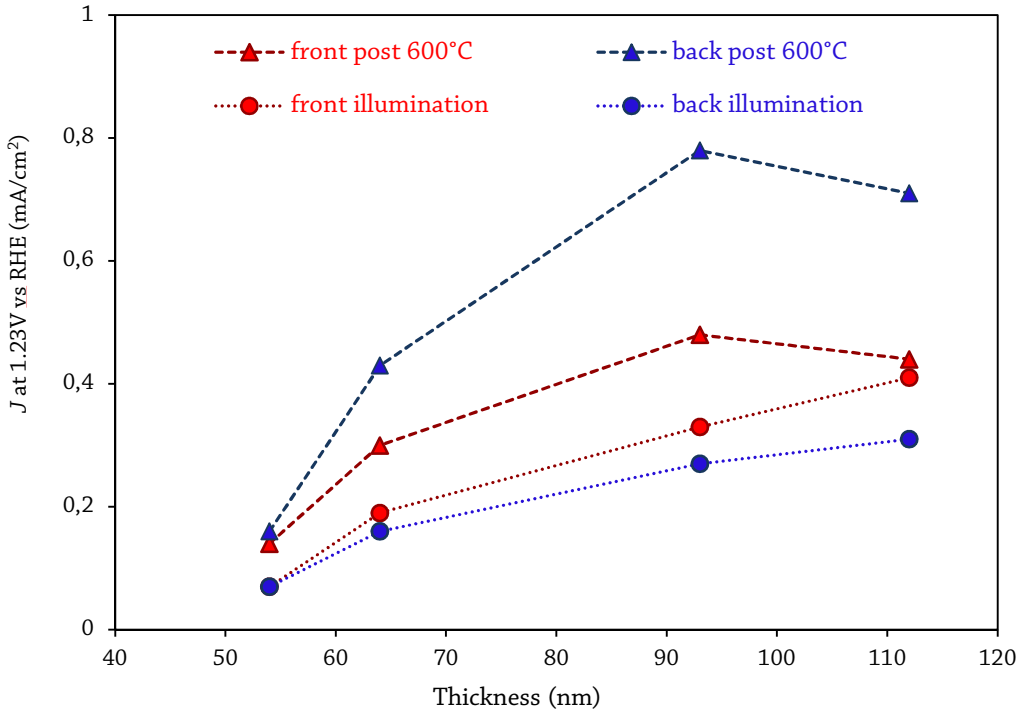

Figure 48: photocurrent at 1,23 V as a function of thickness, for bare samples of $BiVO_4$ synthetized by spin coating. The increase in photocurrent brought by annealing the samples at 600°C in clearly evident for all thicknesses, particularly for the back illumination

When analysing the performances of the samples after the treatment at 600°C, we noted that the increase of photocurrent density was constant only up to the 20-layers sample, while for 23-layers the photocurrent started to decrease. Partially this was due to the fact that the UV-Visible absorption for the 23-layers sample after the extra annealing step showed lower values than the same pre-annealed sample. Whatever the cause, this means that a lower amount of charges was now generated, which surely has a negative effect to the photocurrent density achievable. However the absorption of the post-annealed 23-layers sample wasn't as low as that of the post-annealed sample with 20-layers. This implies that the concentration of charges generated in the 23-layers sample will still be higher than in the 20-layers one. Therefore, the decrease in photocurrent cannot be only due to its lower absorption, but probably to the fact that recombination of the generated carriers is now more pronounced. This consideration is used to conclude that a thickness of a 100 nm can therefore be assumed to correspond to the

optimal thickness for $BiVO_4$ samples, after which recombination phenomena become too prominent. This is in compliance with the reported calculated value of holes diffusion length, which is in fact about 100 nm.[46]

The analysis of bare samples in an electrolyte where a hole scavenger was added were a clear indication of the slow water oxidation kinetics at the surface. The deposition of a co-catalyst was found to be a good expedient to overcome such problem. The results obtained from the photoassisted deposition of CoPi are reported in Figure 49. We can see that in all cases the addition of CoPi improved the photocurrent produced almost to the point of reaching that of the bare sample tested in presence of a hole scavenger. As already explained, this is an indication of the fact that the co-catalyst deposition was successful and that CoPi worked indeed as good catalyst for water oxidation when deposited on our samples. However, the effect seems to be more pronounced for thinner samples. Nonetheless, only few samples were tested, therefore further experiments should lead to more representative conclusions.

Furthermore, CoPi was deposited on samples that did not undergo annealing at 600°C, but we can expect that depositing the co-catalyst on a sample from which carbon has been remove, should bring an even higher photocurrent density

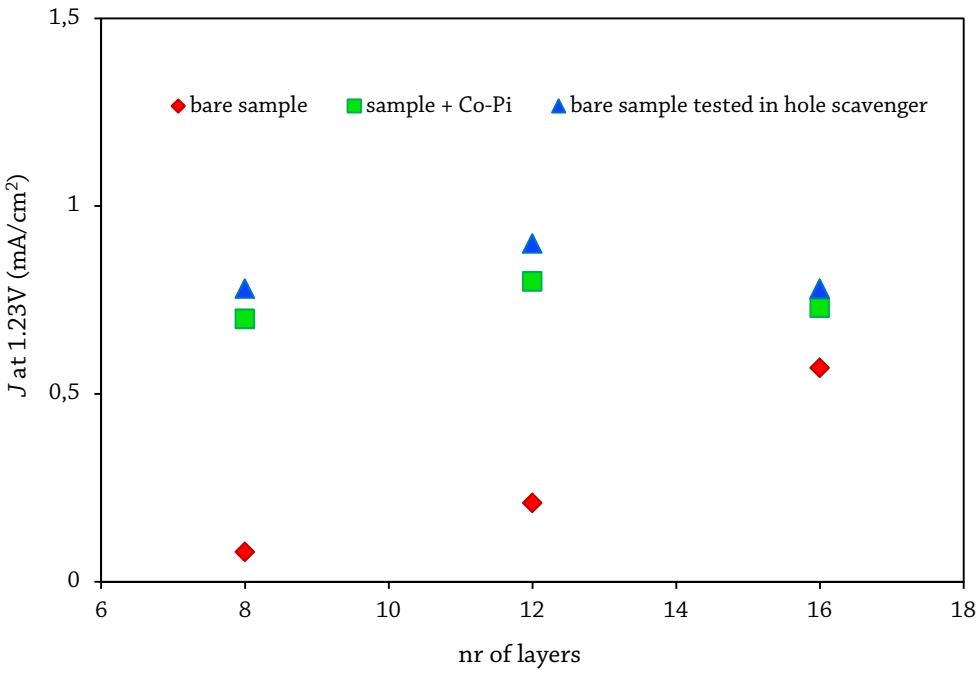

Figure 49: photocurrent at 1,23 V vs. RHE as a function of thickness. The comparison is made among bare samples(red rhombus), bare samples tested in presence of a hole scavenger (blue triangle) and sample with deposited CoPi tested in a normal electrolyte (green square). For all samples, the photocurrent increased when a co-catalyst was deposited. The performance of bare samples in a hole scavenger is used as a reference point of performance achievable when increasing drastically the surface kinetics.

The bulk properties were then tuned by the addition of a dopant. The results are shown in Figure 50, where photocurrent density values are reported for samples tested in presence of a hole scavenger.

At a first inspection, among the range of concentration tested, 0,2%W in the of precursors solution seemed to allow the synthesis of samples with enhanced photoperformance than the correspondent undoped ones. On the other hand, higher amount of dopant showed to limit the performance of $BiVO_4$. This is associated to the fact that the W^{6+} ions of the dopant are substituting the V^{5+} ions in the $BiVO_4$, and if their presence is too pronounced, the crystal structure will be altered to an extent that will cause a loss in photoactivity. On the contrary, an optimal amount of dopant should be low enough to enhance the concentration of charge carriers without putting too much stress onto the crystal structure of the semiconductor.

However, since the presence of carbon affected the undoped samples performances, we expected it to be the case for doped samples as well. This was confirmed by annealing the samples at 600°C and comparing the resulting photoperformaces (green triangles in Figure 50) to the pre-annealing ones (black circles).

After the removal of carbon, all samples showed a higher photocurrent. Now also concentration of W higher than 0,2% seemed to have a positive effect on $BiVO_4$ performance. Nevertheless, the optimal concentration was confirmed to be 0,2% of W.

It should be noted that the results reported in the graph are those of the samples tested in presence of a hole scavenger. Since in this condition surface transport kinetic to the electrolyte is considered at is maximum, the still evident improvement in photocurrent shows how the removal of carbon affected also the bulk properties of our samples. This is an indication of the fact that carbon was present not only at the surface, but in the bulk as well and that its concentration was reduced in both locations.

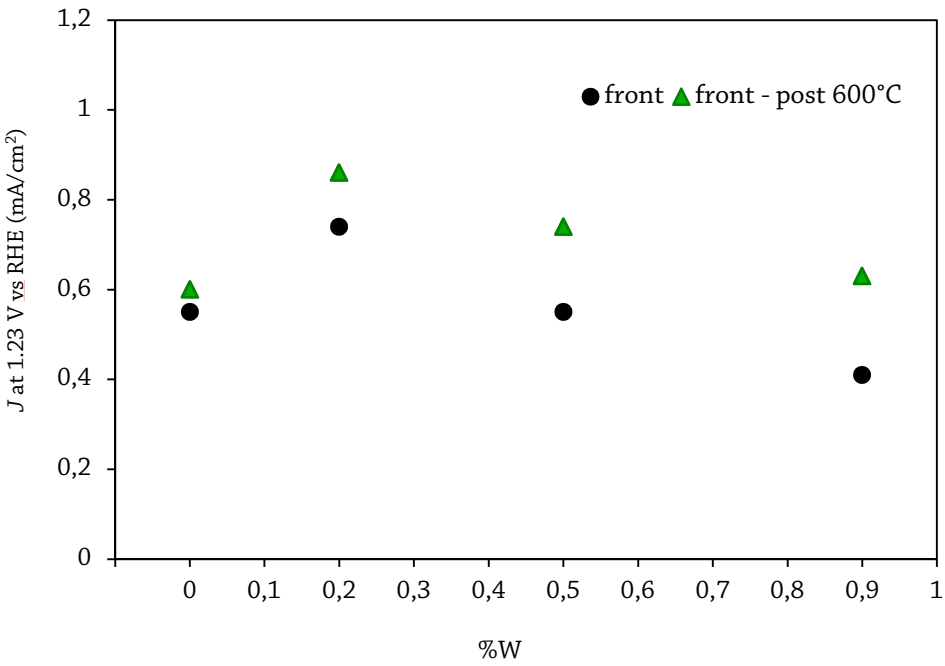

Figure 50: Photocurrent values at an applied voltage 1,23 V vs. RHE for samples tested in presence of a hole scavenger, as a function of dopant concentration, The increase in photocurrent brought by annealing the samples at 600°C in clearly evident for all sample, with a more significant improvement for doped films.

4.4. Charge dynamics investigation

4.4.1. TAS results

A final characterization of the $BiVO_4$ samples was done by means of a transient absorption spectrometer with which we can investigate the dynamics of excited species.

Firstly, we tested the samples in air, exploring the effect of the increase in excitation energy. In such condition, the sample was not connected in a close circuit, i.e. the electrolyte was missing and no connection was made to the back contact. Therefore, the decrease in concentration of the excited species should be entirely due to recombination phenomena or trapping of the charge carriers to different energy states.

Figure 51 shows the ΔAbsorption spectra of the 20-layers sample. Nonetheless, all samples were tested and the same conclusion was drawn for the whole batch. The spectrum profile is found to be similar to those reported by Ravensbergen et al.[67] The absorption maximum is found at values around 465-470 nm, which corresponds to the calculated band gap of 2,65 eV. This band situated in the visible is assigned to hole absorption, while free electrons are expected to absorb in the near-IR region.[62,67] As predictable, higher pump powers correspond to more intense absorption, since a higher concentration of charge carries is generated. A red shift of absorption maximum was also detected with increased excitation energies. This behaviour was also reported in literature.[67] The ground-state bleach is visible at around 430 nm. This is to be expected since upon 355 nm excitation (3.50 eV), an excess energy of 0.85 eV in respect to the band gap is given to the charges. This results in the excitation of electrons from more positive potential than the valence band edge, which justifies the position of the bleach band to the high-energy (low wavelength) side of the spectrum.

In Figure 52 are reported the correspondent normalized time traces. It is noticeable that, after a very fast increase in absorption, which corresponds to the generation of excited species, follows a decay in time with the signal decreasing to zero within 100 μs. Furthermore, by plotting the time traces with a logarithmic horizontal scale, it was evident that such time decay seemed to be composed by two contributions, a fast one in the order of ns and a slower one in the time scale up to 100 μs. The nature of these contributions will be treated in the next section (4.4.2). Without going into a more quantitative analysis yet, as a first investigation, we could see that such decays profiles were influenced by different excitation energies. The most evident effect was the broadening of the signal with increasing energies, which was not perceived with any other following type of test performed.

For example, if we compare the decay traces of samples with increased thickness, but same excitation energy (Figure 53a), we can see that the decays are effected by the thickness of the sample, but no broadening of the signal is detected.

Since different performances were obtained in the photoelectrochemical setup when the sample was illuminated from the back, experiment with back illumination were also performed with the transient spectrometer. The results are reported in Figure 53b and we can see how back illumination seems to generate much longer lived excited species. To be noted is that the difference between back and front illumination was tested for all samples, in air and with a range of different pump intensities. A difference between back and front illumination was noted

in all cases, with the exception of the thinnest sample, when excited with pump intensity lower than 1.0 mW, which is reasonable and to be expected.

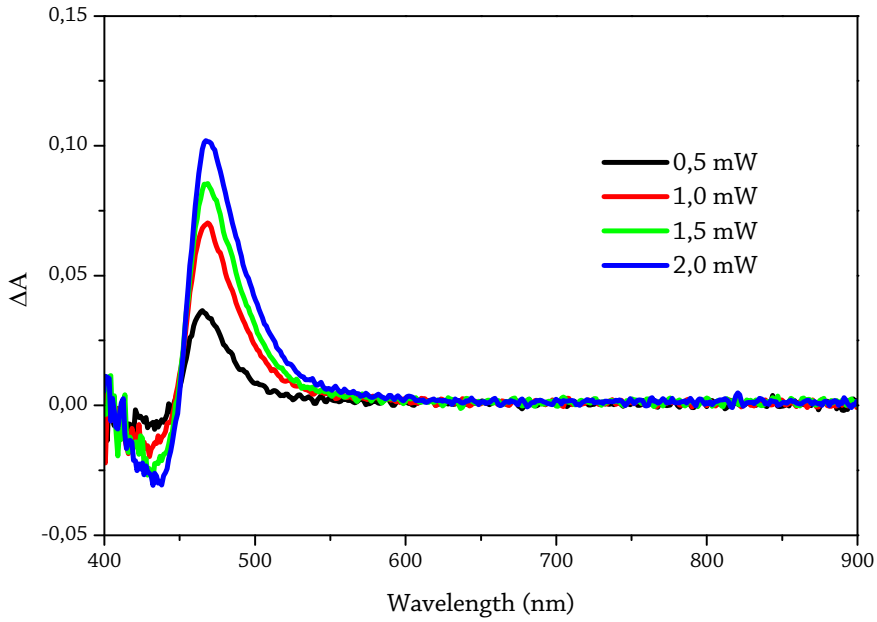

Figure 51: Transient ΔAbsorption spectra at a selection of delay time for $BiVO_4$ in air, at different excitation energies. The results here reported refer to the 20-layers sample, but similar effects were found for all thicknesses.

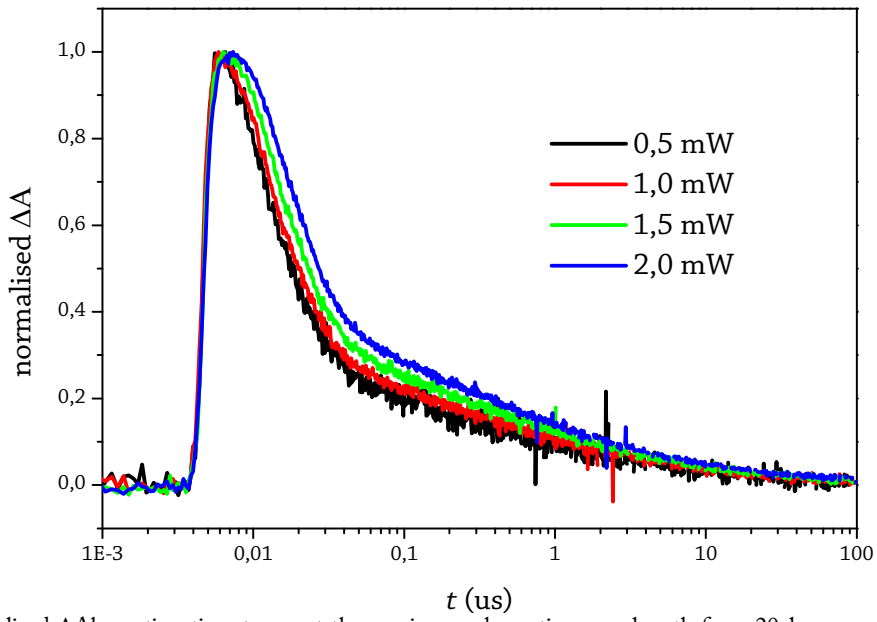

Figure 52: Normalised ΔAbsorption time traces at the maximum absorption wavelength for a 20-layers sample excited with increasing pump energies. To better discern differences in decay traces, the horizontal axes is converted to a logarithmic scale.

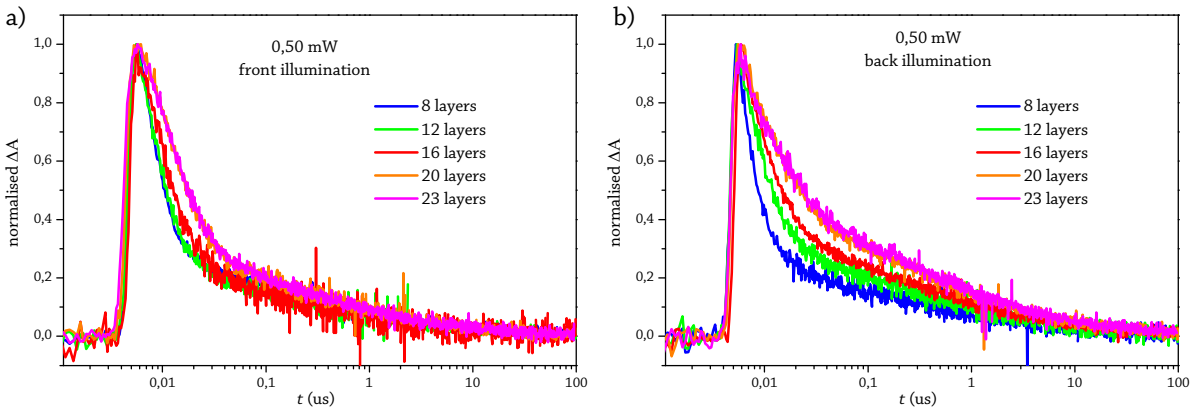

Figure 53: a) Normalised absorbance decay in time at the maximum absorption wavelength for a set of samples with increased thickness. b) Same time traces obtained by illuminating the samples with the laser from the back side.

By means of a sealed cuvette, the samples were also tested in different gaseous atmospheres than air, namely Ar and O_2. Such experiment was meant to exclude the possible accumulation of charge carriers, namely electrons, at the sample surface. Ar is indeed an inert gas, while O_2 should function as electron scavenger. The results of such investigation are shown in Figure 54. As we can see in Figure 54b, both time traces of samples in Ar and in O_2 perfectly overlap the one in air, suggesting that no difference in charge dynamics was influenced by the presence of an electron scavenger. The same outcome was detected for all samples.

Another interesting finding during such experiments was that absorption intensity could not be correlated to charge carrier concentration in a reproducible way. Figure 54a represents the absorption spectra profiles of the three different experiments conducted on the 20-layers sample. In this case the cuvette and the sample were kept in position, while the gases were injected into the cuvette prior each experiment. With this technique no adjustment to the spectrometer optics was necessary and, as a result, the absorption spectra were completely identical. On the other hand, the same kind of experiment was conducted using a different procedure. This time, the cuvette was removed by its position to allow an easier injection of the gases, while the experiment in air was simply performed with no cuvette. As depicted in Figure 54c, the absorption intensities resulted quite different from each other, and this is due to the fact that the overlap between probe and pump required to be adjusted prior each experiment by slightly regulating the optics positions. Since this procedure was performed manually, reproducing a perfect overlap with every measurement was not trivial. If the probe does not perfectly overlap with the pump, then the excited species generated will not be probed in their total amount, therefore absorption signal intensities could not be correlated to the exact concentration of species generated. Nonetheless, the normalization of the time traces in both cases showed to be perfectly matching, as seen in Figure 54d. This was expected, because even though not all the excited species where probed, their behaviour was reflecting the presence of their total amount. This made us conclude that, even if absorption intensities were not easily reproducible and, therefore not quantifiable, their time traces would always be accurate and the conclusion by them obtained, meaningful.

This also means that such irreproducibility of absorption intensities would occur in other experiments, for example any time that a new sample needed to be placed in position, or due to the fact that some experiment were conducted with a cuvette and some other without. Since the differences in absorption were also in these

cases due to the same problematic, an equivalent conclusion can be assumed to be true for all experiments conducted.

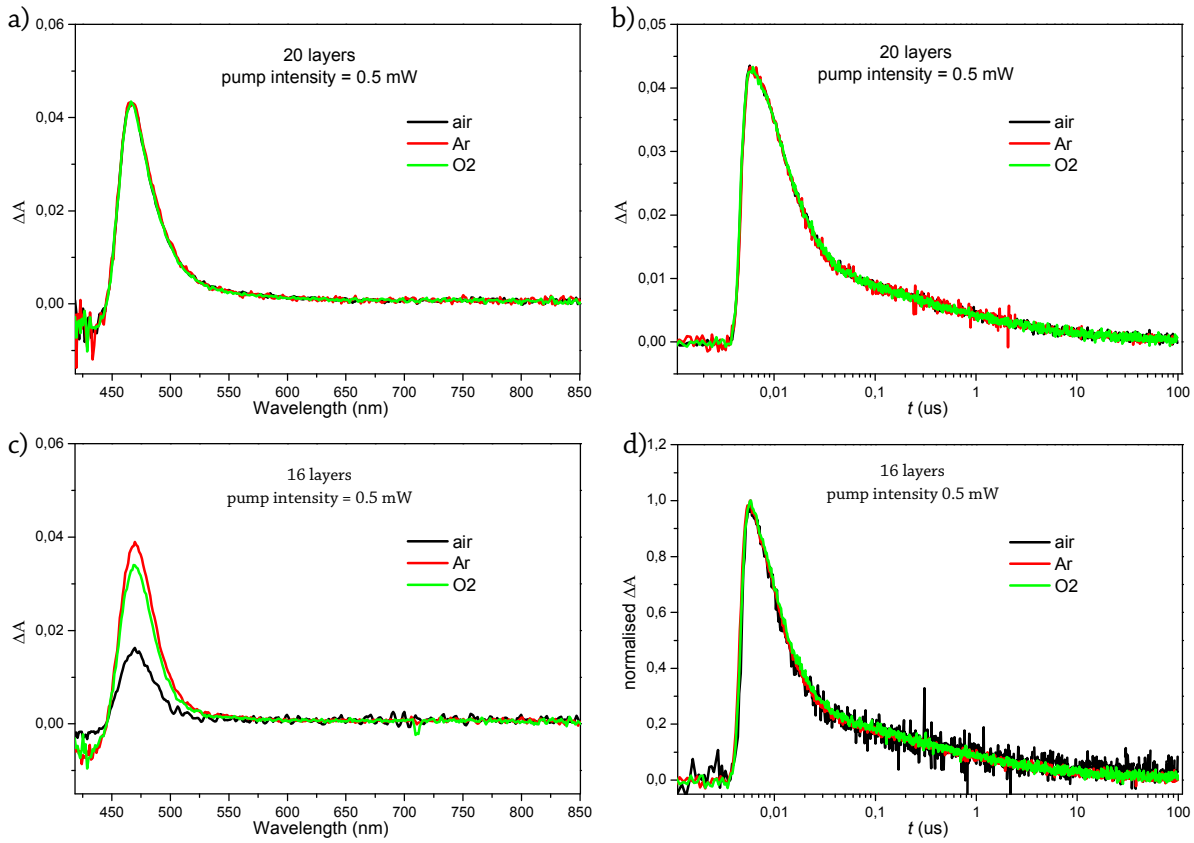

Figure 54: a),c) Transient absorption spectra at a selection of delay time for $BiVO_4$ in air, Ar, and O_2, with fixed pump intensity of 0.50 mW. b), d) Corresponding normalized absorbance decay in time at the maximum absorption wavelength.

To further investigate the charge carrier dynamics, we tested the effect of the presence of a CoPi co-catalyst on the surface of our sample. Such test was conducted in air and no difference was observed when compared to the time trace of the same sample without the deposited co-catalyst. Such results were confirmed for all samples and with both low and high excitation energies (a representative example is reported in Figure 55a). This could be simply due to the fact that in absence of an electrolyte, the semiconductors bands are still flat and the co-catalyst holes scavenger function cannot be triggered if no electrolyte is there to accept holes from it.

Subsequently, the samples were tested in the same electrolyte employed during photoelectrochemical measurement. Once the sample is in contact with the electrolyte, the conduction and valence bands bends in proximity of the surface, due to the exchange of charges between electrode and electrolyte, as explained in section 1.2.2. Such change is expected to influence charge carrier dynamics and should be therefore be detected by transient absorption experiments. In Figure 55b we can see that this is the case for our samples, even though the difference is hardly detectable. The decay seems to occur faster when the sample is immersed in the electrolyte, compared to the sample in air. However, no difference is detected when a hole scavenger is added to the solution.

Therefore, the same could be expected when testing the CoPi loaded sample immersed in an electrolyte. Again, this was verified for all samples with different excitation energies.

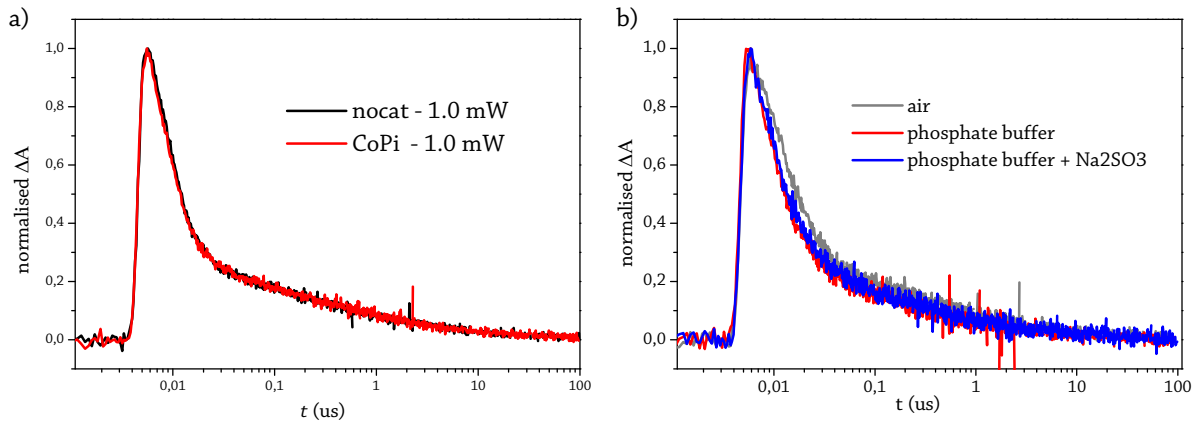

Figure 55: a) Normalised time traces of a 12-layers sample tested in air and the same sample with deposited CoPi co-catalyst on its surface, also tested in air. b) Normalized time traces of the ΔAbsorption of a sample tested in air, in a buffered electrolyte and in the same electrolyte with the addition of 0.1 M Na_2SO_3 as hole scavenger.

Finally, the effect of an applied voltage was tested on the $BIVO_4$ samples. At a first inspection, values of applied voltages below and included 0.0 V showed to have overlapping time traces, while when a positive voltage was applied, the time traces seemed to decay faster, especially in the range up to 0.1 μs (see Figure 56a). During trial experiments performed earlier, higher voltages were also tested, and in those cases it was immediately noticed how the absorption maximum decreased with the time of data collection. This was attributed to the damaging of the sample on the spot hit by the laser, which could also be verified by naked eye. Therefore, the doubt was that this could be the case also for lower positive applied voltages, even if such consequences where not immediately identifiable. A further analysis confirmed such doubt. It was possible indeed to divide the collected data of the first ten minutes and compare them to the averaged data on the total time of 20 minutes. The time traces of the first ten minutes of data collection were indeed overlapping (see Figure 56b), unlike those of the total 20 minutes of measurement. It was clear that the absorption decayed in time, and quite noticeably (see Figure 57a). This can confirm that the sample got indeed ruined, even if slightly, causing the absorption signal to decrease. Furthermore, the fact that the decay seemed faster mainly at its beginning can also be explained. If the absorption at a fixed delay time actually decreases due to the damaging of $BiVO_4$, the average of such spectra will also decrease every time that a new spectra is collected at that delay time. In the methods we described how and why more spectra are collected at the beginning of the decay, while at the end of the decay, only few spectra are collected. This means that the decrease in absorption will have a major effect on the beginning of the decay, while at the end, the noise will be quite elevated and the decrease in absorption less noticeable. Consequently, if the data are collected for a long time, the difference between beginning and end of the decay will be much more evident.

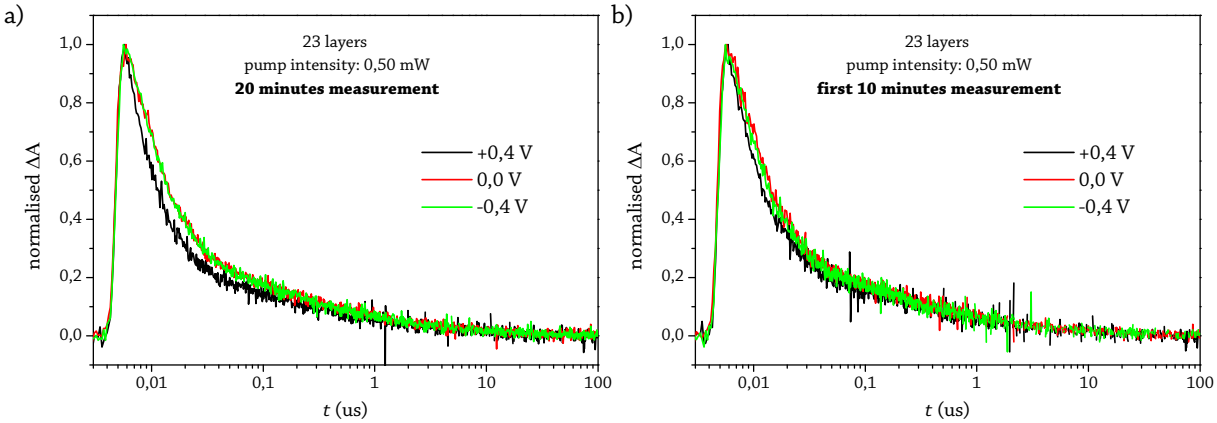

Figure 56: a) Time traces at the maximum absorption wavelength (467 nm) for a 20-layers sample, excited with 0.50 mW pump intensity and under different applied voltages. Appling a voltage of 0.4V seems to result in a slightly faster decay. b) First ten minutes of data collection of the same time traces.

As a further confirmation of this theory, another experiment was conducted with a positive applied voltage, with a slight modification in the procedure of data collection. In this experiment, for the first 10 minutes the software was allowed to collect data in the usual way, while for the subsequent 10 minutes, the software was forced to collect spectra only in the delay time range up to 0.2 microseconds (marked by a yellow line in Figure 57b). It is clearly evident how the decay is faster only in that region, while since no data were collected in the second half of the experiment for longer delay times, the two decays are obviously perfectly overlapping in the range after 0.2 microseconds.

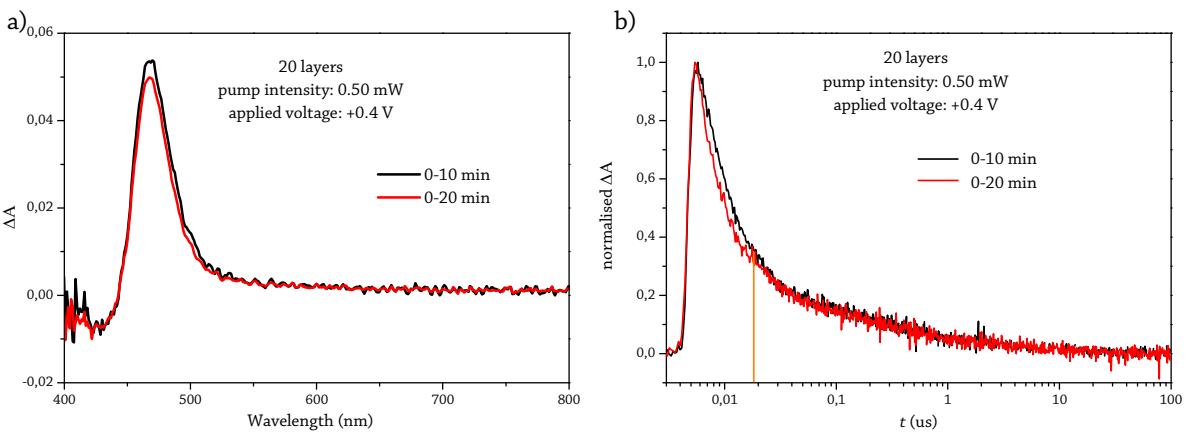

Figure 57: a) Comparison of the absorption spectra at a selected delay time (5.7 ns) between first 10 minutes of data collection and averaged data on the total 20 minutes time of the experiment, conducted with an applied voltage of +0.4V. Clearly, the absorption decreased in time. b) Comparison of time decays at a selected wavelength (467nm) between first 10 minutes of data collection and averaged data on the total 20 minutes time of the experiment. For the first 10 minutes the software was allowed to collect data in the usual way, while for the subsequent 10 minutes, the software was forced to collect spectra only in the delay time range up to 0.2 μs (yellow line).

The samples which underwent extra annealing treatments at 600°C were also tested by transient spectroscopy. The tests in air revealed no difference in decay time compared to the pre annealed samples, both for front illumination and back illumination.

Further tests were planned, as measuring the decay dynamics of doped samples in the electrolyte and by applying a voltage to them. Unfortunately such experiments were not performed, due to the damaging of the only available cuvette, which was essential for performing these experiments. The cuvette broke toward the end of this project and was not replaced in time to allow us to conduct further experiments with the employment of an electrolyte.

4.4.2. Semi-quantitative analysis and results summary

In the previous section it was established that the ΔA values could not be used to calculate the concentration of charge carriers generated. However, a semi-quantitative analysis is still possible by analysing the normalised time traces. The decay were indeed found to have two contributions: a single exponential decay in the fast phase (ns) and a power law decay in the slower phase (μs), as detailed in equation:

$$\Delta A = \Delta A_0 + a \cdot e^{(t-t_\circ)k} + b \cdot t^{-\alpha}$$

Both contributions referred to electron-hole recombination in the bulk, but occurring through two difference processes. In fact, an exponential decay is normally attributed to direct bimolecular electron-hole recombination, while a power law decay is due to dispersive transport of carriers through defect states. A trap (or defect) state is brought by a chemical impurity or an imperfection in the crystal structure that restricts the movement of the captured charge and makes it momentarily unavailable for recombination. Two process that lead to recombination after a charge is trapped are reported in literature.[68–71] One is the trapping-and-release process. The charge is trapped, then removed by that state and free to recombine with the counter charge. Traps exist within a certain distribution of potentials and, as a consequence, the time constants for release from these traps will influence the kinetics of charge recombination. The resultant kinetics are then dependent on the potential values distribution of the traps. A second process, 'hopping', involves the tunnelling of charges from a defect state to another, which eventually leads to charges recombination. In this case, the recombination kinetics are influenced by the spatial and potential distribution of the trapped states. In both cases, α is a value between 0 and 1 which is an indication of the traps distribution extent.

In literature the μs phase of transient decay traces for $BiVO_4$ was also found to be fitted by power law[62,67] and analogous finding for hematite[72] and titania photoanodes[68,73] were also reported.

Therefore, it was established that the power-law kinetics for the μs scale in our analysis could be assigned to trap-limited recombination processes. However, to distinguish between the two proposed mechanisms is outside the scope of this research. Furthermore, a correlation of the α values with the experiments parameters was found to be anything but trivial. Nonetheless, the calculated values were found to be between 0.2 and 0.5 and similar values were reported in literature for $BiVO_4$ photoanodes. Specifically, Ma et al. reported power-law constants varying from −0.24 to −0.32,[62] while Ravensbergen et al. estimated a value of 0.49 for all the excitation energies they employed.[67]

A more detailed analysis was conducted on the exponential contribution of the decay. As explained, such mathematical model corresponds to direct recombination of electron and holes in the bulk. Therefore, the

extrapolated *k* value by the fitted curves represents a rate constant. The following analysis of the results obtained by transient absorption spectroscopy will be based on these values.

Samples tested in air:

Figure 58 shows the calculate k values for samples with different thickness tested in air and increased pump laser energy. If one single sample is considered, it is evident that an increase in excitation energy is cause of slight decrease of recombination rates. This was found to be counter intuitive. In fact, higher pump energies generate higher concentrations of charge carriers. Since the electron and holes are the reactant of the recombination reaction, the kinetics of this process are expected to become faster with increased concentration of charge carriers. However, there's a possibility that these data are a result of instrumental problems. In the *ns* scale we are in fact very close to detection limit and instrumental resolution of the device. Furthermore, the obtained absorption signal could include a contribution from the pump in addition to the sample signal. Therefore, before drawing any final conclusion, the data should be de-convoluted.

The analysis of the influence that thickness has on the extrapolated values of *k*, shows decay kinetics that become slower with increased thickness. This might be due to the competition between recombination phenomena and charge transport in the bulk. In thicker samples charges are generated on a more widely distributed space which might lead to a slower recombination.

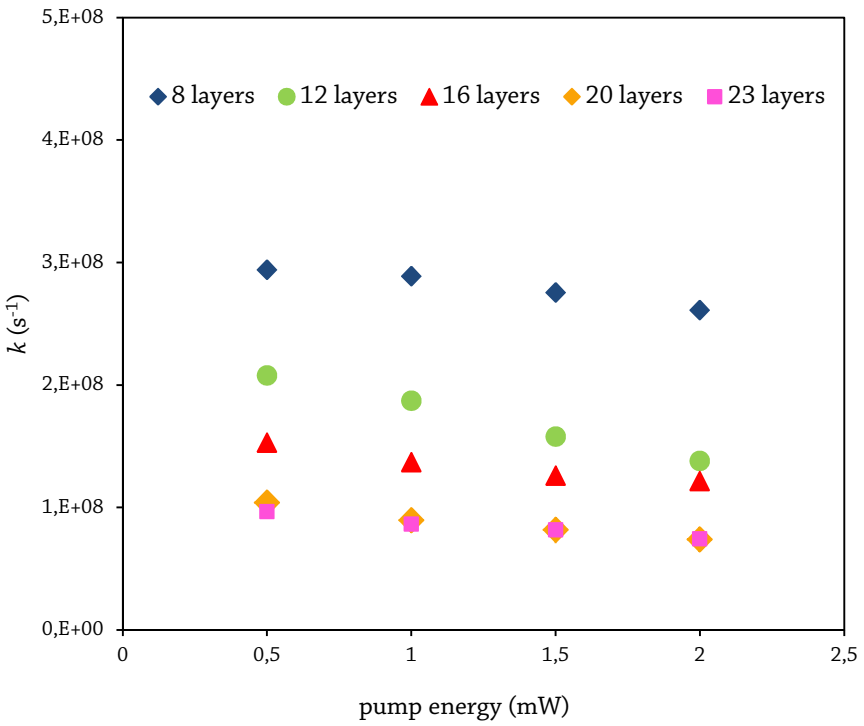

Figure 58: Calculated *k* values from the fitted data. The dependence of *k* with thickness and pump energy is shown.

The samples were also tested while illuminating the film from the back side and after the annealing treatment at 600°C, both with back and front illumination. The results are reported for two different excitation energies in Figure 59 and Figure 60. The first outcome of this investigation is that the extra annealing didn't seem to have any effect on the recombination rates in the bulk. This could be due to the fact that carbon was mostly present at the surface, therefore it is more likely that the effect of carbon removal in transient spectroscopy analysis would be more evident when analysing different time windows where surface phenomena befall.

Decay rate constants showed to be different depending on which side of the sample was illuminated. When analysing film thickness by FIB-SEM cross section, FTO showed to have a really rough surface, with spikes reaching up to 30 nm in height. This made the thickness of thin samples very difficult to determine. In fact, from the analysis of thicker ones, we calculated that every deposited layer would approximately add 5 nm in thickness. If we then consider the 8-layers sample, that would correspond to 40 nm. Considering the roughness of the underlying FTO, the actual thickness will be location-dependent and varying from values like 5 nm up to 50 nm, which is a very extended distribution of thicknesses. Therefore, the decay rates obtained from thin samples are more difficult to interpret, since we cannot know where we are probing the sample (for example on a 5 nm thick spot or on a 50 nm one). If we only consider thicker samples, back illumination resulted in very marginally slower decay rates. This could be explained by the presence of recombination sites located mostly on the surface. If we illuminate from the back, charges will be generated in higher concentration away from this sites, slowing down the decay rate.

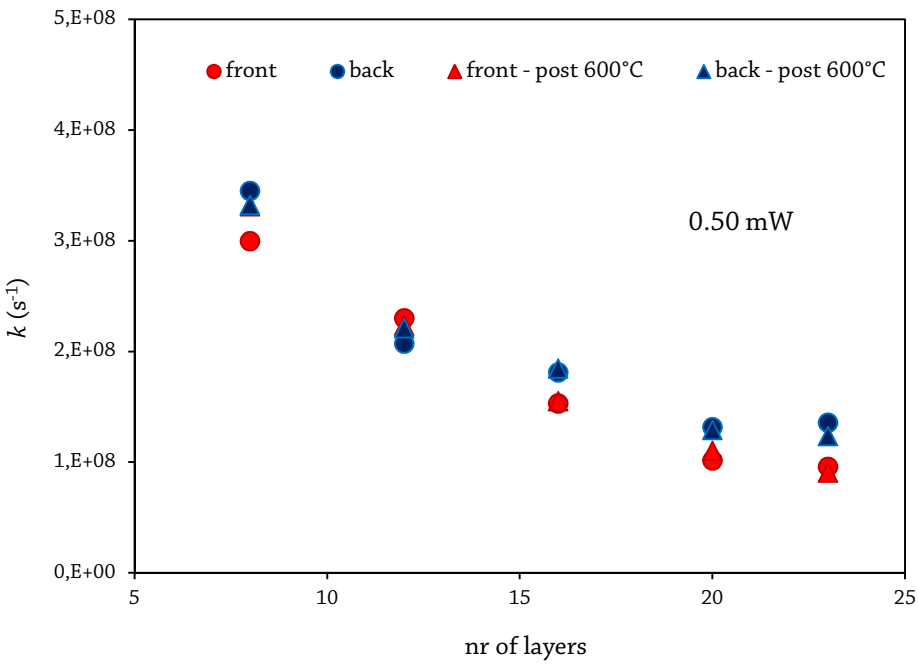

Figure 59: Values of k extrapolated from the fitting of data obtained by transient absorption analysis. The values are reported as a function of thickness and including experiments performed by front and back illumination on sample before and after the extra annealing treatment at 600°C. The energy of excitation was fixed at 0.50 mW.

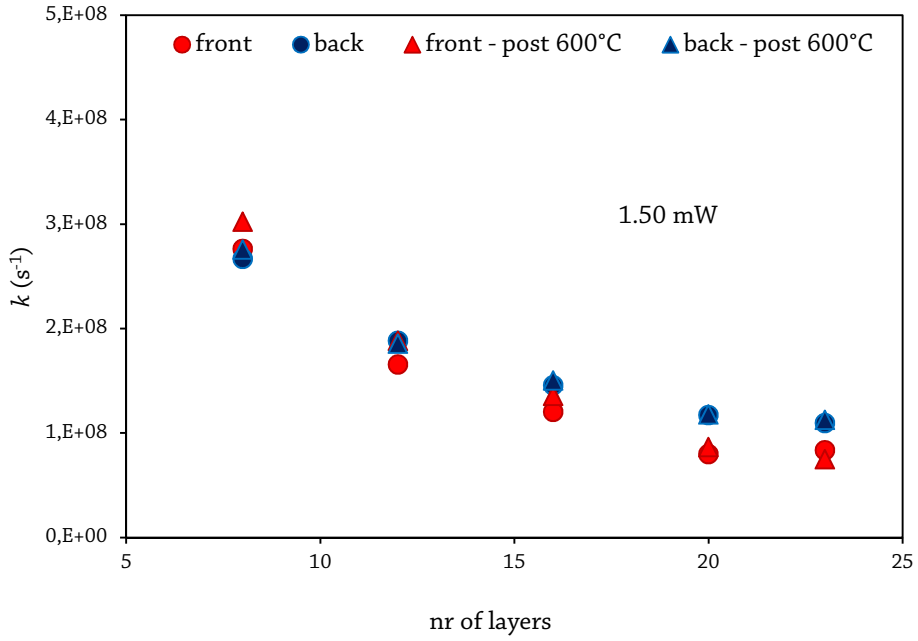

Figure 60: Values of *k* extrapolated from the fitting of data obtained by transient absorption analysis. The values are reported as a function of thickness and including experiments performed by front and back illumination on sample before and after the extra annealing treatment at 600°C. The energy of excitation was fixed at 1.50 mW.

Additionally, samples were tested in different atmospheres, namely Ar and O_2 gases. These experiments were conducted to rule out the possibility of accumulation of electrons at the surface, by analysing the difference in decay rates brought by the presence of an electron scavenger (O_2) or an inert gas (Ar) in contact with the surface. As a result, it was found that no change in decay rates was detected in either cases, therefore it can be assumed that electrons are not accumulated at the surface of our photoanodes.

The samples on which the co-catalyst was deposited were also tested in air. It was clear that no difference in decay rates was due to the presence of CoPi. This is to be expected, since the activation of CoPi would occur in presence of an electrolyte that can accept holes from it. Furthermore, the processes probed are assumed to involve recombination in the bulk that take place on a very fast scale (ns), while hole transport into the electrolyte are reported to occur on longer time scales (ms-s)[67]. This was confirmed by our experiment performed in the presence of an electrolyte.

Samples tested in an electrolyte:

Additionally, charge carrier dynamics were tested with the samples placed first into an phosphate buffer electrolyte and then in the same electrolyte with the addition of a hole scavenger. In Table 4 the calculated values for the 16-layers sample are reported. If we compare the values obtained by the tests in the electrolyte (blue in table) with those in presence of a hole scavenger (marked in red) it is noticeable that there is no significant difference on the decay rate. The hole scavenger is supposed to promote hole transfer into the electrolyte, therefore these results are a further confirmation that the process of hole injection into the electrolyte occurs on

different time scales, while the probed phenomena that take place in the ns-µs scale are not affected. However, the decay rate calculated showed to be marginally higher than those obtained by experiments in air. When an electrolyte is placed in contact with the surface, the bands bends to an extent which is not influenced by the presence of a hole scavenger. However, the bending might affect also processes in the bulk. This could explain why the decay rates for both electrolyte and hole scavenger are slightly higher than those in air, but similar to each other. Nonetheless, it should be expected an opposite behaviour, i.e. the decay rate should become slower with the introduction of bending of the bands. The banding is indeed created by the presence of an internal electric field which promotes transport of holes to the surface and electrons to the back contact, which should lead to slower recombination kinetics in the bulk. Therefore, this behaviour might be related to a marginal degradation of $BiVO_4$ at its surface.

The values for all the other samples are reported in Appendix 8.3.

Table 4: Calculated values of α and k extrapolated from the fitting of the decays of the 470 nm band signal for a 16-layer and a 23-layers samples.

16-layers	α	k (s^{-1})	23-layers	α	k (s^{-1})
air	0.27857	1.38E+08	air	0,26884	9,68E+07
electrolyte	0.3669	2.25E+08	electrolyte	0,35113	1,41E+08
hole scavenger	0.37676	2.17E+08	hole scavenger	0,3526	1,42E+08

Finally, the influence of an applied voltage to the decay rates was also investigated. The results for all samples are summarised in Figure 61. After a first inspection the decay processes seemed to become faster when a positive voltage was applied, while almost no effects were detected for negative or 0V. However, as explained in the results, the absorption signal was found to decay within the 20 minutes time of data collection. Therefore, the decay rate values were also extrapolated for the first 10 minutes of measurements, and as evident in Figure 61, this value seemed to be smaller. This, together with the decrease in absorption signal is a strong evidence of sample damaging. Such behaviour was also reported by Ravensbergen et al.[67] They suggested that, upon applying a positive voltage, holes accumulate at the surface, causing the formation of reactive species in the electrolyte, which lead to the damage of the $BiVO_4$ layer. It is believed that to be the case also for our samples. In fact, the signal would decrease significantly when the laser was constantly hitting the same spot, while it would increase again to the initial intensity when placed on a new spot, for then lowering once more in few minutes time. Nonetheless, during our PEC experiments, degradation was not observed at any value of voltage applied. Therefore this phenomenon is assumed to occur due to the very intense laser energies (10-40sun), which leads to a drastically higher concentration of generated holes. However, if $BiVO_4$ photoanodes were to be employed in a PEC system active for years, degradation would be bound to occur even under 1 sun conditions. It would be interesting to investigate the effect of a hole scavenger or of a co-catalyst, to determine whether or not the removal of accumulated holes at the surface would reduce the extent of degradation.

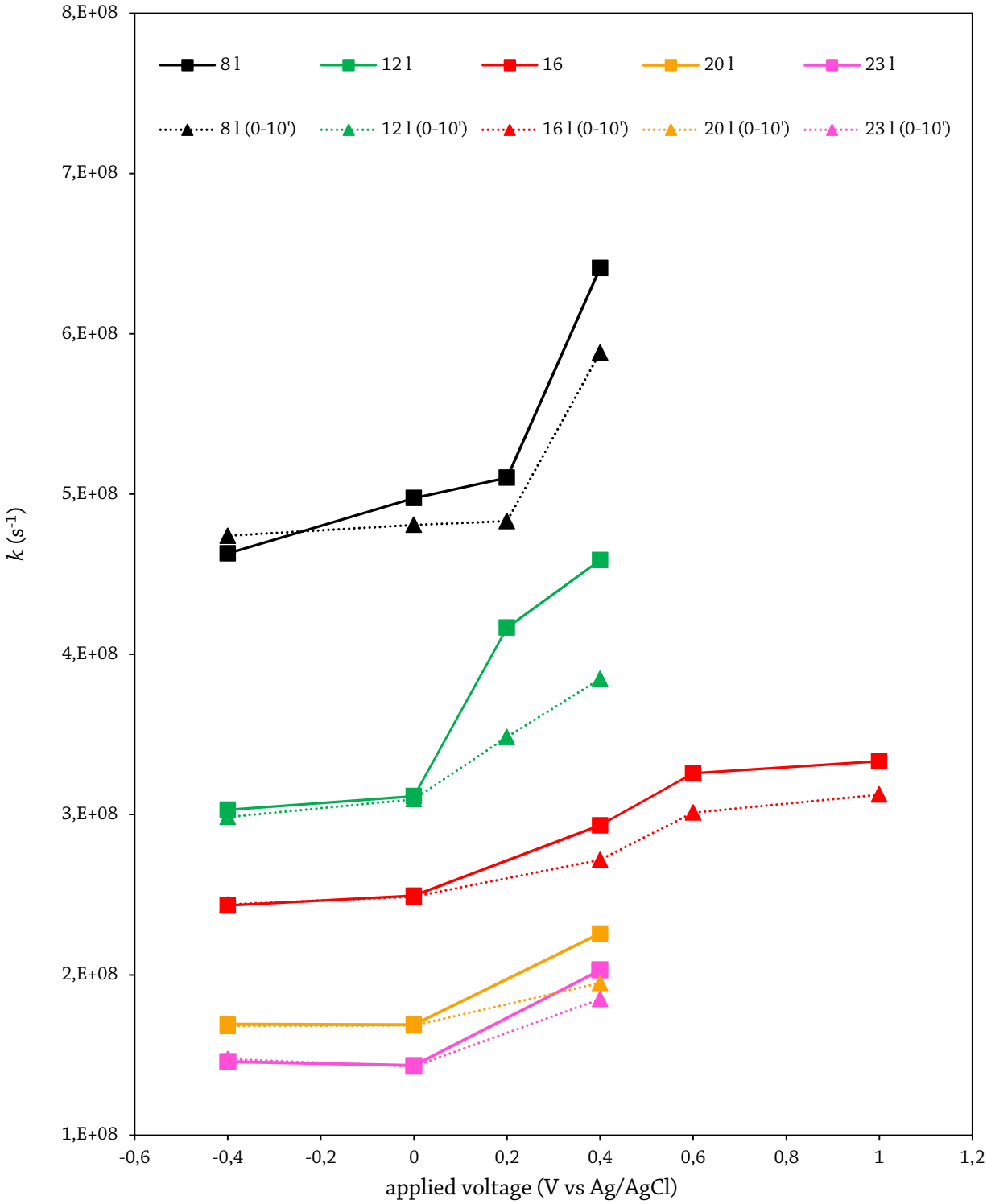

Figure 61: Values of *k* extrapolated from the fitting of data obtained from transient absorption analysis. The values are reported as a function of the applied voltage. Different colours correspond to different sample thicknesses. The values marked by a square referred to the data calculated for the total 20 minutes duration of the experiment. The values indicated by a square correspond to the data extrapolated form the first 10 minutes of measurements. The energy of excitation was fixed at 0.50 m for all experiments.

5. Conclusions

During this research project, the synthesis of thin films of $BiVO_4$ by means of a spin coater was successfully achieved. Even though such deposition method was found to be not trivial, a method for a reproducible synthesis of homogeneous films of the $BiVO_4$ photoactive phase was established. Such encountered difficulties are not surprising. It is clear from literature that this method is user and setup dependent. In fact, every published article reports a different procedure. The success in the synthesis of monoclinic $BiVO_4$ was confirmed by XRD analysis for all samples. The UV-Visible absorption spectra also showed profiles corresponding to those reported in literature. However, the calculated direct ban gaps were found to be of approximately 2.65 eV, slightly higher than expected.

The influence of film width was investigated and it was found that the optimal thickness was about 100 nm. The samples showed to have very low surface kinetics and this problem was successfully addressed by the deposition of a cobalt-phosphate (CoPi) catalyst for water oxidation on the samples surface. It is however believed that there is still a margin for further improvement. Furthermore, the effect seemed more pronounced on thinner samples. The bulk properties were modified by the addition of W in the crystal lattice of $BiVO_4$ as a dopant. The optimal concentration was found to be of 0.2% W to be added to the precursors solution during the synthesis procedure, but no analysis was conducted to establish the actual Bi:V:W ratio in the material.

Moreover, the presence of carbon was detected on all samples and this affected their performances. An extra annealing phase at 600°C was carried on all samples and the carbon concentration was successfully reduced, with a drastic positive effect on the photoperformance on all samples. From these observations, it can be concluded that carbon removal is therefore essential.

From the charge carriers investigation it was possible to establish that, in the window investigated (ns-μs), bulk recombination phenomena take place. Specifically, the direct bimolecular recombination of electron and holes occurs in the fast phase (ns), which is mathematically described by a single exponential decay. On the other hand, trap-mediated recombination processes take place on a longer scale (μs), defined by a power-law decay. Holes injection into the surface befalls on longer time scales. This was reported in literature and found to be the case for these samples as well. In fact, the decay rates deduced by transient absorption analysis of samples placed in the electrolyte were apparently only affected due to degradation of the sample. This was established for experiments in a phosphate buffer, as well as in presence of a hole scavenger and additionally confirmed by experiments with an applied voltage.

Finally, the synthesis of $BiVO_4$ with the spray pyrolysis method was also attempted but not successfully. However, it is believed that bringing further improvements to the setup and synthesis procedure could lead to more positive results.

6. Outlook

The first approach to the synthesis of $BiVO_4$ samples was anything but trivial. The homogeneous desired samples were eventually prepared, but further investigation revealed high amounts of undesired carbon. Moreover, the further annealing of such samples was cause of decreased film homogeneity. Therefore, it is important to keep investigating different synthesis procedures in order to obtained carbon free samples with high homogeneity features. Numerous strategies have been reported in literature, which were not tried during this project. For example, the addition of sodium dodecyl sulphate as a structure directing agent was reported to improve film quality.[74] Another tactic reported is the addition of polyethyleneglycol, with subsequent concentration of the solution by evaporation in vacuum, which leads to a more viscous solution and thicker samples obtained by the deposition of only few layers.[24] Spray pyrolysis should also be further investigated.

An elemental analysis would be interesting for the doped sample, to understand which actual concentration of dopant in the material results beneficial. The verification of the topological distribution of dopant ions within the material would be another interesting aspect to investigate, to check whether or not the ions are evenly distributed or mainly located on specific areas, for example the surface. On the atomic scale, a Raman spectroscopy analysis could be interesting to investigate the location of the dopant atoms in the lattice sites.

As already anticipated in the methods, toward the end of the project, it was realized that the light source used during PEC experiments was not set at 1 sun illumination, but at lower intensities. These samples should therefore be tested using the proper illumination intensity for two main reasons: first, to have the possibility to quantitatively compare these results with literature and second, to make sure that the lower intensity employed was not beneath some threshold value that might change significantly the charge carrier dynamics, hence the performance of the studied electrodes.

For the charge carrier investigation, it would be interesting to know how much the pump pulse is affecting the detected signal, in order to be able to draw conclusion only based on the behaviour of the generated charge carriers. Moreover, an analysis of different time windows would give a more complete picture of the processes that arise in a $BIVO_4$ electrode after excitation. Moreover, it is in presence of an electrolyte that the semiconductor is used in a PEC system; therefore the dynamics of charges in this condition are more significant to the purpose of finding strategies to improve its performance. However, the sample degrades due, most likely due to high laser intensities. To avoid this problem an option would be to add a protective layer on the electrode surface, or to use a system that allows much lower excitation energy densities.

7. Bibliography

(1) Conti, J. J.; Diefenderfer, J. R.; Napolitano, S. A.; Schaal, M.; Turnure, J. T.; Westfall, L. D. *Annual Energy Outlook 2014*; 2014.

(2) Dudley, B. *BP Energy Outlook 2035*; 2015.

(3) Lior, N. *Energy* **2008**, *33* (6), 842–857.

(4) Gratzel, M.; Krol, R. Van De. *Photoelectrochemical Hydrogen Production*; Springer, 2012.

(5) Würfel, P. Wiley - VCH 2005, p 186.

(6) Hulstrom, R.; Bird, R.; Riordan, C. *Sol. Cells* **1985**, *15* (4), 365–391.

(7) Koroneos, C. *Int. J. Hydrogen Energy* **2004**, *29* (14), 1443–1450.

(8) Wang, Z. L.; Naterer, G. F. *Int. J. Hydrogen Energy* **2010**, *35* (21), 11816–11828.

(9) Olateju, B.; Kumar, A. *Appl. Energy* **2013**, *111*, 428–440.

(10) Prévot, M. S.; Sivula, K. *J. Phys. Chem. C* **2013**, *117* (35), 17879–17893.

(11) Chen, Z.; Dinh, H. N.; Miller, E. *Photoelectrochemical Water Splitting Standards, Experimental Methods, and Protocols*; 2013.

(12) Bak, T.; Nowotny, J.; Rekas, M.; Sorrell, C. . *Int. J. Hydrogen Energy* **2002**, *27* (10), 991–1022.

(13) Walter, M. G.; Warren, E. L.; McKone, J. R.; Boettcher, S. W.; Mi, Q.; Santori, E. a; Lewis, N. S. *Chem. Rev.* **2010**, *110*, 6446–6473.

(14) Grätzel, M. *Nature* **2001**, *414* (6861), 338–344.

(15) Alexander, B. D.; Kulesza, P. J.; Rutkowska, I.; Solarska, R.; Augustynski, J. *J. Mater. Chem.* **2008**, *18* (20), 2298–2303.

(16) Li, Z.; Luo, W.; Zhang, M.; Feng, J.; Zou, Z. *Energy Environ. Sci.* **2013**, *6* (2), 347–370.

(17) Bard, A. J.; Faulkner, L. R. *Electrochemical methods: fundamentals and applications*; Harris, D., Swain, E., Robey, C., Aiello, E., Eds.; John Wiley & Sons, 2001.

(18) Vayssierser, L. *On Solar Hydrogen & Nanotechnology*; John Wiley & Sons, 2009.

(19) Frei, H.; Berkeley, L. *Photoelectrochemical Water Splitting Materials, processes and Architectures*; Lewerenz, H. J., Laurence, P., Eds.; RSC Publishing, 2013.

(20) Kai, D.; Zhong, N. **2012**.

(21) Chen, S.; Wang, L. **2012**, *3666* (1).

(22) Abdi, F. F.; Han, L.; Smets, A. H. M.; Zeman, M.; Dam, B.; van de Krol, R. *Nat. Commun.* **2013**, *4*, 2195.

(23) Bornoz, P.; Abdi, F. F.; Tilley, S. D.; Dam, B.; Van De Krol, R.; Graetzel, M.; Sivula, K. *J. Phys. Chem. C* **2014**, *118* (30), 16959–16966.

(24) Sayama, K.; Nomura, A.; Zou, Z.; Abe, R.; Abe, Y.; Arakawa, H. *Chem. Commun. (Camb).* **2003**, No.

23, 2908–2909.

(25) Park, Y.; McDonald, K. J.; Choi, K.-S. *Chem. Soc. Rev.* **2013**, 2321–2337.

(26) Barroso, M.; Pendlebury, S. R.; Cowan, A. J.; Durrant, J. R. *Chem. Sci.* **2013**, *4*, 2724.

(27) Barroso, M.; Mesa, C. a.; Pendlebury, S. R.; Cowan, a. J.; Hisatomi, T.; Sivula, K.; Gratzel, M.; Klug, D. R.; Durrant, J. R. *Proc. Natl. Acad. Sci.* **2012**, *109* (39), 15640–15645.

(28) Abdi, F. F.; Firet, N.; van de Krol, R. *ChemCatChem* **2013**, *5* (2), 490–496.

(29) Liang, Y.; Tsubota, T.; Mooij, L. P. a; van de Krol, R. *J. Phys. Chem. C* **2011**, *115* (35), 17594–17598.

(30) Cooper, J. K.; Gul, S.; Toma, F. M.; Chen, L.; Glans, P.-A.; Guo, J.; Ager, J. W.; Yano, J.; Sharp, I. D. *Chem. Mater.* **2014**, *26* (18), 5365–5373.

(31) Hwang, J. O.; Park, J. S.; Choi, D. S.; Kim, J. Y.; Lee, S. H.; Lee, K. E.; Kim, Y. H.; Song, M. H.; Yoo, S.; Kim, S. O. *ACS Nano* **2012**, *6* (1), 159–167.

(32) Qurashi, M. M.; Barnes, W. H. *Can. Mineral.* **1963**, *7* (4), 561–577.

(33) Luo, W.; Yang, Z.; Li, Z.; Zhang, J.; Liu, J.; Zhao, Z.; Wang, Z.; Yan, S.; Yu, T.; Zou, Z. *Energy Environ. Sci.* **2011**, *4* (10), 4046–4051.

(34) Tokunaga, S.; Kato, H.; Kudo, a. *Chem. Mater.* **2001**, *13* (12), 4624–4628.

(35) Kudo, A.; Omori, K.; Kato, H. *J. Am. Chem. Soc.* **1999**, *121* (49), 11459–11467.

(36) Zhao, Z.; Li, Z.; Zou, Z. *Phys. Chem. Chem. Phys.* **2011**, *13* (10), 4746–4753.

(37) Payne, D. J.; Robinson, M. D. M.; Egdell, R. G.; Walsh, A.; McNulty, J.; Smith, K. E.; Piper, L. F. J. *Appl. Phys. Lett.* **2011**, *98* (21), 2009–2012.

(38) Walsh, A.; Yan, Y.; Huda, M.; Al-Jassim, M.; Wei, S. *Chem. Mater.* **2009**, No. 21, 547–551.

(39) Sayama, K.; Nomura, A.; Arai, T.; Sugita, T.; Abe, R.; Oi, T.; Iwasaki, Y.; Abe, Y.; Sugihara, H. *J. Phys. Chem. B* **2006**, *3*, 11352–11360.

(40) Landsberg, P. T. *Recombination in semiconductors*; Cambridge University Press, 2003.

(41) Papadopoulos, C. *Solid-State Electronic Devices*; 2014.

(42) Grimes, C.; Varghese, O.; Ranjan, S. *Light, water, hydrogen: the solar generation of hydrogen by water photoelectrolysis*; 2007.

(43) Abdi, F. F.; Savenije, T. J.; May, M. M.; Dam, B.; Krol, R. Van De. **2013**.

(44) Seabold, J. a; Zhu, K.; Neale, N. R. *Phys. Chem. Chem. Phys.* **2014**, *16* (3), 1121–1131.

(45) Chen, L.; Alarcón-Lladó, E.; Hettick, M.; Sharp, I. D.; Lin, Y.; Javey, A.; Ager, J. W. *J. Phys. Chem. C* **2013**, *117* (42), 21635–21642.

(46) Rettie, A. J. E.; Lee, H. C.; Marshall, L. G.; Lin, J.; Capan, C.; Lindemuth, J.; Mccloy, J. S.; Zhou, J.; Bard, A. J.; Mullins, C. B. **2013**.

(47) Yang, J.; Wang, D.; Han, H.; Li, C. A. N. **2013**, *46* (8).

(48) Abdi, F. F.; Van De Krol, R. *J. Phys. Chem. C* **2012**, *116* (17), 9398–9404.

(49) Kanan, M. W.; Surendranath, Y.; Nocera, D. G. *Coord. Chem. Rev.* **2009**, *38* (1), 109–114.

(50) Kittel, C. *Introduction to Solid State Physics*, 8th ed.; Johnson, S., Ed.; John Wiley & Sons, 2005.

(51) Ye, H.; Lee, J.; Jang, J. S.; Bard, A. J. *J. Phys. Chem. C* **2010**, *114* (31), 13322–13328.

(52) Ye, H.; Park, H. S.; Bard, A. J. *J. Phys. Chem. C* **2011**, *115* (25), 12464–12470.

(53) Luo, W.; Wang, J.; Zhao, X.; Zhao, Z.; Li, Z.; Zou, Z. *Phys. Chem. Chem. Phys.* **2013**, *15* (3), 1006–1013.

(54) Park, H. S.; Kweon, K. E.; Ye, H.; Paek, E.; Hwang, G. S.; Bard, A. J. *J. Phys. Chem. C* **2011**, *115* (36), 17870–17879.

(55) Stolow, A.; Bragg, A. E.; Neumark, D. M. *Chem. Rev.* **2004**, *104* (613), 1719–1757.

(56) Perednis, D. *Int. J. Thin Film. Sci. Technol.* **2003**, No. 15190.

(57) Korotcenkov, G.; Brinzari, V.; Schwank, J.; DiBattista, M.; Vasiliev, A. *Sensors Actuators, B Chem.* **2001**, *77* (1-2), 244–252.

(58) Chamberlin, R. R.; Skarman, J. S. *113* (1), 86–89.

(59) Siefert, W. *Thin Solid Films* **1984**, *121*, 275–282.

(60) Kim, T. W.; Choi, K.-S. *Science (80-.).* **2014**, *343* (6174), 990–994.

(61) Ruckebusch, C.; Sliwa, M.; Pernot, P.; de Juan, a.; Tauler, R. *J. Photochem. Photobiol. C Photochem. Rev.* **2012**, *13* (1), 1–27.

(62) Ma, Y.; Pendlebury, S. R.; Reynal, A.; Le Formal, F.; Durrant, J. R. *Chem. Sci.* **2014**, *5* (8), 2964.

(63) Li, M.; Zhao, L.; Guo, L. *Int. J. Hydrogen Energy* **2010**, *35* (13), 7127–7133.

(64) Choi, S. K.; Choi, W.; Park, H. *Phys. Chem. Chem. Phys.* **2013**, *15* (17), 6499–6507.

(65) Pilli, S. K.; Deutsch, T. G.; Furtak, T. E.; Brown, L. D.; Turner, J. a; Herring, A. M. *Phys. Chem. Chem. Phys.* **2013**, *15* (9), 3273–3278.

(66) Zhang, L.; Reisner, E.; Baumberg, J. J. *Energy Environ. Sci.* **2014**, *7* (4), 1402.

(67) Ravensbergen, J.; Abdi, F. F.; Santen, J. H. Van; Frese, R. N.; Dam, B.; Krol, R. Van De; Kennis, J. T. M. **2014**.

(68) Cowan, A. J.; Tang, J.; Leng, W.; Durrant, J. R.; Klug, D. R. *J. Phys. Chem. C* **2010**, *114* (9), 4208–4214.

(69) Kuno, M.; Fromm, D. P.; Hamann, H. F.; Gallagher, A.; Nesbitt, D. J. *J. Chem. Phys.* **2000**, *112* (7).

(70) Nelson, J.; Chandler, R. E. *Coord. Chem. Rev.* **2004**, *248* (13-14), 1181–1194.

(71) Scher, H.; Shlesinger, M. F.; Bendler, J. T. *Phys. Today* **1991**, *44* (1), 26.

(72) Pendlebury, S. R.; Cowan, A. J.; Barroso, M.; Sivula, K.; Ye, J.; Grätzel, M.; Klug, D. R.; Tang, J.; Durrant, J. R. *Energy Environ. Sci.* **2012**, *5* (4), 6304.

(73) Tang, J.; Durrant, J. R.; Klug, D. R. *J. Am. Chem. Soc.* **2008**, *130* (42), 13885–13891.

(74) Pilli, S. K.; Deutsch, T. G.; Furtak, T. E.; Turner, J. a.; Brown, L. D.; Herring, A. M. *Phys. Chem. Chem. Phys.* **2012**, *14* (19), 7032.

8. Appendix

8.1. Tauc plots

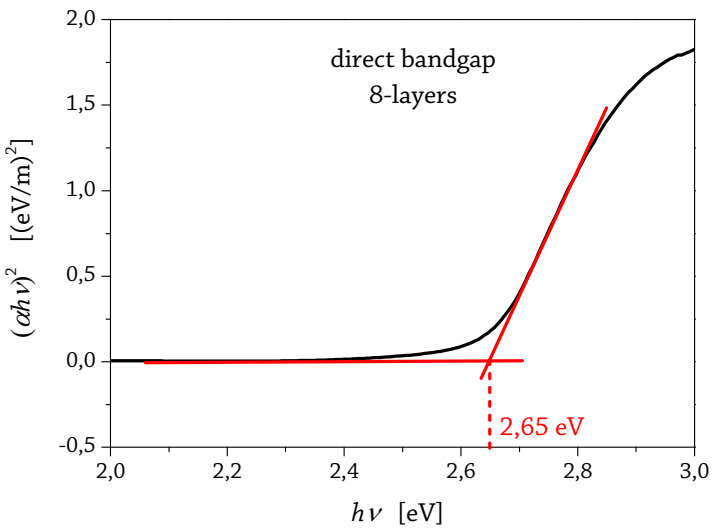

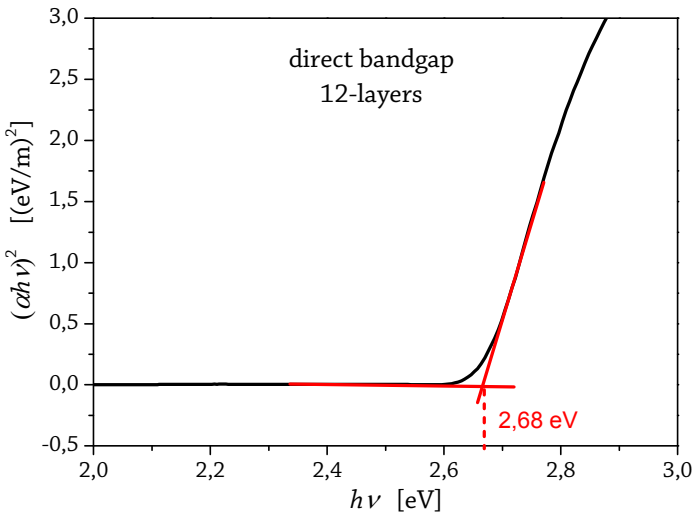

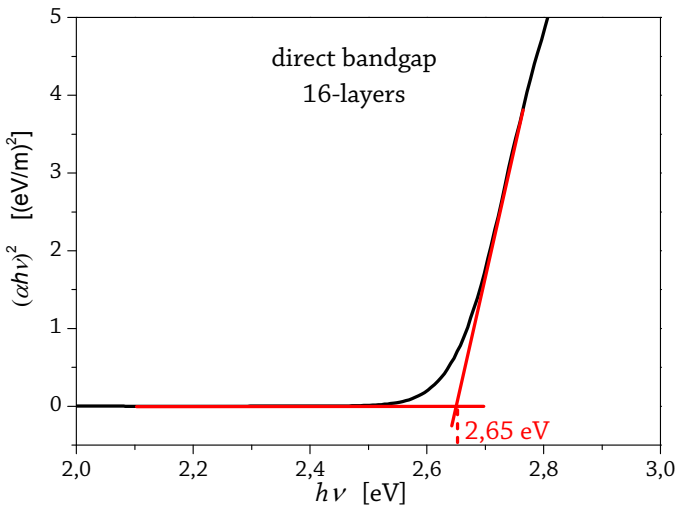
direct bandgap
16-layers
2,65 eV
$(\alpha h\nu)^2$ [(eV/m)^2]
$h\nu$ [eV]

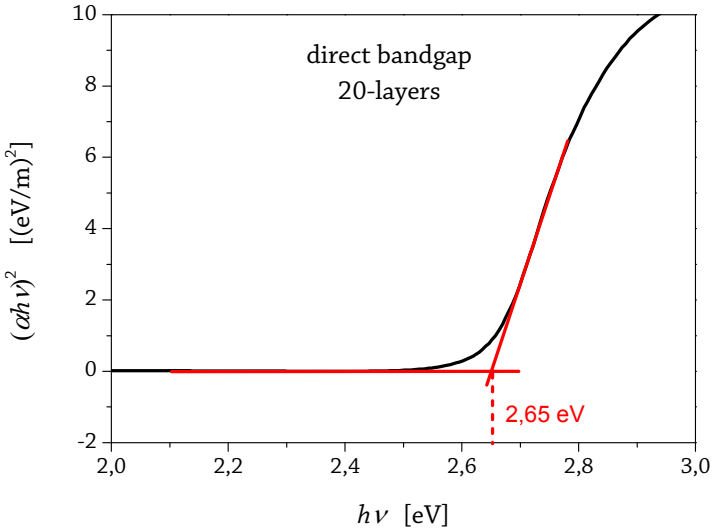
direct bandgap
20-layers
2,65 eV
$(\alpha h\nu)^2$ [(eV/m)^2]
$h\nu$ [eV]

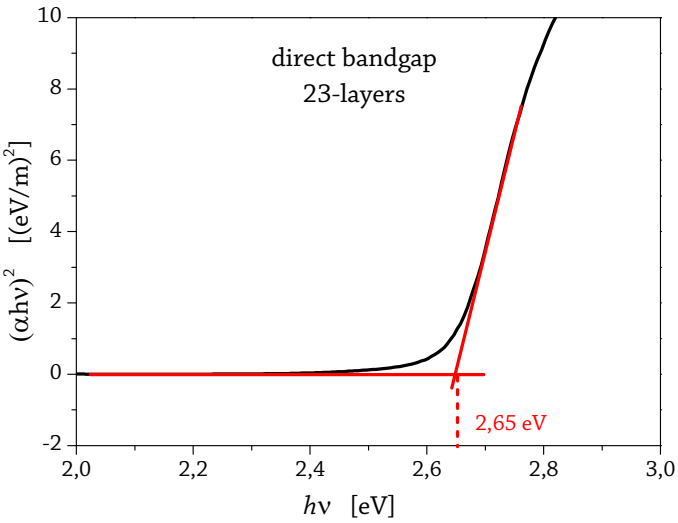
direct bandgap
23-layers
2,65 eV
$(\alpha h\nu)^2$ [(eV/m)^2]
$h\nu$ [eV]

8.2. FTO surface

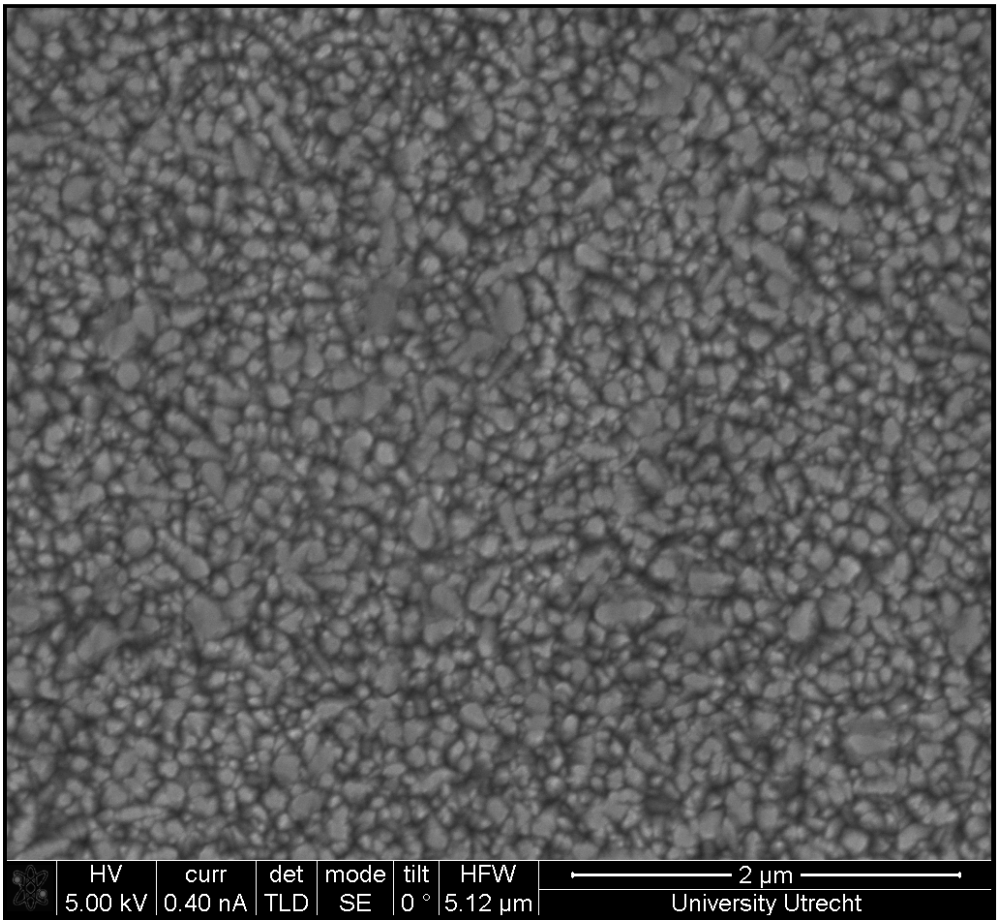

Figure A1: FIB-SEM front image of bare FTO coated glass. As evident, the FTO layer covers the glass homogeneously. However, its surface is not smooth.

8.3. Annealing temperature investigation

After TGA analysis, it was established that a temperature of 530°C should have allowed for total decomposition of the organic component. However, the samples synthetized with such temperature during the annealing step, presented several scattered spots distributed on the sample surface. Therefore lower temperatures and their effect on the photoanodes properties were also investigated. The temperatures studied were in the range of 470-530°C. Such temperatures were in fact expected to allow decomposition of organics and formation of the monoclinic phase. It should be noted that such investigation was carried on at an early stage of this research project, when the synthesis of $BIVO_4$ films was still performed with fixed and very low number of layers, i.e. 7. Nonetheless, the results obtained showed the disappearance of the scattered spots when samples were annealed at lower temperatures than 500°, and a higher absorption intensity (Figure A2). The absorption spectra of the sample annealed at 530°C (red line in figure) was in fact the less intense. Furthermore it showed a slight different profile, due to the scattering brought by the inhomogeneous spots on its surface.

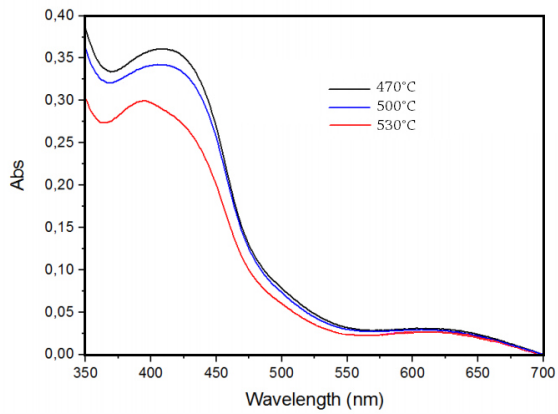

Figure A2: UV-Visible absorption spectra for 7 layers $BiVO_4$ samples annealed at different temperatures.

However, analysis by XRD didn't show any significant difference in cristallinity (Figure A3). This is probably due to the fact that all temperatures studied are well above the temperature of state transition from the tetragonal to the monoclinic phase, i.e. 400°C.

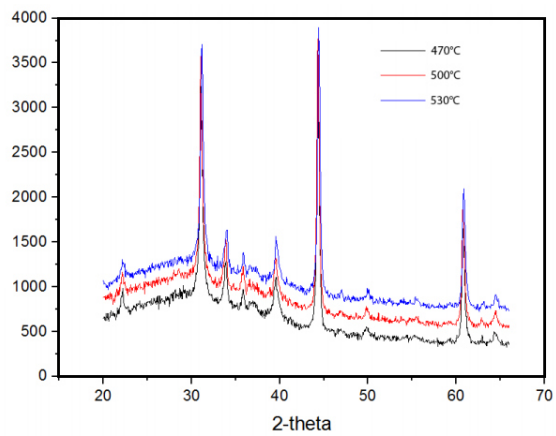

Figure A3: XRD analysis of the 7 layers $BiVO_4$ sample annealed at different temperatures. The integration time per point was of only 0.5s, unlike all other XRD reported in this project which were performed with a 3s integration time per point.

The photoelectrochemical performances were also tested. Such analysis revealed that samples annealed at 470 °C seemed to produce higher photocurrent densities (Figure A4). However, the difference was very marginal and other sample showed to produce lower photocurrents, comparable to those of samples annealed at higher temperatures. Nonetheless, due to the better homogeneity and higher absorption intensities of samples obtained with lower annealing temperature, it was decided to maintained 470°C for the annealing step of all subsequent synthesis. As discussed in this thesis, this led to the production of sample with a residual amount of carbon which negatively influences the electrodes performance.

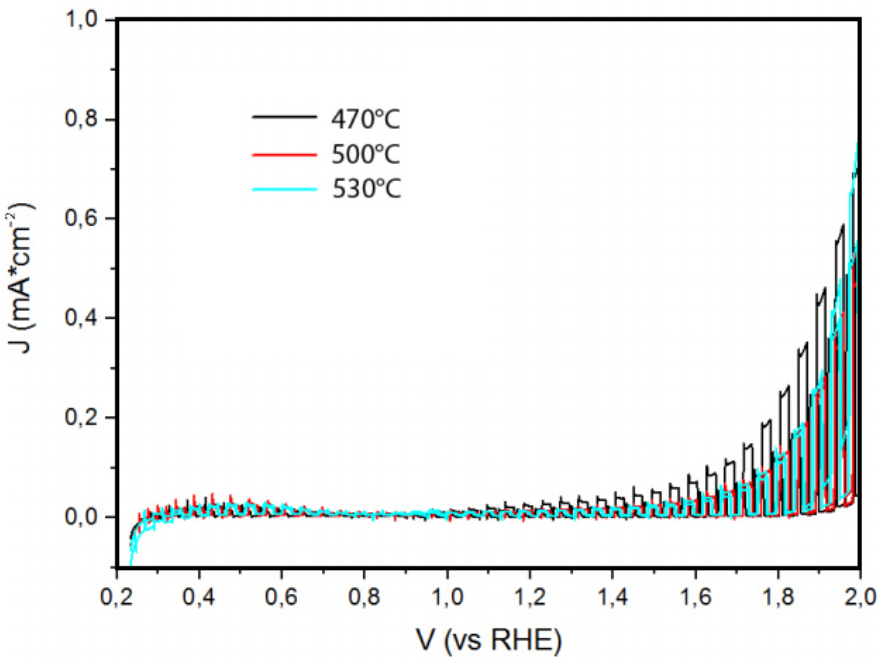

Figure A4: Photocurrent densities produced by 7 layers samples annealed at different temperatures. The experiments were performed with front chopped illumination.

8.4. TAS: alpha and constant rate values

The extrapolated values of α, τ and k with relative deviation standards are reported in the following table for the 8-, 12-, 20- and 23-layers samples. the value are referred to experiment conducted in air (grey), electrolyte (blue) and in presence of a hole scavenger in the electrolyte (red).

8-layers	α	Dev. St.	$k(s^{-1})$
air	0,2648	0,02102	2,94E+08
electrolyte	0,4071	0,02083	4,63E+08
hole scavenger	0,35972	0,01889	4,29E+08

12-layers	α	Dev. St.	$k(s^{-1})$
air	0,24098	0,01044	2,08E+08
electrolyte	0,38179	0,01347	3,46E+08
hole scavenger	0,40146	0,02822	2,90E+08

16-layers	α	Dev. St.	$k(s^{-1})$
air	0.27857	0,02337	1.38E+08
electrolyte	0.3669	0,01388	2.25E+08
hole scavenger	0.37676	0,01139	2.17E+08

20-layers	α	Dev. St.	$k(s^{-1})$
air	0,24695	0,0095	1,01E+08
electrolyte	0,35861	0,01181	1,69E+08
hole scavenger	0,34319	0,01112	1,49E+08

23-layers	α	Dev. St.	$k(s^{-1})$
air	0,26884	0,00751	9,68E+07
electrolyte	0,35113	0,0077	1,41E+08
hole scavenger	0,3526	0,00897	1,42E+08